Zeeman deceleration of Methyl Radical

by

SIDA ZHOU

A THESIS SUBMITTED IN PARTIAL FULFILLMENT OF

THE REQUIREMENTS FOR THE DEGREE OF

DOCTOR OF PHILOSOPHY

in

THE FACULTY OF GRADUATE AND POSTDOCTORAL STUDIES

(Chemistry)

THE UNIVERSITY OF BRITISH COLUMBIA

(Vancouver)

April 2014

Abstract

Conventional Zeeman decelerator, consisting of 80 stages, was constructed and tested. The experimental setup was characterized using O_2 as the reference molecule. Known results of deceleration of O_2 were reproduced. As an extension, detailed REMPI analysis of deceleration of O_2 was carried out, this REMPI analysis was conducted in parallel with ref [1]. Numerical simulation was successful in reproducing the TOF and REMPI spectra of deceleration of O_2.

The extension of using Zeeman decelerator to decelerate a polyatomic radical, CH_3, was successful: from initial velocity of 480m/s to a final velocity of 368m/s, corresponding to a removal of 41.2% of the initial translational energy. The decelerator's efficiency at final velocity of 368m/s is around ~10%. The limiting factor of further deceleration is the signal to noise ratio. Hence, optimization of DC discharge conditions of CH_3 were attempted, but the attempt was with limited success.

Preface

I[(*)] participated in the Zeeman deceleration project under the supervision of Professor Takamasa Momose. I joined the project when it had just started and we had to begin from scratch. The team was led by Professor Momose, with intimate collaboration with the electronic shop and the mechanical shop of the Department of Chemistry. Later on, technician Pavle Djuricanin, and postdoc Yang Liu joined the project.

The electronic shop had a major role in the electrical design of the experimental setup. Pavle Djuricanin and the mechanical shop had a major role in the mechanical design of the experimental setup. Yang Liu had a major role in obtaining the experimental results.

For my contribution in the project: for the construction stage, I had performed the deceleration and magnetic field simulations, which had influenced the experimental design. I was also responsible for much of the miscellaneous labor throughout the project. I saw the first deceleration signals from our experimental setup. Later on, I collaborated with Yang Liu in obtaining the experimental results, which are included in this thesis. I had also completed the analysis of the experimental results by myself, which are included in this thesis.

Results of Section 5.1 (Figure 5.1 and Figure 5.2) was published in "Manipulation of translational motion of methyl radicals by pulsed magnetic fields. Takamasa Momose, Yang Liu, Sida Zhou, Pavle Djuricanin, David Carty. *Phys. Chem. Chem. Phys.*, 15:1772–1777, 2013", in which my main contribution was the simulation results and analysis of the experimental results.

[(*)] sidazhou@gmail.com

Table of Contents

List of Tables

List of Figures

Glossary

$1...10V$ denotes a range from $1Volt$ to $10Volt$

$\{a,b,c\}$ denotes a set of numbers or variables whose members are a,b and c

+ve/-ve denotes positive/negative, ie -ve voltage means negative voltage

LFS denotes low field seeking, or low field seeker

HFS denotes high field seeking, or high field seeker

TOF denotes Time of Flight

REMPI denotes Resonance Enhanced Multi Photon Ionization

MCP denotes MicroChannel Plate

Acknowledgements

I offer my gratitude to my supervisor Takamasa Momose, on his supervision technique, and his understanding, and his lead-by-example on how to become a good scientist.

I offer my gratitude to Yang Liu, who worked tirelessly in obtaining the experimental results.

I offer my gratitude to my peers, Omid Nourbakhsh, Pavle Djuricanin, Mario Michan, Eric Miller, Alex Han for the interesting discussion about science, technology, and everything.

I offer my gratitude to Tony Mittertreiner, Roman Baranowski, Ilja Gerhardt, who have taught me stuff that I never imagined learning.

I offer my gratitude to my friends from all over the world, who kept me alive throughout my PhD degree, you know who you are.

Dedication

This thesis is dedicated to my mom, and to my family, who always wanted a PhD in the family.

==========

"If you want to build a ship, don't drum up people to collect wood, don't assign them tasks and work, but rather teach them to long for the endless immensity of the sea." *-Dr Neil deGrasse quoting Antoine de Saint-Exupery (French aviator)*

==========

Chapter 1: Introduction

1.1 Introduction to cold molecules

The attainment of extreme conditions and the examination and understanding of how matter behaves under previously unattainable conditions is a constant stimulus to scientists. The concept of an absolute zero of temperature has been with us for many years and the challenge of reaching as close as possible to that limit is nothing new. [2]

Cold molecules are molecules that have a temperature in the range of $1mK...1K$. Molecules that are under $1mK$ are labeled as ultra-cold molecules. The key property of molecules at these low temperatures is that only few of the quantum levels are occupied. Dealing with fewer quantum states have many benefits, it will simplify spectroscopic analysis, simplify analysis of reaction dynamics, enable quantum scattering experiments, enable quantum control experiments etc.

Cold molecule research owes much of its original inspiration to the field of cold atoms. However, molecules are more complicated than atoms, but also more interesting: apart from possessing vibrational and rotational degrees of freedoms, molecules may carry dipole (and higher) electric and magnetic moments. [3] These additional properties of molecules will enable us to explore new science.

The research focus in the field is on the techniques in creating large ensembles of cold molecules, and the various applications of cold molecules.

1.1.1 Methods of production

Over the past decade various methods of creating cold molecules were developed. The methods for producing translationally cold molecules can be generally divided into two categories, indirect cooling methods and direct cooling methods.

Indirect cooling methods are to assemble cold molecules from ready cooled atoms through magnetically tunable Feshbach resonances (magneto association) or by photoassociation. The advantage is, these techniques make use of existing methods in laser cooling and evaporative cooling of atoms. The disadvantage is, indirect cooling can only be used to create molecules whose constituent atoms, mainly alkali and rare-earth atoms, can be laser cooled and trapped. The molecules that are assembled such way are translationally as cold as the atoms they were assembled from. [4] [3]

The direct cooling methods are to cool room temperature molecules into the cold regime directly; or to select preexisting cold molecules from a thermal ensemble (velocity filtering). Direct cooling techniques include, but not limited to: magnetic (Zeeman) and electric (Stark) decelerators, laser cooling, buffer gas cooling and evaporative cooling, each method has its advantages and disadvantages. [4][3]

As mentioned, the methods of creating cold molecules are numerous, and comprehensive reviews on the topic can be found on the references used in this section, which are ref [2],[3],[4],[5],[6]. The following section will give a more detailed description on selected topics to illustrate the variety of methods of producing cold molecules available in the field.

1.1.1.1 Buffer gas cooling

One method of cooling molecules is to immerse molecular species in a cryogenic temperature bath of buffer gas (usually helium). The molecular species will be thermalized with the cold buffer gas via elastic collisions, and the end result is a cold molecular ensemble.

The buffer gas cooling method has been pioneered by Doyle and co-workers and has also been implemented by Bakker et al. [5]

Note that, the molecules (or atoms) must thermalize to the temperature of the buffer gas before they reach the walls of the gas chamber, which typically requires several hundred collisions, meaning that rather high pressure is needed in the vacuum chamber.

Also, there must be a method to isolate the cold molecules from the buffer gas. The method utilizes large inhomogeneous magnetic fields to trap molecules in low field seeking Zeeman states in the center of the chamber. Hence, this technique can only be applied to molecules with a sufficiently large magnetic dipole moment. To date, magnetic trapping has been demonstrated for CaH, NH, VO, CrH, MnH and numerous atoms. [5]

Once isolated from the buffer gas, the trapped species will form a new starting point for evaporative cooling, and/or velocity filtering.

1.1.1.2 Laser cooling

Another method to cool the trapped molecular species is laser cooling. The principle of laser cooling relies on finding a closed cycle within the species of interest. The molecule will be excited to the upper states by absorbing a photon, and relax back to lower states via spontaneous emission, forming a continuous cycle, which is repeated. Each photon absorbed will carry a small linear momentum, and the momentum of all photons together will result in cooling of the translational motion of molecule.

Laser cooling has been the most successful method to produce cold atoms. The application of laser cooling to molecules has been considered unfeasible for a long time, because of the complexity of molecular energy level structure, due to the rotational and vibrational degrees of freedom. The complexity of the energy levels in molecules makes finding a closed cycle transition very difficult. However, a number of molecular species have been identified that possess an energy level scheme that may make them suitable for laser cooling, such as NH, CaH, CaF, RaF, OH and others. [6]

1.1.1.3 Photoassociation

The photoassociation method is to synthetize cold molecules from cold atoms. Cold atoms can be achieved using laser cooling.

The photoassociation technique has been applied to form dimers of alkali or alkaline metals. The atoms are irradiated continuously with photons at a frequency just below the excitation frequency of the atom, and if the kinetic energy of the atoms is negligible (which is a good assumption for cold atoms), then at a certain internuclear separation, there will be a transition from the unbounded ground state of separated pair of atoms into a bounded excited state of the dimer. [5]

The very low collision energy limits the total angular momentum and so the molecules are typically produced with little rotational excitation. The formation of the molecules at large separations, however, leads to highly excited vibrational states and there has been significant effort aimed at removing this excitation. [5]

In summary, the three different methods of cooling introduced here are very distinct. The buffer gas cooling method utilizes the collisions with cold ensemble; laser cooling method utilizes the momentum of a photon; photo association method utilizes molecular synthesis together with atomic cooling techniques. And there are many more cooling techniques for atoms and molecules. These methods include, but not limited to: counter rotating nozzle, velocity filtering, Stark deceleration, Rydberg deceleration, Zeeman deceleration, magneto association via Feshbach resonances, superfluid helium nanodroplets, photostop, sympathetic cooling, evaporative cooling etc.

1.1.2 Possible applications

Researches conducted in cold molecules include, few-body and many-body physics/chemistry, precision spectroscopy, probes of fundamental symmetries and constants etc. As techniques advance, a diverse selection of high density, cold, stable molecules will be more readily

available. This will lead to more research possibilities and give further insights in topics such as, controlled molecular dynamics, high-resolution spectroscopy, quantum information technology etc. For molecules that are cold, the thermal de Broglie wavelength is on the order comparable to size of molecules, which correlates with the interaction cross section of the molecule. This quantum effect will give rise to collision rates that deviates from the rate that Arrhenius equation predicts. Another difference is, cold molecules have longer interaction time with external field. This results in, for example, narrowing of spectra lines. [3],[4],[5]

As mentioned, the applications of cold molecules are numerous, and comprehensive reviews on the topic can be found in the references used in this section, which are ref [2],[3],[4],[5],[6]. The following section will give a more detailed description on selected topics to illustrate the variety of applications of cold molecules that are/ might be possible.

1.1.2.1 Astrochemistry

In the extremely low temperatures and pressures characterizing the interstellar medium, the relative translational energies between molecular species are very low and the mean free paths very long. This combination potentially enables species such as highly reactive radicals to exist for extremely long times. This is in contrast to the environment on earth, where highly reactive species are typically very short lived, eg as transient intermediates during a chemical reaction.

In order to identify and interpret the spectra of these molecular species in outer space, it is important to be able to synthesize and study these species under laboratory conditions. In a sense, the cold transient molecules can be used to mimic the interstellar environment. Because the cosmic microwave background temperature of the universe is at $2.7K$, which is also the range of the field of cold molecules. [2]

1.1.2.2 Controlled cold reactions and collisions

External control, using electric or magnetic fields, of bimolecular reactions is desired. The control is complicated by thermal energy, which randomizes the orientation of the molecules,

and the quantum states the molecules are in, which in turn diminishes the effects of external fields on the control process.

The effects of the thermal motion can be reduced by cooling molecular gases to low temperatures. Electromagnetic fields may influence molecular collisions significantly only when the translational energy of the molecules is smaller than the perturbations due to interactions with external fields. At these temperatures, molecular collisions can be effectively controlled with static and laser electromagnetic fields. [7]

Also, at these temperatures, the large de Broglie wavelength of cold molecules changes the nature of reaction dynamics. At such low temperatures, even collisions of large molecules exhibit significant quantum effects. Energy barriers on the potential energy surface play a different role because tunneling becomes the dominant reaction pathway. [7]

1.1.2.3 Quantum information

Ultracold polar molecules trapped in optical lattices provide a promising platform for quantum information processing. Ultracold polar molecules have an advantage of additional tunable experimental parameters, which neutral atoms don't have: static DC electric fields can be used to induce an electric dipole; microwave fields can be used to drive transitions between internal rotational states. The presence of rotationally excited states allows for the possibility to dynamically tailor the dipole-dipole interactions to be effectively short or long range.

Quantum computing schemes based on ultracold molecules have been explored theoretically for some years now. Thus there is a well-developed literature to build from, encompassing everything from molecular vapors to artificial lattice systems to hybrid mesoscopic devices. [4]

In summary, the three different applications of cold molecules introduced here are very distinct. The application to astrochemistry tries to deepen the understanding of chemistry of outer space; the controlled cold collision studies try to advance our understanding reaction

mechanisms and fundamental structures of molecules; the quantum information front might utilize cold atoms and molecules, enabling future possibilities of world changing breakthroughs. And there are many more applications for cold and ultracold atoms and molecules. These methods include, but not limited to: high resolution spectroscopy, time variation of fundamental constants, search for electron dipole moment, barrierless reactions, quantum simulators, direct life time measurements of metastable state etc.

1.2 About the methyl radical

There is considerable motivation to study the methyl radical, CH_3. The methyl radical is one of the most important species in the combustion reactions. [8][9] For example, the reaction between the methyl radial and hydroxyl radical, OH, is an important reaction in the formation of methanol in combustion, but its reaction rate and branching ratio are still under debate. [10] The studies of spectra of radicals also play an important role in astrophysics and astrochemistry, for example radicals occur in comets and interstellar medium. The study of methyl radical is also relevant to surface science [11], for example methyl radical is suspected to be an intermediate species in growth of diamond. [12]

The first spectrum of free methyl radical CH_3 (and free methylene CH_2) was recorded by Herzberg and Shoosmith in 1956. Herzberg was given the honor of presenting his research in the Bakerian Lecture, 1960, on the topic of the spectra and structures of free methyl and free methylene. Herzberg research gave insight into the electronic and the geometrical structure of free methyl and free methylene.

At that time, the spectra of many diatomic free radicals, such as CH, OH, NH, C_2, CN have already been identified and studied. Our current knowledge and theory of diatomic molecules is obtained through the study of these spectra of diatomic free radicals. And the spectra of these diatomic radicals can be readily observed in combustion and electric discharge experiments. [13]

The study of polyatomic radicals came after the study of diatomic radicals. There are two reasons why progress in polyatomic radicals was slower. Firstly, the spectra of polyatomic radicals were much more complex compared with diatomic radicals. Secondly, polyatomic radicals were harder to produce, due to greater difficulty of exciting these spectra in emission. As a consequence, no infrared or Raman spectra of a free polyatomic radical has been observed

in 1956, despite the fact that infrared and Raman spectra of ordinary polyatomic molecules were readily observed.[13]

Since 1956, a variety of spectroscopic studies have been done to determine the molecular parameters of the methyl radical. IR spectroscopy was done by Yamada et al in 1981. [14] REMPI spectroscopy by Hudgens et al. in 1983. [15] CARS spectroscopy by Holt et al. in 1984. Resonance Raman spectroscopy by Kelly et al. [8] CRD spectroscopy by Zalicki et al. in 1995. [16]

The abundancy of research and literature on methyl radical is one of the reasons, which make methyl radical the radical of our choice, in addition to its mass to magnetic moment ratio.

1.3 This thesis

The goal is to produce cold ensembles of polyatomic radicals, which we have chosen to be the CH_3 radical. The challenge is that CH_3 is polyatomic (as opposed to diatomic or atoms), and that CH_3 being a radical is reactive, and is in a chemically metastable state.

There are many methods to produce cold molecules, however many of them are not applicable when trying to cool down CH_3. For example, laser cooling on molecules has only been done on alkali dimers, hence finding a closed cycle transition in CH_3 might be difficult. Photoassociation into a metastable polyatomic radical species is unheard of. Buffer gas cooling might not be possible, since molecular collisions should be avoided with the highly reactive CH_3. Rydberg decelerator requires the species in its Rydberg state, which is not cold in the electronic degree of freedom. Stark decelerator requires the molecule to have a permanent dipole moment, which is not generally applicable for radical species. Zeeman decelerator, on the other hand, requires the molecule of interest to have a non-zero magnetic moment, ie non-zero spin. And radicals by definition have an unpaired electron, which gives rise to a non-zero spin. Hence, Zeeman decelerator is a general and a good method for the production of cold molecular radicals.

So far, only simple radical species, such as H (Zeeman), OH (Stark), NH (Stark), NO (Stark), have been decelerated, using Stark or Zeeman deceleration techniques. In this thesis, we will extend the application of the deceleration technique to more complex polyatomic radical, CH_3, which due to its complexity, is inherently more interesting.

1.4 History of Zeeman decelerator

Zeeman decelerator have much in common with Stark decelerator, the purpose of both techniques are to decelerate supersonic molecular beams using external fields. We can argue, design of Zeeman decelerator is inspired by the success of Stark decelerators. Therefore, it is important to investigate the development of Zeeman decelerator in parallel to the development of Stark decelerator.

1.4.1 Notes on Stark decelerator

The first proof of principle experiment was done by Meijer's group in 2000, where CO molecule was guided using Stark decelerator. [17] And the first deceleration of supersonic molecular beam was done shortly after, with deceleration of NH_3 using Stark decelerator in 2002 [18] Note that, sometimes we call the Stark decelerator developed in 2000, the 1st generation Stark decelerator, or the conventional Stark decelerator. Since 2002, the Stark deceleration has been improved by improving the switching sequence of the electrodes, without changing the design of the decelerator itself. First notable improvement was in 2009, s=3 mode of operation, where only every third electrode is used to decelerate, and rest of the electrodes are used to focus the molecular beam. s=3 mode of operation effectively decouples the transverse motion from the longitudinal motion, making the control of the beam dynamics easier, and hence improving the beam intensity at the end of the decelerator. [19] Second notable improvement, without changing the design of decelerator, was also in 2009, bunching mode of operation, where first ~100 stages of Stark electrode were used to aggressively decelerate the beam, and last ~50 stages of Stark electrode were used for bunching. The idea is to have better control over the phase space, and match the emittance of the Stark decelerator with the acceptance detection, hence improving the beam intensity. [20]

There are also different designs of Stark decelerators, based on the same principle of conventional Stark decelerator, ie utilizing the Stark shift to manipulate the motion of the molecular beam using external fields. For example, alternative gradient variant of Stark decelerator was developed in 2002 to manipulate the high field seeking states, instead of low

field seeking states. [21]. Proof of principle of optical Stark decelerator was done in 2004, which utilized the optical dipole force induced by pulsed fields. [22] Travelling trap Stark decelerator on a chip was done in 2008, which is a miniaturization of a travelling trap Stark decelerator, proof of principle by transporting metastable CO molecules above the chip. [23] Wire Stark decelerator was demonstrated in 2010, where Stark electrodes are replaced by thin wires, resulting in 10 times smaller in size compared with the size of conventional Stark decelerator. [24] Macroscopic traveling trap Stark decelerator was demonstrated in 2010, where conventional Stark electrodes were replaced by ring electrodes, hence providing 3D confinement, resulting in a larger emittance of the decelerator. [25]

1.4.2 Notes on Zeeman decelerator

First demonstration of Zeeman deceleration was reported in 2007 by two independent groups in parallel. The Merkt's group (ETH, Switzerland) decelerated atomic hydrogen and [26] And, the Raizen's group (UT Austin, US) decelerated metastable neon. [27]

For Merkt's group, in early 2008, the final velocity of $107 m/s$ for H was achieved [28], which was sufficiently low for trapping, and trapping experiment of H was successful shortly after. [29] Investigation of motion of molecules in Zeeman decelerator was conducted [30], and REMPI analysis of the molecular beam was also done [1].

Meanwhile, for Raizen's group, after deceleration of metastable neon in late 2007 [27], the group investigated the deceleration of O_2. [31] After which Narevicius (WIS, Israel) branched out from Raizen's group, and investigated moving trap Zeeman decelerator theoretically [32] and experimentally [33] with good success.

The main design differences between Merkt's group vs Raizen's group are, the chamber design (coil outside the chamber vs coil inside the chamber); the presence of magnetic shielding materials around the coil (no shield vs shielding), and the electrical current used in the coil (200A vs 700A), leading to different maximum B-field (1.5T vs 5.2T).

The success of Zeeman deceleration has sparked the interest of many other groups. To date, there are several new groups in the world starting on Zeeman deceleration. Some of the examples are following: Vanhaecke (FHI of MPG, Germany) new design for moving trap Zeeman decelerator, utilizing magnetic hexapoles[34]; Momose (UBC, Canada) deceleration of methyl radical [10] (this thesis); Softley (Oxford, UK) working on similar Zeeman decelerator design as Merkt's groups design; Carty (Durham, UK) working on moving trap Zeeman deceleration.

To summarize, the species that was decelerated by Zeeman decelerator to date (late 2013) (excluding the content of this thesis, which is the deceleration of methyl radical) are nicely summarized in Table 1.1.

Species	State	Remarks
H	$1^2S_{1/2}$, $F = 1$	Deceleration
	$1^2S_{1/2}$, $F = 1$	Magnetic trapping
D	$1^2S_{1/2}$, $F = 3/2$	Deceleration
	$1^2S_{1/2}$, $F = 3/2$	Magnetic trapping
Ne	$(2p)^5(3s)^1\ ^3P_2$	Deceleration
Ar	$(3p)^5(4s)^1\ ^3P_1$	Guiding
O_2	$X\ ^3\Sigma_g^-$	Deceleration

Table 1.1 - Species decelerated by multistage Zeeman decelerator [35]

1.4.3 Notes on other deceleration methods

There are situations when neither Stark nor Zeeman deceleration is applicable. For example, molecules of interest have no electric and magnetic dipole moment in its ground level; or for example, the level of interest is a high field seeking state. In these cases, methods such as Rydberg-Stark deceleration or microwave deceleration can be used.

Rydberg-Stark deceleration does not rely on the existence of a ground state electric or magnetic dipole moment. Instead the molecules are photoexcited to Rydberg states, which

exhibits large electric dipole moments. And since all atoms and molecules possess Rydberg states, this approach is quite general and therefore applicable to species that cannot be decelerated by multistage Stark or Zeeman deceleration, for example H_2. [36]

Microwave deceleration uses microwave radiation field inside a resonant cavity, which will produce a standing wave electric field, and combined with the AC Stark shift of the molecules, can be used to manipulate the motion of high field seeking states of a molecule. [37]

To conclude, we note that Stark decelerator and its variants have a much longer history and more concentrated effort than Zeeman decelerator. Hence Zeeman decelerator has a lot of potential new designs and ideas, inspired from Stark decelerator.

It is also equally important to note that, both Stark and Zeeman decelerator borrows a lot of concepts from linear accelerators. In many aspects, Stark and Zeeman decelerators are linear accelerators operated in a different mode, to decelerate instead of to accelerate. The goal of both accelerator and decelerator are to manipulate the motion of molecular beam using external field. Concepts such as phase space, emittance, acceptance, chromatic aberrations, weak and strong focusing etc are common in both accelerator physics and decelerator physics. And it is obvious that accelerator physics is a much more mature field than decelerator physics. Hence knowledge and expertise in accelerator physics will give inspirations on the future development of decelerator techniques.

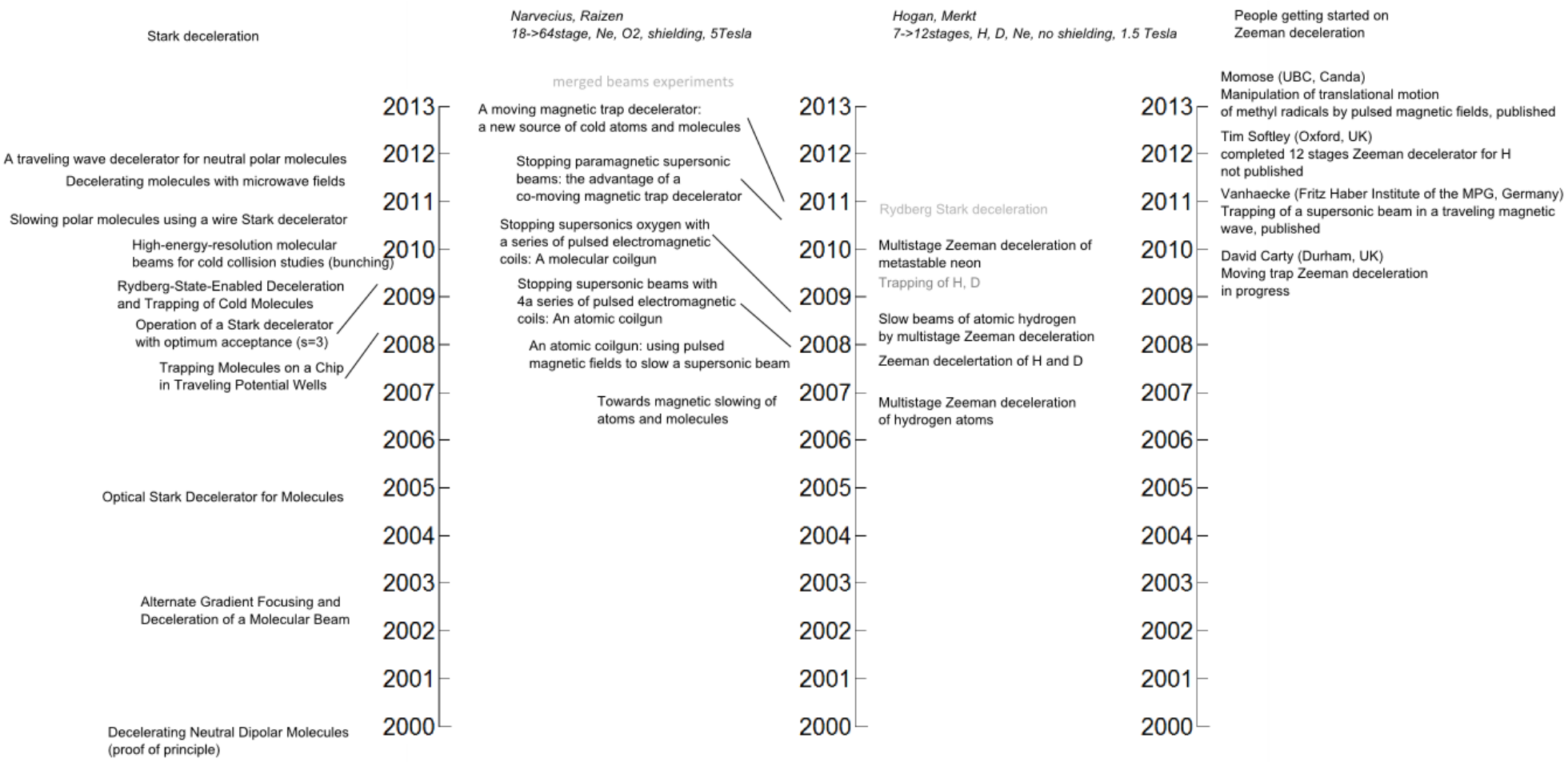

Figure 1.1 – Summarizing figure. Left column shows the important advancements in the development in Stark decelerator; middle two columns show all the publications on Zeeman decelerator of the more established groups; and right column shows the groups that are starting on Zeeman deceleration

1.5 Principle of Zeeman decelerator

The goal is to produce a packet of molecular beam, which is ideally in the absolute ground state, ie in the rotational ground state, vibrational ground state, and electronic ground state. In addition, we would wish the molecules to be standing still in the laboratory frame, ie translational ground state. In practice, using supersonic expansion together with Zeeman deceleration, temperatures of few kelvins can be reached, instead of temperatures of absolute zero.

Supersonic expansion is used to cool the rotational, vibrational and electronic degrees of freedom. Zeeman decelerator is used to cool the translational degree of freedom.

1.5.1 Cooling of rotational vibrational and electronic degrees of freedom

In the supersonic expansion section, we estimate the final temperature of the beam after nozzle expansion to be about $\sim 1K$, see section about supersonic expansion. We assume that equipartition theorem holds, meaning that molecules inside the beam had enough collisions and are thermalized. Then, the energy is shared equally among all of the degrees of freedom, in other words, we assume rotational, vibrational and electronic temperature are all about $\sim 1K$.

At the temperature of $\sim 1K$, only the ground state vibrational and electronic degrees of freedom are populated, because the spacing between the energy levels are very large, $330cm^{-1}...50000cm^{-1}$, see Table 1.2, compared to the temperature $\sim 1K$ ($=\sim 0.7cm^{-1}$).

Because of the spacings of the energy levels in rotational degree of freedom are small, $0.033cm^{-1}...330cm^{-1}$, and are comparable to the temperature $\sim 1K$ ($=\sim 0.7cm^{-1}$). Hence, states other than the ground rotational state are also populated. We have found through our experience, for the species we are working with, namely O_2 and CH_3, only few rotational states, $\sim 2...5$ states, of the lowest energy are populated, which is sufficient for our purposes.

	Rotation of polyatomic molecules	Rotation of small molecules	Vibration of flexible bonds	Electronic transition
Wavenumber(cm^{-1})	0.033...3.3	3.3...330	330...14500	14500...50000
Region	Microwave	Far infrared	Infrared	Visible and ultraviolet

Table 1.2 – typical values for rotation, vibration, and electronic energy level spacing. [38]

In summary, supersonic expansion is sufficient to reduce the electronic, vibrational, and rotational temperature of the molecular beam.

1.5.2 Cooling of translational degrees of freedom using Zeeman decelerator

The molecular beam exiting the nozzle, the translational energy (aka kinetic energy) in the laboratory frame is high, while energy in other degrees of freedom is low. Zeeman decelerator is used to reduce the translational energy (aka kinetic energy) of the molecular beam. In Zeeman decelerator, a narrow pulse of molecules is slowed by rapidly switching and dynamically controlling inhomogeneous magnetic fields.

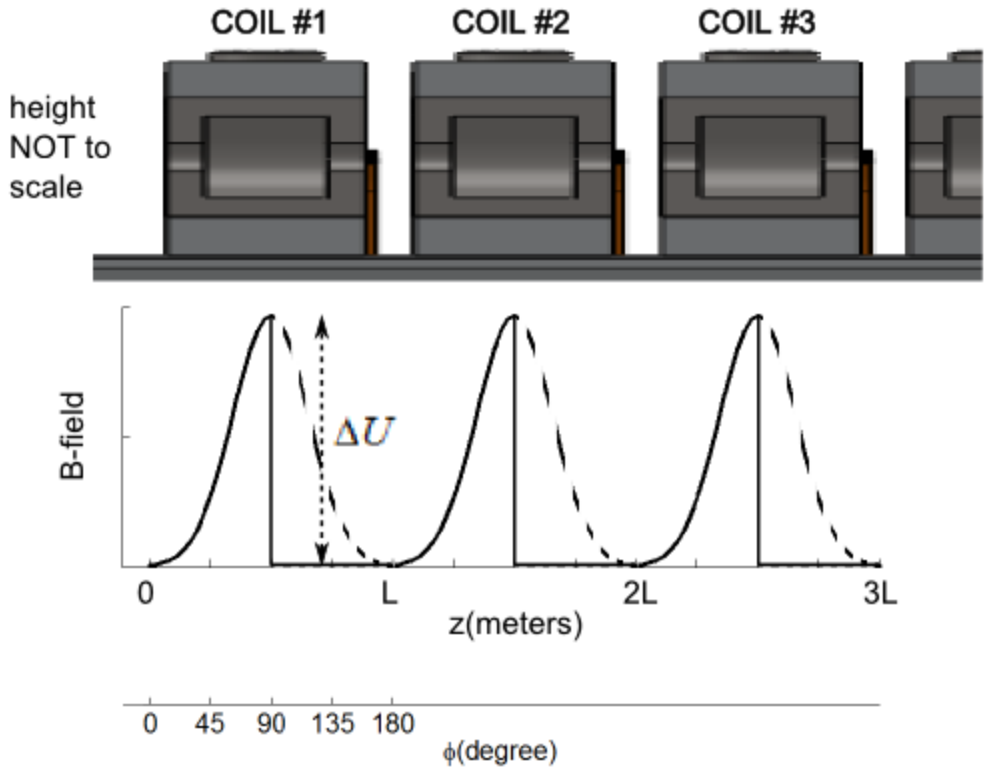

Figure 1.2 – Bottom figure is the illustration of switching of the B-field inside Zeeman decelerator. z *is the molecular beam axis.* L *is the length of one coil stage,* ΔU *is energy lost per stage. Solid line is the B-field variation along* z *. Dotted line is the situation if we don't do any switching. Top figure is drawing of the first 3 coils of the decelerator, vertically aligned to the bottom figure, included for clarity.*

We shall examine the deceleration process using Figure 1.2. The molecular beam flies from left to right in Figure 1.2. We define a molecule, called the synchronous molecule, which has a specific quantum state, specific position and specific velocity within the ensemble of molecules, and the deceleration process will be determined based on this synchronous molecule. Usually, a molecule in the region of highest initial phase space density is selected as the synchronous molecule.

In Figure 1.2, the coil forms a magnetic hill, with the maximum B-field in the center of the coil. For molecules in a magnetic field, there would be a Zeeman shift, $U(B)$. For the synchronous

molecule, which is a low field seekers, ie having a positive slope in the Zeeman shift, $dU / dB > 0$, will gain Zeeman potential energy, and lose kinetic energy by moving into the high magnetic field region at the center of the coil. When the synchronous molecules reach the top of the magnetic hill, it will gain an amount of potential energy:

$$\Delta U = U(B = B_{switchoff}) - U(B = B_{-\inf})$$

Equation 1.1

In Equation 1.1, $U(B = B_{switchoff})$ is the energy of the Zeeman shift at a point in space, up the magnetic hill, when we instantaneously switch the B-field off. $U(B = B_{-\inf})$ is the energy of the Zeeman shift before the coil, usually $B_{-\inf} = 0$, however if there is leak field far away from the coil, then $B_{-\inf} \neq 0$.

Due to conservation of energy, the amount of the kinetic energy, ΔE_k lost is equal to the Zeeman potential energy gained, ΔU. More strictly speaking, the gain of the Zeeman potential energy , $U(B)$ changes only with respect to changing of the B-field, $B(z)$, which in turn is a variable of position z. In other words, Zeeman potential energy is a function of position, $U(B) \rightarrow U(z)$. Variation of position is the same as motion of the molecule, and hence the gain in Zeeman potential energy is coupled to the loss of kinetic energy (as opposed to, for example, loss of rotational energy).

In the case of not switching the field, the low field seeking synchronous molecules will lose the gained potential energy, ΔU, and regain the exact same amount kinetic energy ΔE_k. Resulting in no change in kinetic energy, and hence no deceleration.

The reduction in the ΔE_k of the synchronous molecule, is per one coil. Therefore, this process can be repeated with N coils, such that total kinetic energy lost is equal to $N \times \Delta E_k$. In principle, if the decelerator is long enough, ie having enough stages, ie N is large enough, then

all kinetic energy of the molecule can be removed, ie final velocity of molecule is $0m/s$ in laboratory frame. However, when analyzed further, there are several practical and theoretical limiting factors, which prevent us to achieve final velocity of $0m/s$.

It can also be derived that the force experienced by the molecule along the molecular beam axis is

$$F_z = -\frac{dU}{dB}\frac{dB}{dz}$$

Equation 1.2 - where dU/dB is the gradient of Zeeman shift (see sections 2.6 and 2.8 about zeeman shifts) with respect to external B-field, dB/dz is the gradient of the external B- field shift with respect to the position along z-axis in space. To clarify, by B-field we mean the norm of the B-field, $B = |\vec{B}|$.

And similarly, the forces perpendicular to the molecular beam axis are

$$F_x = -\frac{dU}{dB}\frac{dB}{dx},\ F_y = -\frac{dU}{dB}\frac{dB}{dy}$$

Here are some typical values for deceleration of O_2 molecule are calculated for reference. We select the target state to be $|N''=1, J''=1, m_{J''}=1\rangle$. For the estimation, let's assume B-field strength is $2.2Tesla$. Then, the energy lost per stage is calculated to be $\Delta E_k = 2.9e-23Joules$. Assuming initial velocity is $250m/s$ which corresponds to $1.7e-21Joules$ of initial kinetic energy. This indicates that $N=57$ stages of coils are needed to decelerate O_2 down to $0m/s$. And the final velocity achieved using 15 stages is $215m/s$. Note that later stages will have larger decrease in velocity, because the change in velocity, Δv, is larger as the velocity of molecules, v, is lower in later stages, as change in energy per stage $\Delta E_k = mv\Delta v$ stays constant.

H atom can also be decelerated using Zeeman decelerator. For H atom, the Zeeman splitting and the mass will be different from O_2, and estimation gives $\Delta E_k = 1.3e-23J$ lost per stage.

Assuming same initial velocity $250m/s$, which correspond to $5.2e-23J$ of initial kinetic energy. This indicates that only $N=4$ stages of coils are needed to decelerate H down to $0m/s$. This was to illustrate that there is a huge contrast in number of stages needed, between deceleration of a light atom compared with deceleration of a heavier molecule.

The discussion so far, is limited to the synchronous molecule. There are molecules which have slight different position or velocity from the synchronous molecules, called phase stable molecules, which are also decelerated. And the signals we detect are the phase stable molecules. Hence it is important to maximize the number of phase stable molecules, or more precisely speaking, phase stable area.

There is a tradeoff between amount of deceleration, and the phase stable area, which is the concept of phase stability. Phase stability is also the reason, why achieving final velocity of $0m/s$ is not possible. In practice, translational temperature of $\sim 5K$ can be readily reached. All the concepts regarding phase space will be described in more detail in sections about longitudinal (Section 2.2) and transverse phase space stability (Section 2.3).

In summary, rotational, vibrational and electronic temperature of few kelvins can be achieved, by using supersonic expansion. Translational temperature of few kelvins can be achieved, by using Zeeman decelerator. And, hence, all degrees of freedom of the molecule can be cooled.

==========

"[On scientific writing] if the reader is to grasp what the writer means, the writer must understand what the reader needs." -*Judith Swan*

==========

Chapter 2: Necessary calculations and analysis

2.1 Supersonic expansion

2.1.1 Effusive beam

Molecular beam can be produced by expanding gas from a reservoir of high pressure, P_0 (gas sample), into a reservoir of low pressure, P_b (vacuum chamber) through a pinhole. If the mean free path, λ_0, of the molecules in high pressure reservoir is much larger than the diameter of the orifice of the nozzle, d, ie $\lambda_0 \gg d$, then the beam is called effusive molecular beam. And if the mean free path of the molecules in high pressure reservoir is much smaller than the diameter of orifice of the nozzle, ie $\lambda_0 \ll d$,then the beam is called supersonic molecular beam.

In effusive beam, since mean free path is much larger than the orifice of the nozzle, there are no collisions when gas exits and expands through the nozzle, hence no interactions between the molecules, hence the properties of the beam are similar to before expansion through the orifice. The beam property before and after the nozzle expansion can be described using Maxwell distribution [39], $f(v)$

$$f_{effusive}(v) = 4\pi\left(\frac{m}{2\pi kT_0}\right)^{3/2} v^2 exp\left(\frac{-mv^2}{2kT_0}\right)$$

Equation 2.1 – Maxwellian velocity distribution, where m is molecular mass, k is Boltzmann's constant, T_0 is the temperature of the high pressure reservoir.

The central velocity is

$$v_{central} = \sqrt{2kT_0 / m}$$

Equation 2.2

and the width of this distribution is $\sigma_{velocity} = \sqrt{kT_0 / m}$.

2.1.2 Structures in supersonic beam

Supersonic beam will form, provided the pressure ratio inside the nozzle (high pressure reservoir) vs the vacuum chamber (low pressure reservoir) exceeds a critical value:

$$P_0 / P_b \gg ((\gamma+1)/2)^{\gamma/(\gamma-1)}$$

Equation 2.3 - where P_0 *is the pressure of high pressure reservoir,* P_b *is the pressure of low pressure reservoir,* $\gamma = C_p / C_V$ *is the ratio of heat capacities of the gas.* $\gamma = 5/3$ *for monoatomic gases,* $\gamma = 7/5$ *for diatomic gases at low temperature (ignoring vibration degree of freedom), and* $\gamma = 9/7$ *for diatomic gases at high temperature (including vibration degree of freedom).*

For example, we can verify that the inequality from Equation 2.3 is indeed true, in our case, when we use O_2 as the sample gas, $\gamma = 7/5$,with backing pressure of $P_0 = 10bar$, expanding to a vacuum of $P_b = 1e-6torr$, the inequality from Equation 2.3 evaluates down to $P_0 / P_b = 7.5e9 \gg 2 = ((\gamma+1)/2)^{\gamma/(\gamma-1)}$.

In supersonic beam, since mean free path is much smaller than the orifice of the nozzle, there are a lot of collisions between the molecules as the molecules exit and expand through the nozzle. This interaction through collisions will lower the energy in rotational and vibrational degrees of freedom of the molecule. These collisions will also increase the central velocity of the beam, and narrow the velocity distribution.

Both theoretical and experimental study of supersonic beam began around 1951[39]. In Figure 2.1, we see the structure of the supersonic expansion: after the expansion from high pressure reservoir, P_0 , to low pressure reservoir, P_b , several interesting features are formed. The expansion can be described as a high speed stream flowing into a stagnant background. A shear layer is formed due to the velocity difference between the stream and the stagnant background, which will draw the surrounding gas and mixes it with the jet stream creating small

scale turbulent eddies and large scale structures.[40] The large scale structure of interest to us is the zone of silence, barrel shock, and Mach disk shock, which are sketched in Figure 2.1.

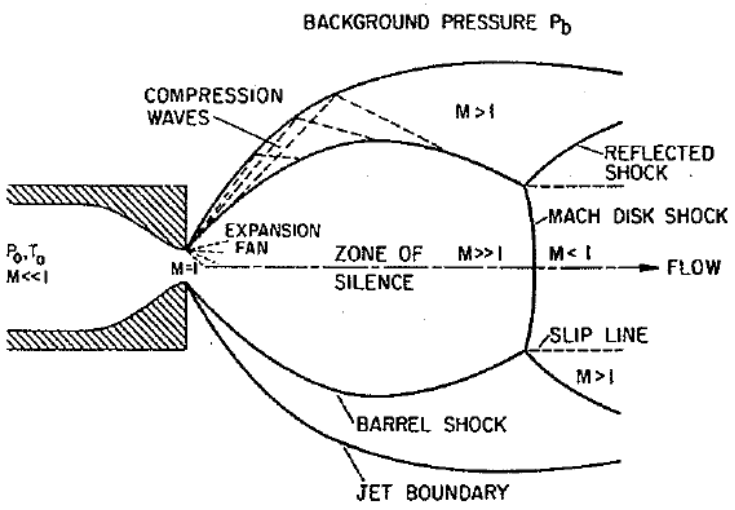

Figure 2.1 – free-jet expansion [41]

All the features and structures in Figure 2.1, depend on continuum fluid mechanics to describe the details of the flow. But here, a simpler and slightly more intuitive explanation will be given. First is the barrel shock, barrel shock forms from the eddies, which in turn forms from velocity difference between the expanding gas and the stagnant background. This region is turbulent, viscous, heat conducting, nonisentropic. These kinds of shock wave regions, including barrel shock, have large density gradients, and hence they can be visualized by light-scattering techniques. These shock regions, to a zeroth order approximation, will reflect any incoming stream of gas, due to their turbulent nature.

Under imperfect expansion conditions, the expanding gas goes through a sequence of expansions and compressions known as the shock-cell structure. In Figure 2.1, we see the first shock-cell, which is bounded by barrel shock, and is terminated by the Mach disk shock. This cell-shock structure will repeat itself indefinitely down the stream, see Figure 2.2.

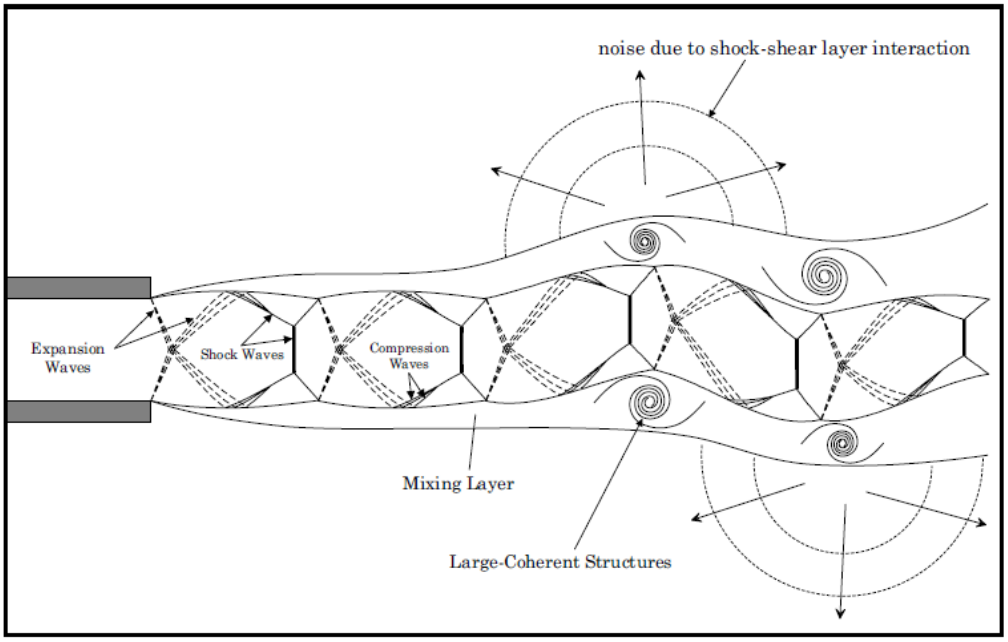

Figure 2.2 – cell-shock structure of free-jet expansion [40]

Mach disk shocks, or Mach disks, are not intuitive to describe, and best way to think about it, is Mach disk shocks are due to boundary conditions when solving Navier stock equations for this system. The Mach disk distance, x_M , from the nozzle, depends on the nozzle diameter, d ,is surprisingly insensitive to γ and is given by

$$(x_M / d) = 0.67\sqrt{P_0 / P_b}$$

Equation 2.4

The term zone of silence is named such, because supersonic flow in this region is not aware of any external conditions, as it travels faster than all the other turbulences and hence not interacting with those turbulences. In zone of silence, there are negligible viscous and heat conduction effects, effectively there are no interactions in this zone, and the beam can be considered to be close to a parallel non-interacting beam.

2.1.3 Skimmed beam

The key of producing a molecular beam, is to place a skimmer inside the zone of silence, before the Mach disk shock occurs. For our nozzle diameter, typically, $d = 250\mu m$, with backing pressure of $P_0 = 10bar$, expanding to a vacuum of $P_b = 1e-6torr$, using Equation 2.4, the Mach disk shock distance from nozzle is $x_M = 0.67d\sqrt{P_0 / P_b} = 14.5meters$. Meaning that theoretically, a skimmer should be placed at distance of $< 14.5meters$ away from nozzle, to avoid complications. In practice, we don't have to worry about this Mach disk shock, since the chamber length is only on the order of meters, and skimmer is placed on the order of tens of centimeters away from the nozzle.

A skimmer is a pinhole, with a cone shaped body. The pinhole is to skim the central beam, which is parallel and non-interacting, from the turbulences and shocks that are created from the free expansion. And the purpose of the cone shaped body is to avoid creating more shocks and turbulences while the beam is being skimmed. Also, by using a skimmer, we isolate the source chamber, which usually have a relatively high pressure, from the second vacuum chamber, which operates at much lower pressure.

With the skimmer in place, we can visualize the supersonic expansion as an isentropic expansion into perfect vacuum and disregard any complicated shock structures. This simplification will ease our task in describing the supersonic expansion, as we only describe the properties of the central beam, which is isentropic and adiabatic. And we don't need to worry about all the complicated structure of the turbulences and shock waves etc, despite that descriptions about those complicated structures do exist.

This adiabatic and isentropic assumption of our beam will lead to the conservation of the sum of the enthalpy and the kinetic energy of beam as the free expansion into vacuum happens[39], ie $H(z) + \frac{1}{2}mv(z)^2 = constant$, where $H(z)$ is the molar enthalpy of the gas at position z from

the nozzle, and $v(z)$ is the average beam velocity at position z. Because of this conservation of energy, the maximum velocity the beam can achieve is given by

$$v_{max} = \sqrt{\frac{2H(T_0)}{m}}$$

Equation 2.5 - where $H(T_0)$ is the enthalpy of the gas at the temperature of the high pressure reservoir, T_0.

For the case of ideal monoatomic gas $C_P = \frac{5}{2}k$, and $H(T) = C_p T$. So now we can write Equation 2.5 as

$$v_{max} = \sqrt{\frac{5kT_0}{m}}$$

Equation 2.6 - k is the Boltzmann's constant, and m is the molecular mass.

Hence the maximum beam velocity, v_{max}, is only determined by the temperature of our nozzle, T_0, given the gas sample.

A quick comparison between Equation 2.6 and Equation 2.2 shows that speed of the beam for supersonic beam is faster than the speed of the effusive beam, ie $v_{\text{supersonic}} = \sqrt{5kT/m}$ compared with $v_{effusive} = \sqrt{2kT/m}$. This increase in the velocity of the beam is undesired, however supersonic beam has other desirable properties, which effusive beam does not have. These desirable properties are, lower temperature of the beam, and narrower velocity distribution of the beam, which we will describe next.

For ideal gas, we have ideal gas law, $pV = nkT$, and for ideal gas change of enthalpy is directly proportional to change in temperature, $dH = C_p dT$, with the proportionality constant of heat capacity, C_p, which is assumed to be independent of temperature. We denote the state before

expansion with (p_0, T_0, ρ_0), where $\rho = n/V$ is the density of the gas. And we denote the state after the free expansion with (p_f, T_f, ρ_f), then it can be derived[39] that

$$\frac{T_f}{T_0} = \left(\frac{p_f}{p_0} \right)^{(\gamma-1)/\gamma}$$

Equation 2.7

From Equation 2.7, we see intuitively that when the pressure drops, as gas expands from high pressure reservoir to low pressure reservoir, the temperature will also drop. This is rather trivial, and this is just a property of adiabatic expansion. However, more detailed description can be derived[39] [41], which expresses (p_f, T_f, ρ_f) in terms of the Mach number $M(z)$, which in turn, depends on the distance the beam has travelled from the nozzle, z.

From Figure 2.1, we can see that the Mach number, defined as

$M = \dfrac{\text{velocity of the beam relative to the background}}{\text{speed of sound in the background}}$, is much greater than 1, $M \gg 1$, in the zone of silence. But more precisely, following expression can be derived [39] [41] to calculate the Mach number, as a function of distance beam has travelled from nozzle, z.

$$M(z) = A\left(\frac{z}{d} - \frac{z_0}{d} \right)^{\gamma-1} - \frac{1}{2} \frac{(\gamma+1)/(\gamma-1)}{A(\frac{z}{d} - \frac{z_0}{d})^{\gamma-1}}$$

Equation 2.8 - z_0/d and A, are related to the flow field properties of the beam, and are experimentally obtained[41], and is different for different gas, depending on the value of γ.

γ	z_0/d	A
5/3	0.075	3.26
7/5	0.40	3.65
9/7	0.86	3.96

Table 2.1 – Values of γ, z_0/d, A, for calculating the Mach number $M(z)$ [39] [41]

For our purpose, we don't care too much about how was this derived, and what is the implication of different Mach number at different regions in Figure 2.1. We merely use it as an equation, in order to calculate the thermodynamic properties of our system. For a free jet expansion, and assuming ideal gas, following thermodynamic properties of the beam can be derived in terms of the Mach number, which is much more descriptive than Equation 2.7

$$\frac{T_f(z)}{T_0} = \left(1 + \frac{\gamma - 1}{2} M(z)^2\right)^{-1}$$

Equation 2.9

$$\frac{p_f(z)}{p_0} = \left(1 + \frac{\gamma - 1}{2} M(z)^2\right)^{-\gamma/(\gamma-1)}$$

Equation 2.10

$$\frac{\rho_f(z)}{\rho_0} = \left(1 + \frac{\gamma - 1}{2} M(z)^2\right)^{-1/(\gamma-1)}$$

Equation 2.11

When we examine Equation 2.9 … Equation 2.11 closer, we see that, the temperature of the beam, together with the pressure and density approaches zero rapidly, when $M \gg 1$, which occurs almost immediately after the free expansion, see Figure 2.1. And indeed, this decrease in temperature is one of the attractive features of supersonic expansion. For example, we can look at the beam properties of a O_2 beam before the skimmer, which is about $z = 10cm$ away from the nozzle. With $d = 250\mu m$, and $\gamma = 7/5$, we use Equation 2.8 and Table 2.1 to get the Mach number at this position, the result is $M(z = 10cm) = 40$. Then we use Equation 2.9, assuming our nozzle is cooled to $T_0 = 130K$, we will get $T_f(z = 10cm) = 400mK$.

For our supersonic beam, we can still approximate it as a Maxwell-Boltzmann distribution, with the central velocity shifted by $v_{max} = \sqrt{5kT_0/m}$, which is maximum supersonic beam velocity, obtained from Equation 2.6. Also, note in, Equation 2.12, we use T_f instead of T_0, which was used in Equation 2.1.

$$f_{supersonic}(v) = 4\pi\left(\frac{m}{2\pi kT_f}\right)^{3/2}(v - v_{\max})^2 exp\left(\frac{-m(v - v_{\max})^2}{2kT_f}\right)$$

Equation 2.12

We can visualize the difference between effusive and supersonic beam, by plotting Equation 2.1 together with Equation 2.12. The parameters used are $T_0 = 130K$, $T_f = 400mK$, and the result is following:

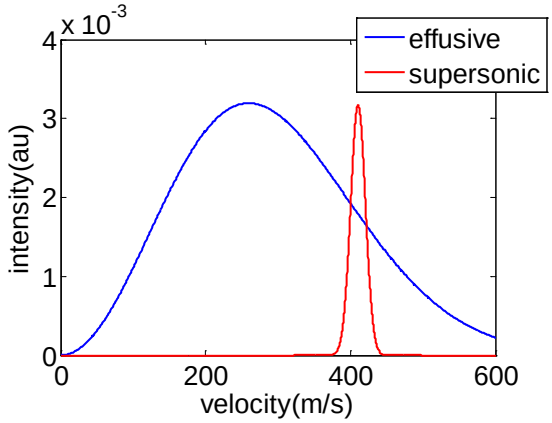

Figure 2.3 – effusive beam vs supersonic beam, with typical values for O2, 130K nozzle. Normalized to the same intensity.

We can examine the properties of the oxygen beam.

For effusive beam, see Equation 2.2, $v_{central} = \sqrt{2kT_0 / m} = 260m/s$, and the width of this distribution is $\sigma_{velocity} = \sqrt{kT_0 / m} = 180m/s$.

For supersonic beam, see Equation 2.6, $v_{central} = v_{max} = \sqrt{5kT_0 / m} = 410m/s$, and the width of this distribution is $\sigma_{velocity} = \sqrt{kT_f / m} = 10m/s$

2.1.4 Pulsed beam

Due to the fact that supersonic expansion requires relatively high pressure in high pressure reservoir, a continuous supersonic beam may cause too much gas load for the vacuum pumps to pump away. One solution to this problem is to use a pulsed supersonic beam. Pulsed

supersonic beam will reduce the gas load to the vacuum considerably, hence achieving a better vacuum. And in the case of Zeeman deceleration, the detection scheme involves pulsed lasers, the deceleration is pulsed magnetic fields, then the natural choice for the source would be pulsed supersonic beam.

One important question when using the pulsed beam is that, how long the nozzle must remain open for a supersonic expansion to fully develop. According to [39], the rule of thumb is that the pulsed nozzle must be fully opened for a time $\Delta t \geq 4d / v_{sound}$ for a supersonic expansion to fully develop. Where d is the diameter of the nozzle, and v_{sound} is the speed of sound in the high pressure reservoir. For ideal gas, the speed of sound is given by $v_{sound} = \sqrt{\gamma kT / m}$. We plug in some typical values for O_2, $\gamma = 7/5$, our nozzle diameter, typically, $d = 250\mu m$, using valve temperature $T = 130 Kelvin$, we get $v_{sound} = \sqrt{\gamma kT / m} = 220 m/s$, and $\Delta t \geq 4.6\mu s = 4d / v_{sound}$. So, in theory, we need to open our nozzle for at least $4.6\mu s$ for supersonic expansion to fully develop, but in practice we open the nozzle much longer than this, $40\mu s ... 80\mu s$, in order to get a higher flux, so that we can detect the beam.

2.1.5 Seeded beam

From Equation 2.6, $v_{max} = \sqrt{5kT_0 / m}$, we see that the velocity of the molecular beam is only determined by the gas sample and the temperature of our nozzle. Most of time, it is desirable to have as low initial velocity as possible. But, in the actual experiment, we have constrains on choosing our gas sample, and constrains on how far we can cool our nozzle. However, if we use a mixture of gas, instead of using pure gas as our sample, then we have another scheme to decrease our initial beam velocity, namely seeding the beam.

To create seeded molecular beam, a small mole fraction of a second species, we call it seeded gas, is added to the gas in the high pressure reservoir, we call it carrier gas. In seeded beams, the seed gas will be accelerated/decelerated to the beam velocity of the carrier gas.

In the limit of high source pressure, p_0, of the carrier gas, the behavior of seeded beam does not deviate from the behavior of unseeded beams. And we treat seeded beams exactly the same as we treated unseeded beams, with a small modification. The modification is, for seeded beam, the molecular weight, m, and heat capacity, C_P, used in our calculations, need to be replaced by the weighted average molecular weight, $\bar{m}$, and heat capacity, $\bar{C}_P$, of the seeded gas and carrier gas. And the weight is simply a weight by molar fraction, X_i, of the seeded gas and carrier gas, as follows

$\bar{m} = \sum X_i m_i$, and $\bar{C}_P = \sum X_i C_{Pi}$

Usually, the carrier gases are one of the noble gases, because of their inert nature. And the seeded gas is our sample that we want to investigate, usually seeded from few percent, to low tens percents. For example, for $20\%\ O_2$ seeded in Ar, $T_0 = 130K$, we get $\bar{m} = 0.8 \times 39.9 + 0.2 \times 32.0 = 38.3amu$. Meaning that, for this seeded beam, the initial velocity of the beam, Equation 2.6, is just $v_{max} = \sqrt{5kT_0 / \bar{m}} = 375m/s$, compared with if we use pure O_2, then the initial beam velocity would be $v_{max} = \sqrt{5kT_0 / m} = 410m/s$.

Using heavier carrier gas will lower the initial velocity, see *Equation 2.6*. However, heavier noble gas, such as Xe, has higher boiling point, and hence the nozzle cannot be cooled down as aggressively as lighter noble gas, such as Ar. Higher nozzle temperature will give higher initial velocity, see *Equation 2.6*, hence a balance has to be found. In practice, we favored Ar over Xe.

An additional quick note here, which is, at low to intermediate source pressure, the heavier molecules tend to lag behind the lighter molecules when expanded, and this phenomenon is called “velocity slip”. The effect of velocity slip might seem to be similar to the effect of insufficient mixing of the gas in the reservoir.

2.2 Longitudinal phase space stability

2.2.1 Introduction to phase space stability

The goal of deceleration of molecular beam is to achieve lowest possible translational velocity, with highest possible phase space density. More precisely, the desire is the highest possible phase space density, which matches the phase space acceptance of the next stage of the experiment, whether it will be another deceleration method, a trap, or detection. Reminding ourselves, phase space is a 6-dimensional space, consisting of $\{x, y, z, v_x, v_y, v_z\}$ degrees of freedom, where $\{x, y, z\}$ are the Cartesian coordinates in space, and $\{v_x, v_y, v_z\}$ is the velocity of molecule in direction of $\{x, y, z\}$. The z -axis is the molecular beam axis.

It is known that conventional decelerator methods, including Zeeman decelerator, cannot compress the phase space density, meaning that in the best case the phase space density is conserved and not decreased over time. The lack of ability to compress phase space is also the reason, why sometimes decelerator techniques are called slowing techniques, instead of cooling techniques.

Unlike accelerators, the decelerator cannot compress phase space, hence the best case scenario for decelerators is the case when phase space volume is conserved. For phase space volume to conserve, the decelerator needs to be operated in a phase stable manner, to achieve phase space stability. And in this section, we take some time to describe what we mean by phase space stability, which is also called phase stability.

Molecules that are in the phase stable volume, due to various physical reasons, have an oscillatory motion around the synchronous molecule in the phase space. Phase stable molecules are desirable, because only phase stable molecules will remain after infinitely long evolution time. And hence only phase stable molecules can be detected after a long deceleration process. And in contrast, molecules that are not phase stable, will not have an oscillatory motion around the synchronous molecule, and will be lost after some finite evolution time, and hence will not be detectable after the deceleration process.

Phase space acceptance, is the region in phase space, which is phase stable before the decelerator. Phase space emittance, is the region in phase space, which is phase stable after the decelerator. These concepts are from accelerator physics, since phase space can be compressed through radiation processes in undulators, and hence the phase space acceptance and phase space emittance are not equal. And since decelerator cannot compress phase space, phase space acceptance, phase space emittance and phase stable area are equal to each other.

We separate the discussion of phase stability into longitudinal phase stability(along z). and transverse phase stability (along x, y).

2.2.2 Longitudinal phase space stability

We begin the discussion with the longitudinal phase stability, because it is less complex, and the discussion of transverse phase stability requires the concepts from longitudinal phase stability. The longitudinal direction is along the z -axis, which is the molecular beam axis, see Figure 2.4. Hence the longitudinal phase space is the 2 dimensional sub space, $\{z, v_z\}$, of the total 6 dimensional phase space.

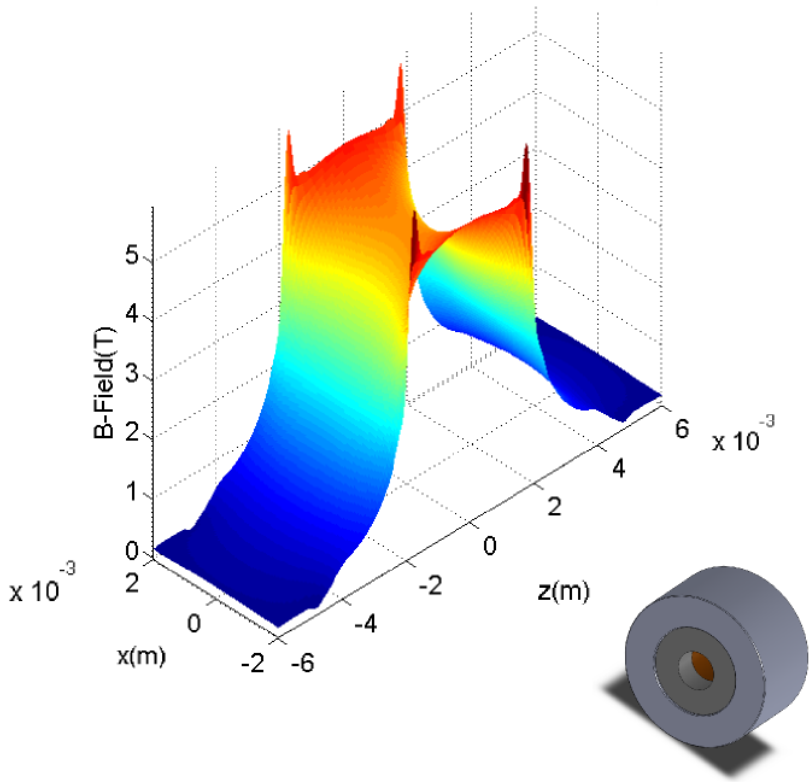

Figure 2.4 – showing the z-axis, which is along and equal to the molecular beam axis. We call the direction along z-axis the longitudinal direction. x and y axis are in the plane perpendicular to z-axis, and we call it the transverse direction.

One of the longitudinally phase stable mode of operation is, that we remove the same amount of kinetic energy of the synchronous molecule at each stage of the decelerator. In practice there are always noise and instability from the experiment, but here we assume each stage of deceleration is behaves identically, we also assume the coils can switch off instantaneously, to simplify the discussion. In reality, the coils have $4...6\mu s$ decay time from peak current to zero current, due to inductance and Eddy currents.

The synchronous molecule has the initial velocity, v_0, and we choose the switching phase to be ϕ_0. And the synchronous molecule will lose $\Delta E_{kinetic}$ amount of kinetic energy, determined by the switching phase ϕ_0.

We define switching phase, ϕ_0 ,from 0 degrees to 90 degrees. $\phi_0 = 0^\circ$ switching phase is when coil is switched off when synchronous molecule is between two coils, see Figure 2.5, where the field is at minimum, which results in no deceleration, but produces largest number of phase stable molecules. And, $\phi_0 = 90^\circ$ switching phase is when coil is switched off when synchronous molecule is in the middle of the coil, see Figure 2.5, which results in greatest amount of deceleration, but produces smallest number of phase stable molecule.

For molecules other than the synchronous molecule, $\Delta E_{kinetic}$ is different for each molecule, and $\Delta E_{kinetic}$ only depends on the relative phase, $\Delta\phi = \phi - \phi_0$, of the molecule. ϕ is the absolute phase of the molecule in question. In other words, $\Delta E_{kinetic}$ of a molecule depends on the relative distance in z between the molecule in question and the synchronous molecule.

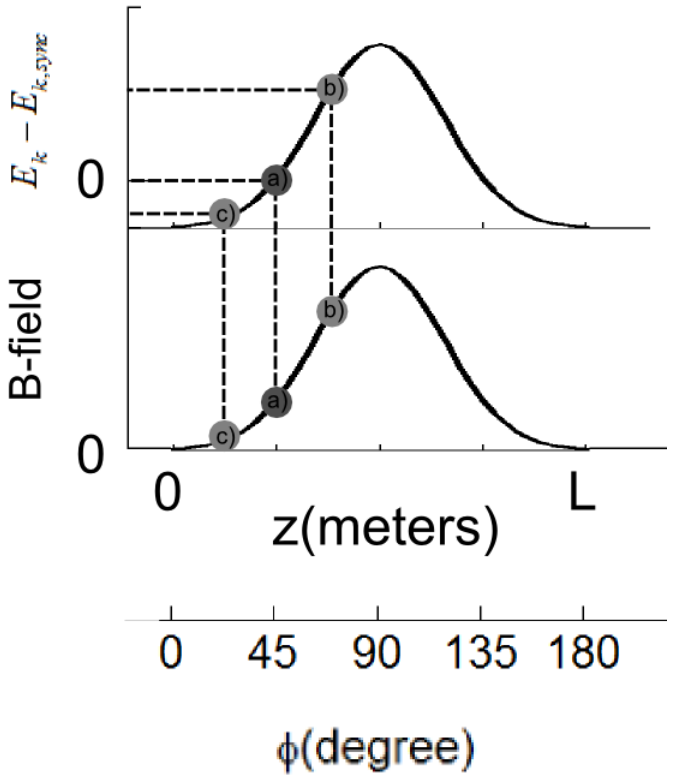

Figure 2.5 - The change in kinetic energy relative to the synchronous molecule, due to the B-field generated by the coil for a) the synchronous molecule at $\phi_0 = 45^\circ$, b) a molecule with higher phase than the synchronous molecule and c) a molecule with lower phase than the synchronous molecule. L is the length of the coil. Note that this diagram is a sketch, does not present the actual shape of the curves.

The key concept of longitudinal phase stability is following. Let's assume all non-synchronous molecules have the same initial velocity, v_0, as the synchronous molecule. We are switching the coils at a constant phase, ϕ_0, plus the fact that the coils in the decelerator are equally spaced to one another, and hence, the synchronous molecule will always travel the same distance L, from stage to stage.

However, for a molecule that has slightly higher phase $\phi = \phi_0 + \Delta\phi$, it will experience more loss in kinetic energy relative to the synchronous molecule, hence it has lower velocity relative to the synchronous molecule. Having a lower velocity means that the molecule will have moved less distance, into the second coil than the synchronous particle, by the time the second coil is switched. Resulting in the molecule now has a phase $\phi = \phi_0 - \Delta\phi$ which is lower than the synchronous molecule.

In summary, over the length of the decelerator, for molecules that have higher (lower) phase angle than ϕ_0, the molecule starts losing (gaining) phase angle and velocity relative to the synchronous molecule until it reaches the same phase angle as ϕ_0. And this results in an oscillatory motion of non synchronous molecule around the synchronous molecule, we call molecules undergoing this oscillatory motion the longitudinally phase stable molecules.

2.2.3 Separatrix in longitudinal phase stability

The molecules are longitudinally stable, only if they are sufficiently close the synchronous molecule in z, ie if $\Delta\phi$ is sufficiently small. As long as $\Delta\phi$ is sufficiently small, we can develop

an approximate analytical description, by assuming that the average effective force acting on a nonsynchronous molecule is

$$F(z_0+\Delta z)\approx -\frac{1}{L}[W(z_0+\Delta z)-W(z_0)]$$

Equation 2.13 - where $W(z)$ *is the effective magnetic potential energy at the position* $z=\frac{L}{\pi}\phi$, L *is the distance between adjacent coils.*

We can approximate $W(z)$ as a single gaussian function, with fitted parameters a,b and c

$$W(z)=a\exp\left[-\frac{(z-b)^2}{2c^2}\right]$$

Equation 2.14

Which corresponds to our coil, inner coil diameter $4mm$, $5\times 6=30$ windings, current $=600A$, $\text{B-field}_{max}=4.27Tesla$, distance between adjacent coils $L=12mm$.

For O_2, $|N''=1,\text{J}''=2,\text{m}_{J''}=2\rangle$, $a=8.1\text{e-}23joules$, $b=6mm$, $c=1.86mm$.

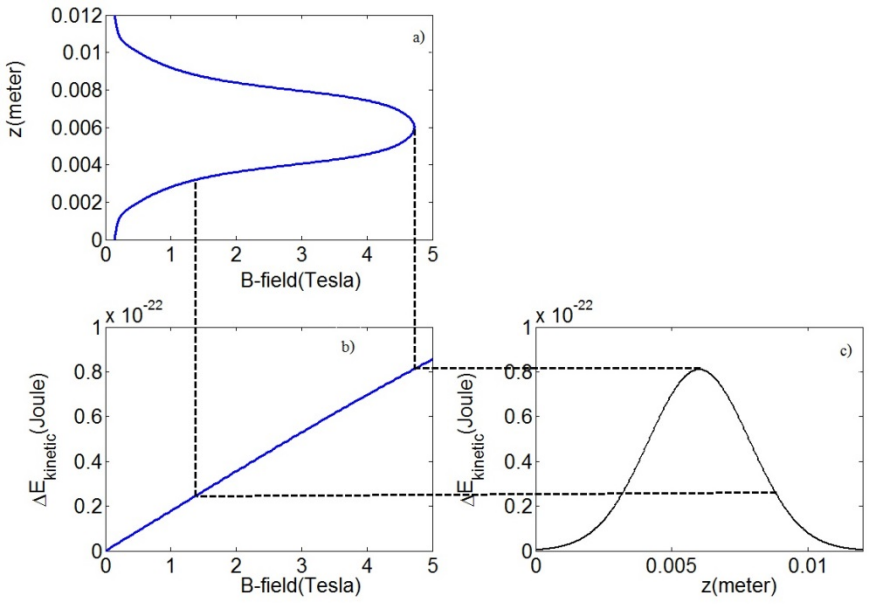

Figure 2.6 - The effective magnetic potential energy $W(z)$ is the combination of the strength of the B-field, and the Zeeman shift of the particular level, in this case the level is O_2, $|N''=1,J''=2,m_{J''}=2\rangle$ We see the peak field 4.27T in a) corresponds to 8.1e-23joules in c).

And finally, using Equation 2.13 and Equation 2.14, the equation of motion , $acceleration = \frac{Force}{mass}$, of nonsynchronous molecule can then be written as

$$\frac{d^2\Delta z}{dt^2} = \frac{1}{m}\frac{1}{L}[W(z_0 - \Delta z) - W(z_0)]$$

Equation 2.15 - where $W(z)$ is defined in Equation 2.14.

A note to the reader, Equation 2.15 compared with equation used in ref [42], are not identical. There is a factor of L difference, since we preferred to work in relative positions in Equation 2.15, Δz, instead of relative phases, $\Delta\phi$, as in ref [42].

Phase space is a state space, a space in which all possible states of a system are represented, and the dynamics in a state space is fully defined by its state, and does not depend on the path which led to the state. Hence Equation 2.15 fully characterizes the 2 dimensional phase space of $\{z, v_z\}$.

The parameter z_0 in Equation 2.15 is actually the switching phase, $\phi = \frac{\pi}{L}z$, that needs to be optimized to have as large phase stability as possible. In order to examine the properties of Equation 2.15 and to optimize ϕ_0, we first transform the coordinate from $\{z, v_z\}$ into $\{\Delta z = z - z_0, \Delta v_z = v_z - v_{z0}\}$, for clarity. And then we plot various values of ϕ_0.

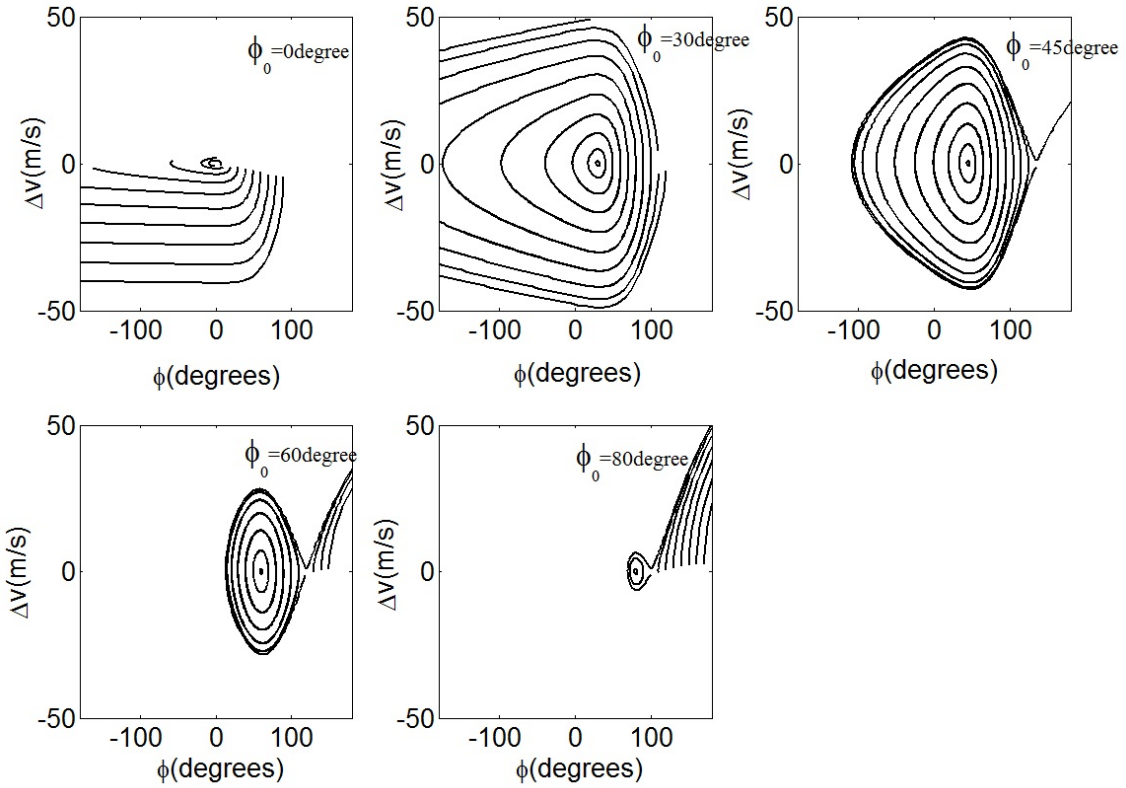

Figure 2.7 – phase space evolution for various ϕ_0, total time for evolution is 3ms, coil center is at $+90^\circ$. The initial conditions used, for each plot in , are $\Delta v_{z,init} = 0$ and $\Delta\phi_{init} = \phi_{init} - \phi_0 = +10^\circ, +20^\circ \ldots + 80^\circ, +90^\circ$, and the evolution is governed by Equation 2.15.

In the phase space, see Figure 2.7, molecule rotates clockwise, similar to a harmonic oscillator. Closed paths indicate that the motion of molecule is phase stable, while open paths indicate the motion of molecule is not phase stable. The closed curve enclosing the largest area is called the separatrix. All the molecules inside the separatrix are phase stable, and all the molecules outside the separatrix are not phase stable.

For low switching phase of synchronous molecule, $\phi_0 = 0^\circ$, the oscillatory motion is slow, due to field gradient is small at low switching phase. And due to the slow oscillatory motion, the non synchronous molecules do not complete even one full oscillation, before the beam reaches the end of the decelerator, which is $\sim 3ms$. Hence, we cannot say they are phase stable. In theory,

if we have an infinitely long decelerator, $\phi_0 = 0^\circ$ would yield the largest phase stable area relative to other plots in Figure 2.7.

As we increase the switching phase ϕ_0, the oscillation motion become more rapid, which eliminates the problem described in the paragraph above. However, non synchronous molecules with too large relative phase will get accelerated, and will be lost. The condition for too large relative phase is approximately

$$\Delta\phi > 90^\circ + (90^\circ - \phi_0)$$

Equation 2.16

Due to Equation 2.16, the more we increase the switching phase ϕ_0, the more molecules will be lost, and hence the smaller phase stable area.

We also need to remember, larger switching phase leads to larger deceleration, since the molecules will climb up the potential hill more, before the potential hill is switched off. Also, the right switching phase is a balance of these factors, which is found by trial and error, since it depends on the shape of the magnetic field, and the Zeeman shift of the level one chose to use, and the coupling between longitudinal motion and transverse motion.

For example, our field the field is noticeably compressed (3x less in width) compared with the field used by Wiederkehr [42], see Figure 2.8, due to the permendur shielding of the coil.

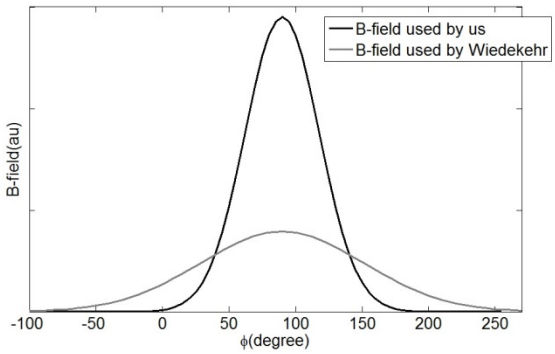

Figure 2.8 – comparison between our B-field and B-field used by Wiederkehr [42]

This compression decreases the phase stable area, due to Equation 2.16, which is unavoidable. This difference in field also affect the result of the analysis, in ref [42] $\phi_0 = 0^\circ$ *yielded the largest phase stable area, however for us, the oscillation in* $\phi_0 = 0^\circ$ *is too slow, and* $\phi_0 = 30^\circ$ *yielded the largest phase stable area, see Figure 2.7.*

For the sake of comparison, comparing our separatrix, *Figure 2.7*, to the separatrix of FIG. 3. of ref [42]: we see that they (ref [42]) have to decelerate at $\phi_0 \approx 60^\circ$, and we only have to decelerate at $\phi_0 \approx 45^\circ$, in order to achieve the same amount of deceleration. At these conditions, their phase stable area is about $(\pm 30 m/s) \times (5.5 mm) = 330 mm\ m/s$, and our phase stable area is about $(\pm 45 m/s) \times (12 mm) = 1080 mm\ m/s$. (We have roughly assumed the phase stable area is a square: area=height$\times$width) Larger phase stable area is more desirable, and hence this shows the advantage of using bigger B-fields and shielding materials around the coils (gives $\sim 3\times$ bigger phase stable area vs lower field plus unshielded coils of similar geometry)

Comparison with longitudinal phase stability of Stark decelerator [43] reveals that for Stark decelerator, there is an array of phase stable areas, whereas in our Zeeman decelerator, there is only one phase stable area. The reason is, Stark electrodes are in an array, and the whole array is switched at once, whereas in Zeeman, only one coil is switched at a time.

We can, and we should compare the analysis so far with our numerical simulation. The result of the comparison is shown in Figure 2.9.

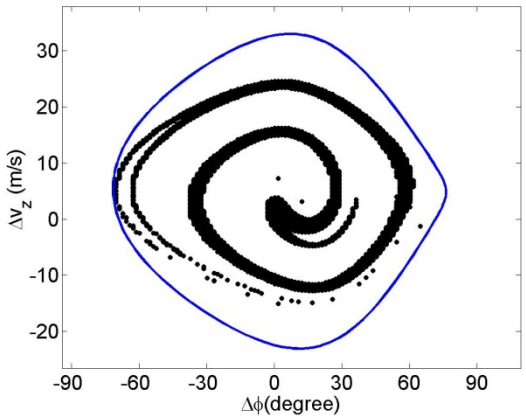

Figure 2.9 – comparison between the separatrix from Equation 2.15 (blue), with numerical simulation (black) (see Appendix D) of the phase space of the decelerated packet of O_2, $|N''=1,\mathrm{J}''=2,\mathrm{m}_{J''}=2\rangle$, $\phi_0=53^\circ$, *80 stages, 600Amps.*

The result is encouraging. However, the molecules from numerical simulation do not fill the separatrix. The reason is, the analysis of longitudinal phase stability is simplification, as it ignores the transverse degree of freedom. Hence, if we simplify numerical simulation to ignore transverse motion , then the simulation and separatrix can be shown to match extremely well [44].

In summary, the longitudinal phase stability analysis depends on the shape of the B-field, and the Zeeman shift of the quantum state we are trying to decelerate. However, in general, the larger the switching phase ϕ_0, the smaller the phase stable area, which is undesirable. However, we need to note that the larger the switching phase ϕ_0, the slower the final velocity of the beam, which is desirable. The balance is found to be $\phi_0=45^\circ\sim55^\circ$, which is comparable with literature. And the size of the phase stable area in z is roughly comparable to the size of the coil.

2.3 Transverse phase space stability

The total phase space is a 6-dimensional space, consisting of $\{x, y, z, v_x, v_y, v_z\}$ degrees of freedom, where z -axis is the longitudinal direction, and x, y -axis is the transverse direction. The transverse phase space is a 4-dimensional space, consisting of $\{x, y, v_x, v_y\}$. In Zeeman decelerator, the B-field is cylindrically symmetric about the z -axis, hence the motion in x -axis is identical to the motion in y -axis. Therefore, we need only to analyze the motion in one of the degree of freedom, let's say in x , and analysis in the other transverse direction, y , would be the same as in x . And hence our task simplifies to the analysis of $\{x, v_x\}$.

Analysis of coupling of longitudinal motion and the transverse motion is important to understand the structures of the decelerated molecules in phase space. As we saw previously, in Figure 2.9, the distribution of molecules inside the separatrix is not uniform. And in this section, we try to give more insight into why and how this coupling of transverse motion and longitudinal give rise to the non uniform structure we see in Figure 2.9.

In summary, there are two aspects of transverse motion. The first aspect being the characterization of initial transverse velocity distribution, $\Delta v_{x,init}$. And the second aspect is the coupling of longitudinal motion and the transverse motion.

2.3.1 Characterization of initial transverse velocity distribution

The characterization of initial transverse velocity distribution is important, because the initial transverse velocity distribution affects the focal point of the beam, the accuracy of numerical simulation, experimental design, for example the design of magnetic hexapole guide etc. According to simulation of ref [18], phase space can differ as much as 5x in density, by manipulating transverse velocity distribution by magnetic hexapole guides, and by placing detection at the focal point of beam.

In fact, there are numerous publications which have noted the importance of the characterization of transverse velocity distribution. For example, in ref [30], the transverse velocity distribution was directly measured by a MCP equipped with a phosphor screen, with CCD camera behind it. And the transverse velocity distribution was determined to be $5...10mK$ for metastable neon, by varying the position of detector, and recording spatially, x, y, resolved distribution.

Another method, other than the direct imaging, can also be used to estimate the initial transverse velocity distribution. In ref [18], ND_3 was decelerated using Stark decelerator, and the initial transverse velocity distribution was determined by matching the time integration signal intensity with the simulation. The result was $11...18mK$.

For out experiment, we adopted a similar approach as ref [18]. However, instead of matching the time integration signal intensity with the simulation, we matched the relative signal intensity of decelerated beam versus free flight beam, with simulation. The result is comparable with literature, and is about $\sim 10mK$.

2.3.2 Focal point of magnetic lens

The Zeeman coils will act like a magnetic lens, due to its concave shape in the transverse direction. The focal point is the most important property to know about the magnetic lens. For example, ideally, the focal point of the beam would coincide with the detection laser, yielding larger signals. Here, we introduce a method to calculate the focal point of a magnetic lens without resulting to numerical simulation.

The focal point, f ,of a magnetic lens was given by ref [45], as

$$f = \frac{DE_{kin}}{\mu_B \beta L}$$

Equation 2.17

For our magnetic lens, typical values are: $\beta = dB/dz = 2T/cm$ is our typical field gradient, $D = 6.35mm$ is the inner diameter of the magnetic lens, $L = 3.2mm$ is the thickness of the magnetic lens. $\mu_B = \mu_{eff} = 1.64Debye = 5.47e-30Cm$ for $O_2, |N'' = 1, J'' = 1, m_{J''} = 1\rangle$ is the effective magnetic moment. $E_{kin} = \frac{1}{2}mv_z^2$, is the kinetic energy in the longitudinal direction. The effective magnetic moment of quantum level can be determined by $\Delta U_{zeeman} = \mu_{eff} B_{ext}$, where ΔU_{zeeman} is the Zeeman shift, due the external magnetic field B_{ext}.

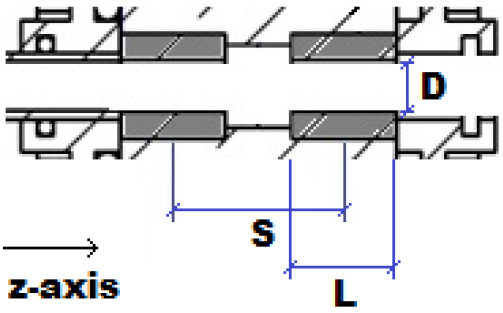

Figure 2.10 – magnetic focuser design,grey areas are neodymium ring magnets. This magnetic lens was designed, but was not used in the final experimental setup.

In our actual design, we ended up with a dual ring magnet design, the spacing between two magnets were $S = 4mm$. For a rough estimate, we can use thin lens formula, which doesn't depend on S

$$\frac{1}{f_{tot}} = \frac{1}{f_1} + \frac{1}{f_2}$$

Equation 2.18

In our case, since two magnets are identical, $f_1 = f_2$. For $O_2, |N'' = 1, J'' = 1, m_{J''} = 1\rangle$, $v_z = 150m/s$, the result from combining Equation 2.17 and Equation 2.18 is $f_{tot} = 50mm$. This result is comparable with the result obtained from numerical simulation, which gave the result of $f_{tot} = 60mm$. Hence we can turn to Equation 2.17 for quick estimations about focal points, instead of using more time consuming numerical simulation.

2.3.3 The transfer matrix method

Due to the coupling between the transverse motion to the longitudinal motion, we have a threshold longitudinal velocity, below which excessive focusing occurs, and phase space density rapidly decreases, see FIG 7 in ref [19]. To obtain a more quantitative value for the threshold longitudinal velocity, we use the method of analysis described in ref [19], which is called the transfer matrix method.

In our model, the transverse force on a molecule in the decelerator has periodicity $2sL$. The molecules repeatedly experience a constant transverse focusing force, F_x, following by a section of free flight. The sections for focusing and free flight are approximated to have equal length sL. See Figure 2.11. We can see that Figure 2.11 approximates transverse force due to the B-field of the actual coil, Figure 2.12.

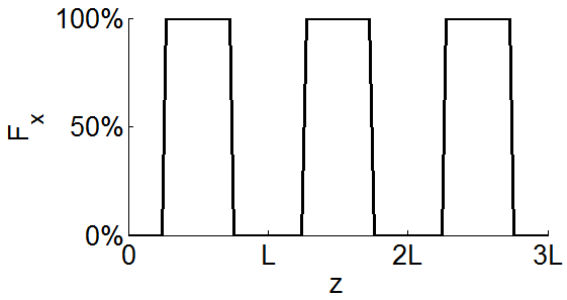

Figure 2.11 – transverse force molecule experiences as it travels down the decelerator in the transfer matrix model. The transverse force is assumed to be constant around the middle of the coil, and no force in between the coils. L is the length of the coil

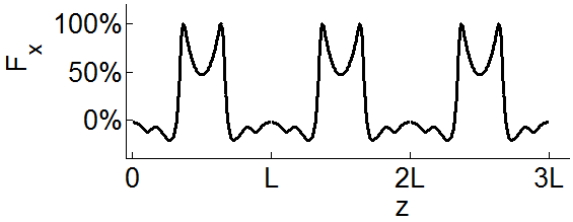

Figure 2.12 – The approximate shape of the transverse force due to the B-field of the actual coil.

For one stage of the decelerator (ie one period), we can map the initial state, $\begin{pmatrix} x_{init} \\ v_{x,init} \end{pmatrix}$, to the final state, $\begin{pmatrix} x_{final} \\ v_{x,final} \end{pmatrix}$, by using a transfer matrix M :

$$\begin{pmatrix} x_{final} \\ v_{x,final} \end{pmatrix} = M \begin{pmatrix} x_{init} \\ v_{x,init} \end{pmatrix}$$

Equation 2.19

For the free flight within one period, $M_{freeflight}$ is defined as:

$$\begin{pmatrix} x_{final} \\ v_{x,final} \end{pmatrix} = \begin{pmatrix} 1 & T \\ 0 & 1 \end{pmatrix} \begin{pmatrix} x_{init} \\ v_{x,init} \end{pmatrix}$$

Equation 2.20 - with $T = \frac{sL}{\langle v_z \rangle}$*, where* L *is the coil to coil distance, and* $\langle v_z \rangle$ *is the mean (or typical) longitudinal velocity, and* s *is the mode of operation.*

For the constant force within one period, $M_{constantforce}$ is defined as:

$$\begin{pmatrix} x_{final} \\ v_{x,final} \end{pmatrix} = \begin{pmatrix} \cos(\Omega_x T) & \frac{1}{\Omega_x}\sin(\Omega_x T) \\ -\Omega_x \sin(\Omega_x T) & \cos(\Omega_x T) \end{pmatrix} \begin{pmatrix} x_{init} \\ v_{x,init} \end{pmatrix}$$

Equation 2.21 - with Ω_x *the transverse oscillation frequency, and other terms are defined same as Equation 2.20.*

The transfer matrix of one coil stage, M_{tot} , is the product of the two transfer matrices in Equation 2.20 and Equation 2.21.

$$M_{tot} = M_{freeflight} M_{constantforce}$$

Equation 2.22

Reminding ourselves that Equation 2.22 describes the motion after one stage, the motion after n numbers of stages are described by $(M_{tot})^n$. The trajectories of the molecules through an infinite number of stages are stable (see derivation on the end of this section) if

$$-2 \le Tr(M_{tot}) \le 2$$

Equation 2.23

We plug in the expressions from Equation 2.20, Equation 2.21 and Equation 2.22 into Equation 2.23, to get our final form of our stability requirement.

$$\left| 2\cos\left(\frac{\Omega_x sL}{\langle v_z \rangle}\right) - \frac{\Omega_x sL}{\langle v_z \rangle}\sin\left(\frac{\Omega_x sL}{\langle v_z \rangle}\right) \right| \le 2$$

Equation 2.24

For our system, coil to coil distance is $L = 12mm$. We complete a cycle of constant force and free flight in distance L, so by definition $s = \frac{1}{2}$. Transverse oscillation frequency $\Omega_x = 10e3rad/s$ for O_2 in $|N'' = 1, J'' = 2, m_{J''} = 2\rangle$ state, see below on calculation of Ω_x. With these parameters plugged into Equation 2.24, we get $\langle v_z \rangle \ge 35m/s$, see Figure 2.13。

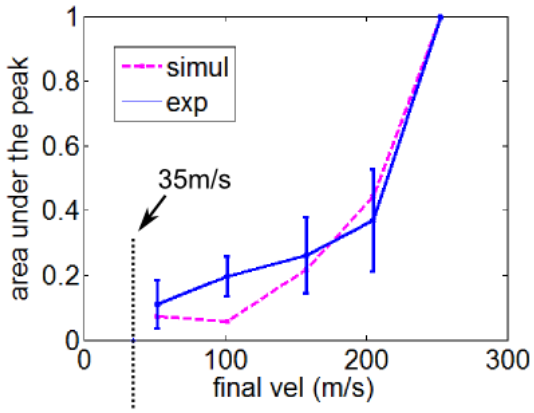

Figure 2.13 – threshold longitudinal velocity predicted by this model, indicated by the black dashed lines, and the experimental result. In the experiment, several attempts have been made to see decelerated packet below 52m/s, but in the end we didn't manage to see any signal below 52m/s in the experiment.

The only difference between this analysis, and the analysis of ref [19] are the values of the parameters used. For our analysis, operation mode is $s=\frac{1}{2}$ instead of $s=3$; coil to coil distance is $L=12mm$, instead of $8.25mm$; and $\Omega_x=10e3rad/s$ instead of $6.4e3rad/s$. It is coincidental that the Stark deceleration of noble gases [19] and Zeeman deceleration of O_2 ended up having similar values for Ω_x , despite the field gradients, deceleration design, and mass of the molecule/atom are quite different.

This analysis is valuable, because the threshold longitudinal velocity this model predicts, has also been verified by other experimental results, see ref [19]. And, for our system, this model predicts that the threshold velocity is $\langle v_z\rangle=35m/s$, for O_2 in $|N''=1,J''=2,m_{J''}=2\rangle$ state, under which excess transverse focusing occurs, and phase space density rapidly decreases.

2.3.3.1 Calculation of transverse oscillation frequency

In order to calculate the transverse oscillation frequency, Ω_x, we use the Zeeman shift (see Section 2.8), dU/dB, of the target state, $|N''=1,J''=2,m_{J''}=2\rangle$, and multiply with the B-field at the center of the coil, see Figure 2.14, to get the transverse force, F_x:

$$F_x(x)=dU/dB\times dB(x)/dx$$

Equation 2.25

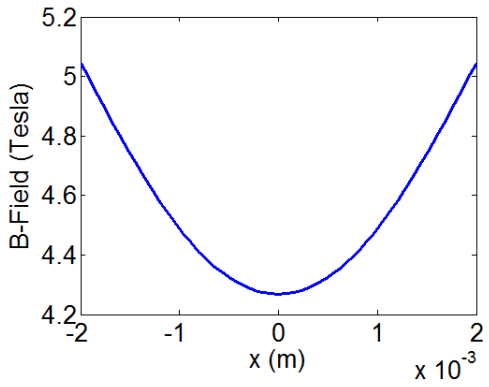

Figure 2.14 – The B-Field at the center of the coil in the transverse direction, which is a function of x. $\{z = \text{center of the coil}, y = 0mm\}$

From Equation 2.25, we see the transverse force F_x depends on x. We assume a simple spring model, such that there is no restoring force when the molecule is at the beam axis, $F_x(x = 0mm) = 0Newtons$.

Next step, we convert F_x to ω_x, in our simple spring model, so that the spring constant $k_x(x) = -\frac{\Delta F_x(x)}{\Delta x}$, and the transverse oscillation frequency $\omega_x(x) = \sqrt{\frac{k_x(x)}{m}}$. Now for the result, we have the transverse oscillation frequency ω_x as a function of our transverse position x, see Figure 2.15. And the range of ω_x is $9.3e3rad/s \sim 11.6e3rad/s$, we then take average of $9.3e3rad/s \sim 11.6e3rad/s$, which is $\omega_x \sim 10e3rad/s$, to be our estimate transverse oscillation frequency, which is used in calculations above.

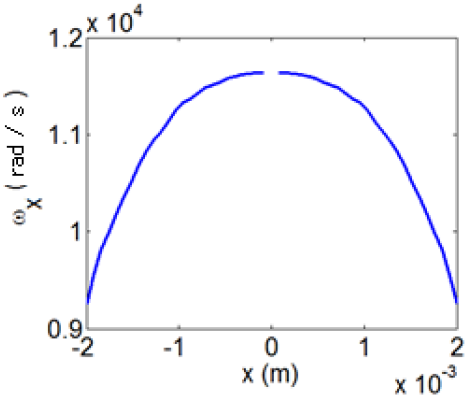

Figure 2.15 – the transverse oscillation frequency, ω_x, as a function of transverse position x. Assuming simple spring model, and assuming center of the coil is good representative of transverse forces. The rough average of transverse oscillation frequency is $\omega_x \sim 10e3rad/s$

2.3.3.2 Stability condition for transfer matrix method

As a side note, we want to present here the central idea of derivation of the stability condition of $-2 \le Tr(M) \le 2$. In the transfer matrix method above, we map our initial state, $\{x_0, v_0\}$, to the a state $\{x_n, v_n\}$ by using the transfer matrix M, n times, ie

$$M^n \begin{pmatrix} x_0 \\ v_0 \end{pmatrix} = \begin{pmatrix} x_n \\ v_n \end{pmatrix}$$

Equation 2.26

Now, suppose that the eigen vectors of M are m_1 and m_2, with eigen values λ_1 and λ_2, ie

$$Mm_1 = \lambda_1 m_1 \quad , \quad Mm_2 = \lambda_2 m_2$$

Equation 2.27

Using Equation 2.26 and Equation 2.27, and with some simple linear algebra, we can derive the following result

$$\begin{pmatrix} x_n \\ v_n \end{pmatrix} = c_1 \lambda_1^n m_1 + c_2 \lambda_2^n m_2$$

Equation 2.28 - where c_1 and c_2 are constant.

And here, we see the main idea of the derivation in Equation 2.28. We require that x_n and v_n stay finite as $n \to \infty$ for stable molecules, meaning that position and velocity must not diverge after travelling through $n \to \infty$ of stages. In other words λ_1^n and λ_2^n must not diverge as $n \to \infty$, hence $|\lambda_1| \le 1$ and $|\lambda_2| \le 1$. And with some further math, we will eventually arrive at the result of $-2 \le Tr(M) \le 2$. For details of the derivation, please see ref [46].

2.3.4 The Mathieu stability diagram method

There is another method, in addition to the transfer matrix method described above, to analyze the coupling of transverse and longitudinal motion. In ref [47], Mathieu stability diagram was used to model the coupling of transverse and longitudinal motion.

The difference between the Mathieu stability diagram and transfer matrix method is that different models of transverse force vs longitudinal position is assumed. In the Mathieu stability diagram analysis, we assume the transverse force varies sinusoidally, see Figure 2.16, opposed to the step function variation in Figure 2.11.

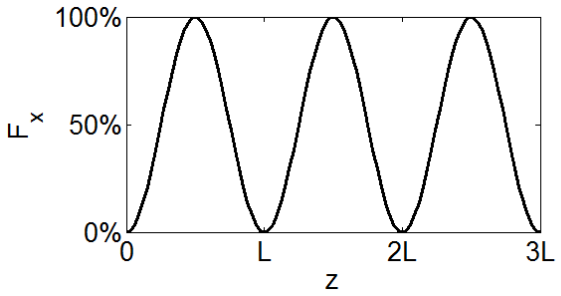

Figure 2.16 – Transverse force experienced by the molecule is assumed to be sinusoidal as the molecule is flying through the decelerator. The transverse force is strongest in the middle of the coil, and the transverse force is zero in between the coil. L is the length of a coil. Oscillation period is assumed to be L. Compare this to Figure 2.11 and Figure 2.12.

With this assumption of sinusoidal variation in transverse force with respect to the longitudinal position, we can use the Mathieu equation to model our system. The Mathieu equation has the general form of:

$$\frac{d^2x}{dt^2}+[a-2q\cos(t)]x=0$$

Equation 2.29 - where a and q are constants

We can compare Equation 2.29 to the equation of motion for harmonic oscillator,

$\frac{d^2x}{dt^2}+\omega^2x=0$, and note that Equation 2.29 very similar to a harmonic oscillator. Instead of

having a constant period of oscillation, $\omega^2 = \text{constant}$, we now have an oscillation which varies sinusoidally as molecule travels down the decelerator $\omega^2 = [a + q\cos(t)]$, where a and q are constants.

We need to assume the longitudinal frequency, $\frac{\omega_z}{2\pi}$ (see Section 2.3.3.1), does not depend on the transverse position of the molecule. And we also need to assume the decelerator is operated at phase angle $\phi_0 > 90^\circ$, because if we switch off the field at $\phi_0 < 90^\circ$, the molecule will not experience the transversely focusing force, which is strongest at the middle of the coil, $\phi \sim 90^\circ$. For reference, in ref [47], the requirement is $\phi_0 \sim 0^\circ$ for the same reason.

With these assumptions, we can approximate transverse force $F_x \propto \omega_x^2(t)$ to be a sinusoidally oscillating function, and enabling the analysis using Mathieu's equation. We can set $mass = 1$, and we write the sinusoidal oscillation of the force as constant force, ω_0^2, which oscillates at the frequency $\omega_z / 2\pi$, with an amplitude of A

$$\omega_x^2(t) = \omega_0^2 - A\cos\left(2\frac{\omega_z t}{2}\right) \propto F_x$$

Equation 2.30

The transverse frequency, ω_x, oscillates once over the distance L. In ref [47], ω_x oscillates twice, because in Stark deceleration L is defined over 2 sets of electrodes. And hence we have a factor of 2 difference inside cosine in *Equation 2.30*.

Using *Equation 2.30*, the equation of motion of our system is then

$$\frac{d^2x}{dt^2} + \left[\omega_0^2 - A\cos\left(2\frac{\omega_z t}{2}\right)\right]x = 0$$

Equation 2.31

And we can transform this into the Mathieu's equation's form:

$$\frac{d^2x}{d\tau^2}+\left[a-2q\ cos(2\tau)\right]x=0$$

Equation 2.32

Where $a=\left(\frac{2\omega_0}{\omega_z}\right)^2$, $q=\frac{2A}{\omega_z^2}$, $\tau=\frac{\omega_z t}{2}$.

Equation 2.33

Depending on the values of a and q, the solutions of the Mathieu equation will exhibit stable or unstable behavior. The 2D plot of a vs q is called Mathieu stability diagram. The key point is, in Equation 2.32, the longitudinal oscillation frequency ω_z is a function of the longitudinal position z, $\omega_z \rightarrow \omega_z(z)$, calculation is very similar to the calculation of transverse oscillation frequency. Hence, a and q are also function of z, ie $a \rightarrow a(z)$ and $q \rightarrow q(z)$. Hence, $a(z)$ and $q(z)$ are essentially a pair of parametric equations with parameter z, and the set of points $\{a(z), q(z)\}$ form a curved line in the stability diagram.

The values the longitudinal position, z, can be obtained from the longitudinal phase space region we want to analyze, which is the region inside the longitudinal separatrix. And we will see that the ring structure inside the separatrix maps onto the stable and unstable regions of the Mathieu stability diagram.

We now apply this model to our system. For $O_2\ |N''=1,\mathrm{J}''=2,\mathrm{m}_{J''}=2\rangle$, $\phi_0=150^\circ$, and for our coil design, we can calculate the longitudinal oscillation frequency, ω_z, using Equation 2.36, see Figure 2.17 below.

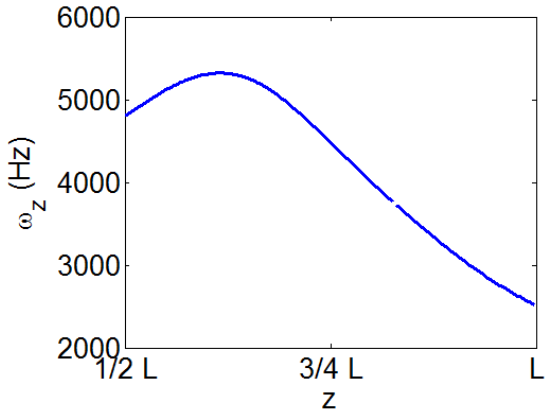

Figure 2.17 - longitudinal oscillation frequency, for $O_2 \mid N'' = 1, J'' = 2, m_{J''} = 2\rangle$, $\phi_0 = 150^\circ$.

We get the sinusoidal transverse oscillation frequency using Figure 2.16, with the function maximum assumed to be $10e3rad/s$, see Figure 2.15. And function minimum assumed to be $0rad/s$.With these assumptions and by using Equation 2.30, we get $\omega_0 = 7.1e3rad/s$ and $A = (7.1e3rad/s)^2$.

Now, we have values for ω_z, ω_0 and A, hence we have everything we need to construct our stability diagram, from Equation 2.32 and Equation 2.33.

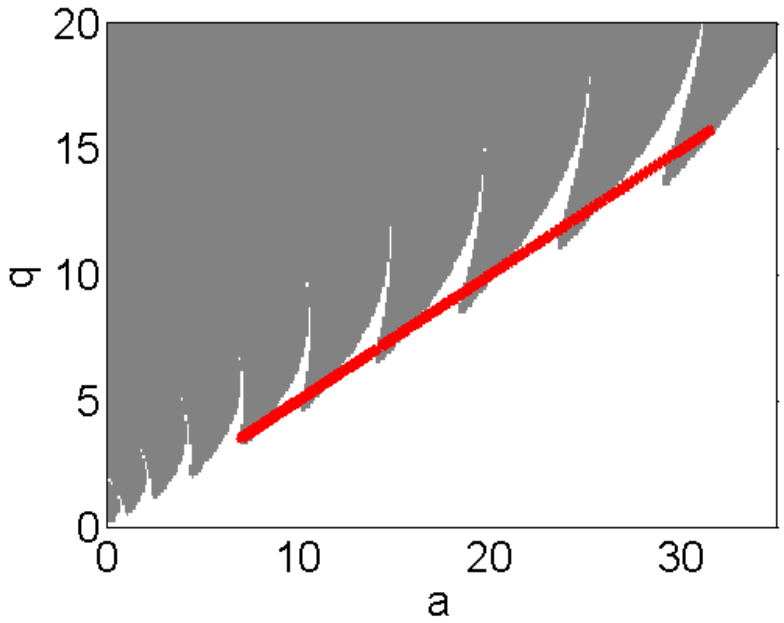

Figure 2.18 – Mathieu stability diagram, the white area indicates stable area, and the grey area indicates unstable area. The red curve is the trace we make when we vary z. The curve comes in from high values of a and q, turns around at {a=7, q=3.5} and heads towards high values of a and q. The curve completely overlaps itself.

In the stability diagram above, a vs q, see Figure 2.18, we see the $\{a(z), q(z)\}$ maps out a curve, with varying z. We constrain the longitudinal position to be $z = \frac{L}{2}...L$, due to the $\phi_0 < 90^\circ$ assumption above. Along the $\{a(z), q(z)\}$ curve, alternating stable region and unstable region can be observed. In the stable region, the oscillations in x remain finite, see *Figure 2.19*, which means the transverse oscillations and the longitudinal oscillations are in sync. For unstable regions, transverse oscillations and the longitudinal oscillations are not in sync, and x will grow exponentially, meaning that the molecule will collide with the wall of the decelerator and be lost, see *Figure 2.19*.

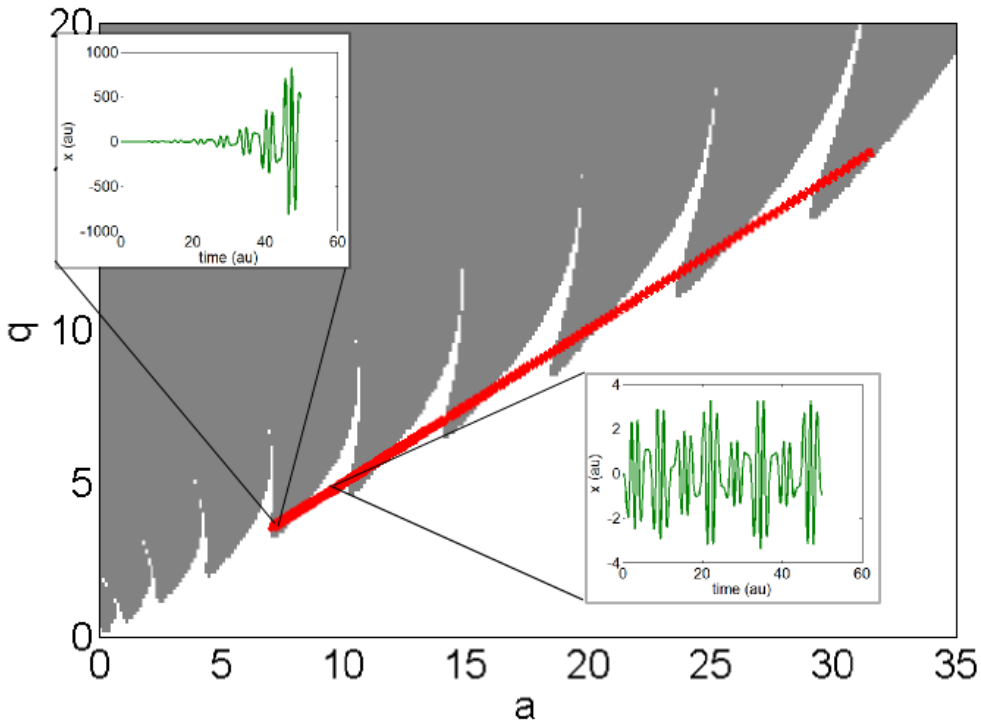

Figure 2.19 – The trajectories in the unstable region(grey) vs the stable region(white).

For clarity, we can trace along $z = \frac{L}{2} \ldots L$ in Figure 2.18, and plot stable/ unstable for each point of z, see *Figure 2.20*. We then trace the same trace over the longitudinal phase space plot, see Figure 2.21, and we should see similar pattern of unstable and stable regions along the $z = \frac{L}{2} \ldots L$ curve.

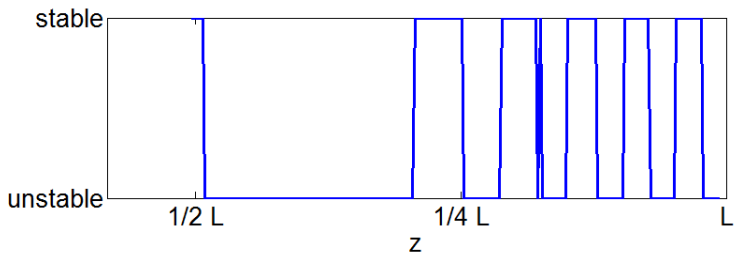

Figure 2.20 – unstable and stable regions along the $z = \frac{L}{2} \ldots L$ *curve*

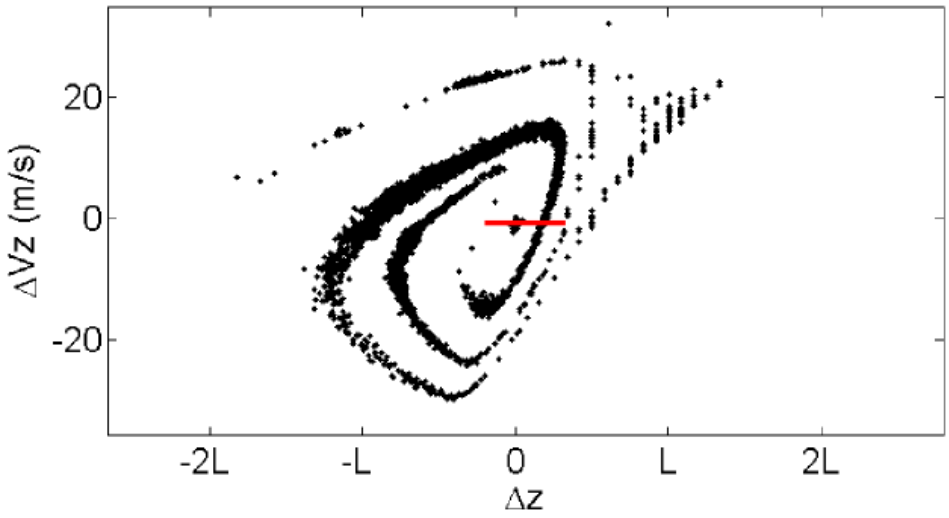

Figure 2.21 – simulation of final phase space of decelerated packet ($\phi_0 = 30^\circ$), showing the ring like structures. $\{z = 0, \Delta v_z = 0\}$ correspond to the coordinates of the synchronous molecule. And the red trace is for $z = \frac{L}{2}...L$, and L is the length of the decelerator.

Comparing the numerical simulation, Figure 2.21, with the stability diagram analysis, Figure 2.20, we see the general pattern of alternating unstable and stable region somewhat matches. The difference is, in Figure 2.21, numerical simulation predict only ~ 4 periods of unstable and stable region within $z = \frac{L}{2}...L$, but the stability diagram, Figure 2.20, predicts ~ 6 periods. The difference is probably coming from the assumptions and simplifications made by the stability diagram model which are not valid in our actual experimental setup.

2.3.4.1 Calculation of longitudinal oscillation frequency

Calculation of longitudinal oscillation frequency is slightly different from the calculation of transverse oscillation frequency. Because, the forces which causes the longitudinal oscillations are effective forces, and not real forces. From the longitudinal phase stability section, we know that the equation of motion in longitudinal direction is

$$\frac{d^2\Delta z}{dt^2} - \frac{1}{m}\frac{1}{L}[W(z_0 - \Delta z) - W(z_0)] = 0$$

Equation 2.34

And, if we model the longitudinal oscillation as a simple harmonic oscillation

$$\frac{d^2\Delta z}{dt^2} + \omega_z{}^2 \Delta z = 0$$

Equation 2.35

Then we can compare Equation 2.34 and Equation 2.35, to get the longitudinal oscillation frequency

$$-\frac{1}{mL}[W(z_0 - \Delta z) - W(z_0)] = \omega_z{}^2 \Delta z$$

$$\Rightarrow \omega_z = \sqrt{-\frac{1}{\Delta z}\frac{1}{mL}[W(z_0 - \Delta z) - W(z_0)]}$$

Equation 2.36

Roughly, for synchronous molecule with $\phi_0 = 45^\circ$, the longitudinal oscillation is around $\omega_z = 3e3 \sim 6e3 rad/s$ depending on the relative position to the synchronous molecule. It is interesting to note, the actual frequency, ie oscillations per second is $f_z = \frac{\omega_z}{2\pi} = 0.5kHz \sim 1kHz$. And in the experiment, typical flight time is $\sim 3ms$, hence total number of oscillations is $(0.5kHz \sim 1kHz) \times 3ms = 1.5 \sim 3$ oscillations. Three longitudinal oscillations over the whole length of the decelerator are rather little. With some different assumptions, we might have less than one oscillation over the length of decelerator. And in such situations, one needs to be careful about using the concept of longitudinal phase stability, because phase stability is only a meaningful concept when the evolution time is long enough.

2.4 Transition frequencies and transition intensities of CH_3

The detection scheme we are using is resonance enhanced multi photon ionization (REMPI). We are using, 2+1 REMPI, meaning that we use 2 photons to excite CH_3 from $\tilde{X}\,^2A_2''$ ground state into the $4p_z\,^2A_2''$ Rydberg state and 1 more photon to ionization continuum. Hence, understanding the REMPI spectra of CH_3 is essential. One of the main uses of understanding and simulating the REMPI spectra is, that we can obtain the rotational temperature of CH_3, which is difficult to obtain otherwise.

2.4.1 Transition frequencies of CH_3

The two photon transition between the ground vibronic state $\tilde{X}\,^2A_2''$ and the Rydberg state $4p_z\,^2A_2''$ is subjected to the selection rule of $\Delta K = 0$ [15], ie $K' = K''$. Hence the rotational transitions are of the nature $|N', K\rangle \leftarrow |N'', K\rangle$. The energy levels are from the rigid rotor model, with added higher order terms due to centrifugal distortion [48]. The energy levels, $E_{N'',K}$, for the ground state, $\tilde{X}\,^2A_2''$, are:

$$E_{N'',K} = B''N''(N''+1) + (C''-B'')K^2 - D''_N N''^2(N''+1)^2 - D''_{NK} N''(N''+1)K^2 - D''_K K^4$$

Equation 2.37

The rotational constants used in Equation 2.37 are defined in Table 2.2 below. And similarly, for $4p_z\,^2A_2''$ excited state, we have

$$E_{N',K} = B'N'(N'+1) + (C'-B')K^2 - D'_N N'^2(N'+1)^2 - D'_{NK} N'(N'+1)K^2 - D'_K K^4 .$$

Ground state(cm^{-1})			Excited state(cm^{-1})			Difference terms(cm^{-1})		
B''	D''_N	D''_{NK}	B'	D'_N	D'_{NK}	ν_0	ΔC	ΔD_K
9.57789	$7.699e-4$	$-1.358e-4$	9.90	$10.7e-4$	$-21.2e-4$	698523.44	$-8.8e-2$	0

Table 2.2 – constants used for calculation of transition frequency, experimentally determined by ref [48]

The transition frequency, ν, is then the difference between the two rotational manifolds, with band origin ν_0

$$\nu = \nu_0 + \Delta C K^2 - \Delta D_K K^4$$
$$+[B'N'(N'+1) - B'K^2 - D'_N N'^2(N'+1)^2 - D'_{NK} N'(N'+1)K^2]$$
$$-[B''N''(N''+1) - B''K^2 - D''_N N''^2(N''+1)^2 - D''_{NK} N''(N''+1)K^2]$$

Equation 2.38 - where all constants are defined in Table 2.2, and the transition frequency, ν, ie two photon energy, obtained using Equation 2.38 is in the range of $69700 \cdots 70100 cm^{-1}$.

2.4.2 Transition intensities of CH_3

For calculating transition intensity, we use ref [49]. The transition intensity, $I_{N',N'',K}$, of the transition $|N',K\rangle \leftarrow |N'',K\rangle$ is defined as [49]

$$I_{N',N'',k} = \frac{S_{N',N'',K}}{2N''+1} \frac{1}{D_{N',K}} P_{N'',K}$$

Equation 2.39 - where $P_{N'',K}$ is the relative population of each rotational level, $|N'',K\rangle$ of the ground state CH_3. $P_{N'',K}$ is a product of nuclear spin degeneracy and Boltzmann population. $S_{N',N'',K}$ is the relative intensity of two photon transition. And $D_{N',K}$ accounts for the loss in ionization efficiency due to predissociation of electronically excited CH_3 [49]

Next, we look at each term more closely. The simplest term is $D_{N',K}$, which we take as a given from ref [49], and it has the form

$$D_{N',K} = 1 + \frac{\Delta\nu_i}{\Delta\nu_h}[N'(N'+1) - K^2]$$

Where $\Delta\nu_h = 1.0 cm^{-1}$, and $\Delta\nu_i = 0.12 cm^{-1}$

Next, we look at the term $P_{N'',K}$, which is defined as

$$P_{N'',K} = Q^{-1} \times G \times (2N''+1) \exp\left[-\frac{E_{N'',K}}{k_B T}\right]$$

Where $Q = \sum_i G_i (2N''_i + 1) \exp\left[-\frac{E_i}{k_B T} \right]$ is the partition function, $E_{N'',k}$ is the energy levels of the ground vibronic state of CH_3, which is defined in Equation 2.37. And G is the degeneracy of each rotational level due to nuclear spin statistics.

If we assume the same rotational temperature for both para and ortho species of CH_3, then the spin statistics can be stated more concisely as $\text{for } |K| = 1, 2, 3, 4, 5, 6, \ldots N''$, the degeneracy have a repeating pattern $G = 2, 2, 4, 2, 2, 4, \ldots$. And $\text{for } K = 0$, $G = 4 \text{ for even } N$, and $G = 0 \text{ for odd } N$. For more details, see Section 2.5 about CH_3 Symmetry and Nuclear Spin Statistics.

And lastly, we have the two photon transition intensity $S_{N',N'',K}$, which explicit form was obtained from ref [50], where they developed rotational line strengths of two photon absorption process in symmetric top molecules using angular momentum theory. The explicit form of $S_{N',N'',K}$ is from ref [50]:

$$S_{N',N'',K} = 5(2N''+1)\frac{\mathbb{F}}{\mathbb{E}} + (2N''+1)(2(N''+\Delta N)+1)\begin{pmatrix} N''+\Delta N & N'' & 2 \\ K & -K & 0 \end{pmatrix}^2, \text{ for } \Delta N = 0, \text{ ie Q-branch}$$

Equation 2.40

$$S_{N',N'',K} = (2N''+1)(2(N''+\Delta N)+1)\begin{pmatrix} N''+\Delta N & N'' & 2 \\ K & -K & 0 \end{pmatrix}^2, \text{ for } \Delta N \neq 0$$

Equation 2.41

Where the explicit form of $\mathbb{E}$ is following, see *Equation 2.42*, (the explicit form of $\mathbb{F}$ is similar to $\mathbb{E}$, and is not included here)

$$\mathbb{E} = \left| \sum_i \frac{2\mu^0_{fi}\mu^0_{i0} + \mu^1_{fi}\mu^{-1}_{i0} + \mu^{-1}_{fi}\mu^1_{i0}}{E_{i0} - \omega} \right|^2$$

Equation 2.42 - where 0 labels the initial state, i labels the intermediate state, and f labels the final state, for definition of $\mu^{0,\pm1}$ see ref [50].

We can see that $\mathbb{E}$ and $\mathbb{F}$ are just dipole coupling strengths between different electronic states, 0, i and f, which is molecule and state dependent, and can be calculated using vibrational wavefunctions. We will avoid calculating $\mathbb{E}$ and $\mathbb{F}$, by making a simplification, by assuming $\mathbb{F}/\mathbb{E} = c$, where c is a constant. This assumption does not affect our analysis of rotational temperature, because $\mathbb{E}$ and $\mathbb{F}$ only contain vibronic labels, and not rotational labels, as we see in Equation 2.42. The result due to $\mathbb{F}/\mathbb{E} = c$ simplification is, that the relative transition intensity of Q-branch, Equation 2.40 , to other branches, Equation 2.41, is no longer meaningful, which is an inconvenience, but not the end of the world for us.

The 3j symbols in Equation 2.40 and Equation 2.41 gives arise to selection rules for CH_3, and in summary for $4p_z\,{}^2A_2'' \leftarrow \tilde{X}\,{}^2A_2''$ transitions, the selection rules are [15]

$$\Delta K = 0$$
$$\text{for } K = 0, \quad \Delta N = 0, \pm 2$$
$$\text{for } K \neq 0, \quad \Delta N = 0, \pm 1, \pm 2$$

Equation 2.43

As an additional note, we see in Equation 2.40 and Equation 2.41, the transition intensities are independent of M quantum numbers, due to absence of external fields, hence we cannot select particular M state by using specifically polarized photons. [50]

The linewidth of each transition, while not essential for the analysis of the rotational temperature, can also be calculated. The linewidth is the full width at half maximum, $\Delta\nu$, of a Lorentzian peak, which is given as [49]

$$\Delta\nu = \Delta\nu_h + \Delta\nu_i[N'(N'+1) - K^2]$$

Where $\Delta\nu_h = 1.0 cm^{-1}$, and $\Delta\nu_i = 0.12 cm^{-1}$

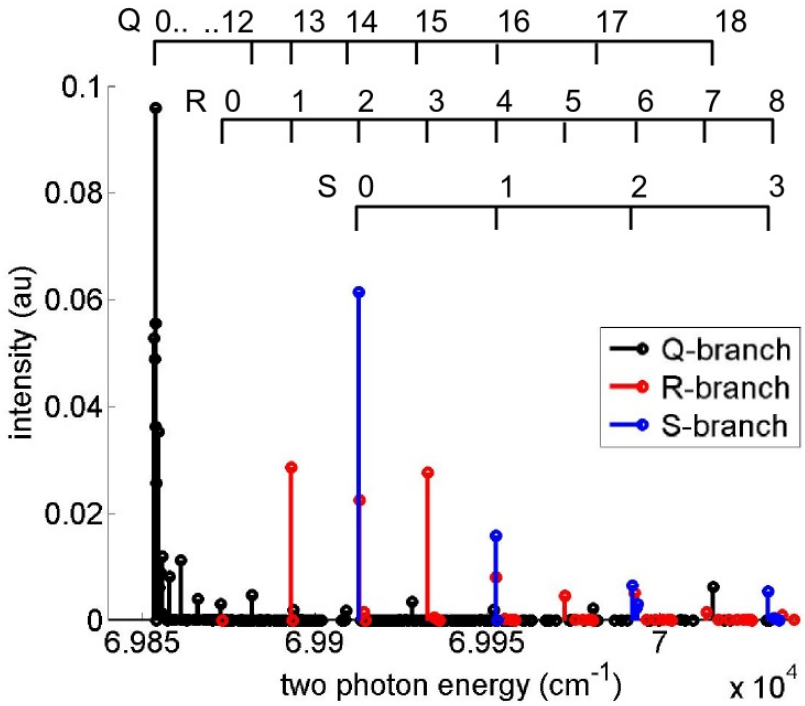

Figure 2.22 - The final simulated CH_3 spectra, and its assignment, at rotational temperature of $25K$. Reminding that the intensity of Q-branch relative to R and S branches is arbitrary.

In summary, combining the transition frequency, Equation 2.38, and the transition intensity, Equation 2.39, will result in the final result of simulation of CH_3 REMPI spectra, see Figure 2.22.

2.5 CH_3 Symmetry and Nuclear Spin Statistics

Pauli exclusion principle states that under exchange of identical particle within our system of particles, $\hat{P}_{12}$, the total wavefunction must be anti-symmetric, if two identical fermions are exchanged, ie

$$\hat{P}_{12}\Psi_{tot} = -\Psi_{tot}$$

Equation 2.44

And if two identical bosons are exchanged within the system, the total wavefunction of the system must be symmetric, ie $\hat{P}_{12}{}'\Psi_{tot} = \Psi_{tot}$. To clarify, our system of particles means all protons, electrons and neutrons that our CH_3 molecule is made of.

CH_3 molecule has a triangular planar structure, see Figure 2.23, and it belongs to the D_{3h} point group. The Pauli's exclusion principle, in terms of group theory, would state: when exchanging fermions, total wavefunction, Ψ_{tot}, must be of A_2' or A_2'' symmetry. And when exchanging bosons, total wavefunction, Ψ_{tot}, must be of A_1' or A_1'' symmetry.

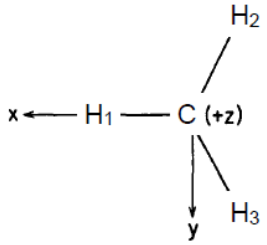

Figure 2.23 – CH_3 radical's planar structure, which belongs to the D_{3h} point group

In our case, we permute two hydrogen nuclei, ${}^1H$, which are fermions. Under this permutation, the symmetry of total wavefunction, Ψ_{tot}, must be of A_2' or A_2'' symmetry. Ie

$$\Gamma_{tot} = A_2' \text{ or } A_2''$$

Equation 2.45

The total wavefunction of a molecule is the product of its electronic wavefunction, vibrational wavefunction, rotational wavefunction, and nuclear wavefunction.

$$\Psi_{tot} = \psi_{elec}\psi_{vib}\psi_{rot}\psi_{nuc}$$

Equation 2.46

The symmetry of the total wave function, Γ_{tot}, is direct product of the symmetries of each term on right hand side of Equation 2.46 .

$$\Gamma_{tot} = \Gamma_{elec} \otimes \Gamma_{vib} \otimes \Gamma_{rot} \otimes \Gamma_{nuc}$$

Equation 2.47

And the direct product table for our point group D_{3h} is given in Table 2.3.

	A'1	**A'2**	**E'**	**A"1**	**A"2**	**E"**
A'1	A'1	A'2	E'	A"1	A"2	E"
A'2	A'2	A'1	E'	A"2	A"1	E"
E'	E'	E'	A'1+A'2+E'	E"	E"	A"1+A"2+E"
A"1	A"1	A"2	E"	A'1	A'2	E'
A"2	A"2	A"1	E"	A'2	A'1	E'
E"	E"	E"	A"1+A"2+E"	E'	E'	A'1+A'2+E'

Table 2.3 – Direct Product table for D_{3h} point group [51]

2.5.1 Symmetry of electronic wavefunction

The goal of this subsection is to get the symmetry of electronic wavefunction Γ_{elec} which is used in Equation 2.47. The symmetry of electronic wavefunction is the direct product of symmetries of all molecular orbitals.

$$\Gamma_{elec} = (\Gamma_1)^n \otimes (\Gamma_2)^{n'} \otimes \cdots \otimes (\Gamma_m)^{n'''\cdots}$$

Where Γ_1, Γ_2 etc... are the irreducible representation of the molecular orbitals, and n, n' etc... are the corresponding principal quantum numbers of the orbitals. Note that totally filled subshells are always totally symmetric, and can be excluded in the symmetry analysis. [52]

The derivation of the symmetry of molecular orbitals in general is bit complicated and somewhat similar to the methods used to obtain vibration and rotational symmetries, hence overview of the methodology of symmetry of molecular orbital is omitted here. The result is that the ground electronic configuration and its symmetry of CH_3 is

$$\underbrace{(1a_1')^2(2a_1')^2(2e')^4}_{\text{totally filled subshell}}(2a_2'')^1$$

Equation 2.48

In Equation 2.48, first three subshells are fully occupied, and can be excluded in the symmetry analysis. The only subshell contributing to the symmetry is $(2a_2'')^1$. Hence, the term for ground state is $\tilde{X}\,^2A_2''$, meaning that $\Gamma_{elec} = A_2''$, see ref [15].

2.5.2 Symmetry of vibrational wavefunction

The goal of this subsection is to get the symmetry of vibrational wavefunction Γ_{vib} which is used in Equation 2.47. The symmetry of vibrational wavefunction is the direct product of symmetries of all normal modes.

$$\Gamma_{vib} = \Gamma_{\nu_1}{}^{v} \otimes \Gamma_{\nu_2}{}^{v'} \otimes \cdots \otimes \Gamma_{\nu_{3N-6}}{}^{v''\cdots}$$

Equation 2.49 - where ν_1, ν_2 etc labels the vibrational mode, and v, v' etc labels the vibrational quantum number for the corresponding mode, and N is the number of atoms in the molecule.

Getting the symmetries for each vibrational mode, Γ_{ν_i}, is not trivial. In general, for a molecule with N atoms, the steps to get the symmetry of vibrational mode are following: First, we construct a reducible representation, Γ_{3N}, using the $3N$ Cartesian coordinates of the N atoms in our molecule. Then, reduce the representation into irreducible form of the corresponding point group, hence obtaining Γ_{3N} in the desired form. Next, we note that $3N$ Cartesian coordinates can be also decomposed as translational, rotational and vibrational coordinate, $\Gamma_{3N} = \Gamma_t \oplus \Gamma_r \oplus \Gamma_v$, and from character table, see Table 2.4, we know the symmetries of Γ_t

and Γ_r, and we can subtract these to get Γ_v. Ie $\Gamma_v = \Gamma_{3N} \ominus \Gamma_t \ominus \Gamma_r$. Where Γ_v contains all the vibrational modes, with total of $3N-6$ modes.

D_{3h}	$\hat{E}$	$2\hat{C}_3$	$3\hat{C}_2$	$\hat{\sigma}_h$	$2\hat{S}_3$	$3\hat{\sigma}_v$		
A_1'	1	1	1	1	1	1		$x^2+y^2; z^2$
A_2'	1	1	−1	1	1	−1	R_z	
E'	2	−1	0	2	−1	0	(x, y)	(x^2-y^2, xy)
A_1''	1	1	1	−1	−1	−1		
A_2''	1	1	−1	−1	−1	1	z	
E''	2	−1	0	−2	1	0	(R_x, R_y)	(xz, yz)

Table 2.4 – Character table for D_{3h} point group

So, up till this stage, we have only obtained the symmetries of all vibrational modes, Γ_v. And next step is to assign the symmetries of Γ_v to each mode and frequency, Γ_{ν_i}, only then we can obtain the symmetry of vibration wavefunction given which vibrational normal modes are occupied, by using Equation 2.49.

For example, for H_2O, belonging to C_{2v} point group, it has three vibrational modes with following symmetries, $\Gamma_{\nu_1} = A_1$, $\Gamma_{\nu_2} = A_1$, $\Gamma_{\nu_3} = A_2$. Let's say the vibrational level is $1^2\ 2^1\ 3^3$, meaning that $\text{for } \nu_1, v=2$, $\text{for } \nu_2, v=1$, $\text{for } \nu_3, v=3$. Then the symmetry of the vibrational wavefunction, Γ_{vib}, will be B_2 [53], see Equation 2.50

$$\Gamma_{vib} = \underbrace{A_1 \otimes A_1}_{1^2} \otimes \underbrace{A_1}_{2^1} \otimes \underbrace{B_2 \otimes B_2 \otimes B_2}_{3^3} = B_2$$

Equation 2.50

For our system, CH_3, we assume the molecule is vibrationally cold, and only 1^0, ie ν_1, $v=0$, symmetric mode is occupied. In this case, analysis simplifies, because we only have one term in Equation 2.49, and this term has the symmetry of A_1. Ie $\Gamma_{vib} = A_1$.

2.5.3 Symmetry of rotational wavefunction

The goal of this subsection is to get the symmetry of rotational wavefunction Γ_{rot} which is used in Equation 2.47. For a symmetric top molecule, the rotational eigenstates are labeled using the quantum numbers $|J,K,M\rangle$. The explicit form of the eigenstates can be derived to be

$$\psi_{rot}(\phi,\theta,\chi)=\langle\phi,\theta,\chi\,|\,J,K,M\rangle=\sqrt{\frac{2J+1}{8\pi^2}}D^J_{K,M}(\phi,\theta,\chi)$$

Equation 2.51 - where $D^J_{K,M}(\phi,\theta,\chi)$ is the Wigner rotation matrix, with rotational quantum number $J=0,1,2\ldots$; projection of J onto molecular axis can have values $K=-J\ldots-1,0,1\ldots+J$, and magnetic component of J can have values $M=-J\ldots-1,0,1\ldots+J$

The symmetry of ψ_{rot} is J and K dependent. To start, we pick a specific value for J and K, for example $|J=0,K=0,M\rangle$ And then we repeat the same process for all other values of J and K. To get the symmetry, we apply all "Equiv. rot." operations, the 3rd row shown in Table 2.5, to the explicit form of our function $|J=0,K=0,M\rangle$, which we obtain from Equation 2.51. The behavior of our function Equation 2.51 under these "Equiv. rot." operations is defined in Equation 2.52.

	E	(123)	(23)	E^*	$(123)^*$	$(23)^*$
$D_{3h}(M)$:	1	2	3	1	2	3
D_{3h}:	E	$2C_3$	$3C_2$	σ_h	$2S_3$	$3\sigma_v$
Equiv. rot.:	R^0	$R_z^{2\pi/3}$	R_0^π	R_z^π	$R_z^{-\pi/3}$	$R_{\pi/2}^\pi$
A_1':	1	1	1	1	1	1
A_1'':	1	1	1	−1	−1	−1
A_2':	1	1	−1	1	1	−1
A_2'':	1	1	−1	−1	−1	1
E':	2	−1	0	2	−1	0
E'':	2	−1	0	−2	1	0

Table 2.5 – Permutation inversion table for D_{3h} point group [54]

$$R_z^{\beta} \mid J,K,M\rangle = e^{iK\beta} \mid J,K,M\rangle$$
$$R_{\alpha}^{\pi} \mid J,K,M\rangle = (-1)^J e^{-2iK\alpha} \mid J,-K,M\rangle$$

Equation 2.52

After each application of rotation from Equation 2.52 to our rotation function Equation 2.51, we will get a term. For our function $\mid J=0,K=0,M\rangle$, we need to apply six equivalent rotations, and we will get six terms (numbers) in return, which for $\mid J=0,K=0,M\rangle$ is $\{1,1,1,1,1,1\}$. Then we use Table 2.5 to match the terms with the symmetry, which for $\mid J=0,K=0,M\rangle$ is A_1'. This means that the rotational state $\mid J=0,K=0,M\rangle$ has A_1' symmetry. For more details, see [52]

We need to note that Equation 2.52 is general behavior of Wigner rotation matrix, the part which is specific to our molecule is Table 2.5 , specifying that we are in the point group D_{3h}, and "Equiv. rot." In this point group is different from other point groups.

We need to repeat this same procedure for all rotational states. And in the end, we will find a pattern, which is summarized in Table 2.6.

	Γ_{rot}
$K=0, J$ even	A_1'
$K=0, J$ odd	A_2'
$K=6n\pm1$	E''
$K=6n\pm2$	E'
$K=6n\pm3$	$A_1'' \oplus A_2''$
$K=6n\pm6$	$A_1' \oplus A_2'$

Table 2.6 – symmetries of rotational wavefunction, $\mid J,K,M\rangle$, degeneracy of M is ignored, and n is an integer. [52]

Using Table 2.6, we can write out some low lying levels explicitly, for future references.

	Γ_{rot}
$\|J=0,K=0\rangle$	A_1'
$\|J=1,K=0\rangle$	A_2'
$\|J=1,K=\pm1\rangle$	E''
$\|J=2,K=0\rangle$	A_1'
$\|J=2,K=\pm1\rangle$	E'
$\|J=2,K=\pm2\rangle$	E''

Table 2.7 – symmetry of low lying rotational levels

2.5.4 Symmetry of nuclear spin wavefunction

The goal of this subsection is to get the symmetry of nuclear wavefunction Γ_{nuc} which is used in Equation 2.47.

The nuclear spin wavefunction is first constructed using Slater determinants, then its symmetry properties are examined. In our molecule, CH_3, there are three H nucleus, ie three ½ spin fermions. Hence, the total nuclear spin of the combined three spin system has to be $I=\frac{3}{2}$ or $I=\frac{1}{2}$. And Slater determinant need to be used to symmetrize the total nuclear spin wavefunction of the combined three spin system.

Skipping the derivation, the final spin wavefunction for $I=\frac{3}{2}$ is shown explicitly in Equation 2.53

$$|I=\tfrac{3}{2},M_I=\tfrac{3}{2}\rangle = |I=\tfrac{1}{2},M_I=\tfrac{1}{2}\rangle_1 \,|I=\tfrac{1}{2},M_I=\tfrac{1}{2}\rangle_2 \,|I=\tfrac{1}{2},M_I=\tfrac{1}{2}\rangle_3$$

*Equation 2.53 - w*here sub index labels the identical protons.

In addition to Equation 2.53, there are three other functions for $I=\frac{3}{2}$, namely $|I=\frac{3}{2},M_I=\frac{1}{2}\rangle$, $|I=\frac{3}{2},M_I=-\frac{1}{2}\rangle$ and $|I=\frac{3}{2},M_I=-\frac{3}{2}\rangle$, which explicit form is not written here.

And similarly, for $I=\frac{1}{2}$, the final result we get is following

$$|I=\tfrac{1}{2},M_I=\tfrac{1}{2}\rangle=\frac{1}{\sqrt{6}}\left[2\alpha_1\alpha_2\alpha_3-\alpha_1\beta_2\alpha_3-\alpha_1\alpha_2\beta_3\right]$$

Equation 2.54 - where $\alpha=|I=\tfrac{1}{2},M_I=\tfrac{1}{2}\rangle,\beta=|I=\tfrac{1}{2},M_I=-\tfrac{1}{2}\rangle$

$$|I=\tfrac{1}{2},M_I=\tfrac{1}{2}\rangle=\frac{1}{\sqrt{2}}\left[\alpha_1\beta_2\alpha_3-\alpha_1\alpha_2\beta_3\right]$$

Equation 2.55 - where $\alpha=|I=\tfrac{1}{2},M_I=\tfrac{1}{2}\rangle,\beta=|I=\tfrac{1}{2},M_I=-\tfrac{1}{2}\rangle$

In addition to Equation 2.54 and Equation 2.55, there are two other functions for $I=\tfrac{1}{2}$, both belonging to $|I=\tfrac{1}{2},M_I=-\tfrac{1}{2}\rangle$, which explicit form is not written here.

For three spins, each spin can have either $\uparrow$ or $\downarrow$, there exist total of $2^3=8$ different combinations, ie nuclear spin functions. And as we saw above, there are 4 nuclear spin functions coming from $I=\tfrac{3}{2}$, and 4 nuclear spin functions coming from $I=\tfrac{1}{2}$, totaling to 8 nuclear spin functions.

Now that we have explicit form of all the nuclear spin wavefunction, we can start examining their symmetry properties. To examining the symmetry properties, we use the character table, Table 2.5, and the permutation operations of Table 2.5, ie the first row in Table 2.5, to our nuclear spin wavefunctions, Equation 2.53 - Equation 2.55. For example, if we take Equation 2.53, and operate cyclic permutation, (123), on the wavefunction, we will see that

$$\hat{P}_{123}|I=\tfrac{3}{2},M_I=\tfrac{3}{2}\rangle=|I=\tfrac{3}{2},M_I=\tfrac{3}{2}\rangle$$

Equation 2.56 - where $\hat{P}_{123}\equiv(123)$.

And since the operation did not change the wavefunction in Equation 2.56, hence the term Equation 2.56 returns is 1. And we do the same calculation for all permutation operations on Equation 2.53, resulting in $\{1,1,1,1,1,1\}$, which corresponds to A_1 symmetry.

In principle, each permutation operation must be carried out once to each of the nuclear spin wavefunctions, in this case, we have 8 spin functions, and 6 different permutation operations

from Table 2.5, we would have to do $8 \times 6 = 48$ calculations to get the symmetries of all our nuclear spin wavefunctions. And in the end, the result is summarized in Table 2.8.

	Γ_{nuc}
$\lvert I = \frac{3}{2} \rangle$	A_1
$\lvert I = \frac{1}{2} \rangle$	E

Table 2.8 – summary of nuclear spin wavefunction

2.5.5 Nuclear spin statistics

Looking back at Equation 2.47, $\Gamma_{tot} = \Gamma_{elec} \otimes \Gamma_{vib} \otimes \Gamma_{rot} \otimes \Gamma_{nuc}$, we have obtained the terms $\Gamma_{elec}, \Gamma_{vib}, \Gamma_{rot}$ and Γ_{nuc}, and the knowledge that Γ_{tot} has to be A_2 or the state doesn't exist due to symmetry concerns.

At low temperatures, the analysis simplifies, because we assume the molecule is at ground electronic state, with $\Gamma_{elec} = A_2$, and ground vibrational state, with $\Gamma_{vib} = A_1$, and that Γ_{tot} has to be A_2. So Equation 2.47 simplifies to

$$A_2 = A_2 \otimes A_1 \otimes \Gamma_{rot} \otimes \Gamma_{nuc}$$
$$\Rightarrow \Gamma_{rot} \otimes \Gamma_{nuc} = A_1$$

Equation 2.57

Using Equation 2.57, we write out some levels explicitly for clarity, see Table 2.9 below.

	Γ_{rot}	Γ_{nuc}	$\Gamma_{rot} \otimes \Gamma_{nuc}$	
$\lvert J = 0, K = 0 \rangle \lvert I = \frac{3}{2} \rangle$	A_1	A_1	A_1	
$\lvert J = 1, K = 0 \rangle \lvert I = \frac{3}{2} \rangle$	A_2	A_1	A_2	*forbidden*
$\lvert J = 2, K = 0 \rangle \lvert I = \frac{3}{2} \rangle$	A_1	A_1	A_1	
$\lvert J = 1, K = \pm 1 \rangle \lvert I = \frac{1}{2} \rangle$	E	E	$A_1 \oplus A_2 \oplus E$	
$\lvert J = 1, K = \pm 1 \rangle \lvert I = \frac{3}{2} \rangle$	E	A_1	E	*forbidden*

Table 2.9 – symmetry allowed and forbidden states

Next step is to look at the degeneracy for each of the state, we shall go through some examples how the degeneracies are obtained. First example, from 1st row of Table 2.9, we have the state $|J=0,K=0\rangle|I=\frac{3}{2}\rangle$, we see it's symmetry allowed, and the degeneracy is 4, because $|J=0,K=0\rangle$ contains 1 function, and $|I=\frac{3}{2}\rangle$ contains 4 functions, see Equation 2.53, hence $1\times 4=4$. Second example, from 2nd row of Table 2.9, we have the state $|J=1,K=0\rangle|I=\frac{3}{2}\rangle$, we see it is symmetry forbidden, and hence degeneracy is labeled as 0. Third example, from 4th row of Table 2.9, we have the state $|J=1,K=\pm 1\rangle|I=\frac{1}{2}\rangle$, we see it is symmetry allowed, and the degeneracy is 2, because $|J=1,K=\pm 1\rangle$ contains 2 functions, due to two fold degeneracy of K, and $|I=\frac{1}{2}\rangle$ contains 4 functions, hence $2\times 4=8$ functions. However, we note that in the direct product, $E\otimes E=A_1\oplus A_2\oplus E$, have a contribution from A_1, which is the only allowed symmetry, is only ¼th of the total sum, hence the actual degeneracy of this level is $8\times\frac{1}{4}=2$. Figure 2.24 is another way to summarize the analysis in this section. Figure 2.24 displays all the allowed levels for CH_3, and the degeneracy of each level. We note that for $K=0$, only even J states exist, and only for $|I=\frac{3}{2}\rangle$. And, for $K=1,2,3,4,5,6\ldots$, the total nuclear spin varies in a repeated pattern of $I=\frac{1}{2},\frac{1}{2},\frac{3}{2},\frac{1}{2},\frac{1}{2},\frac{3}{2}\ldots$ this result is also used in ref [49] to calculate transition intensities of CH_3.

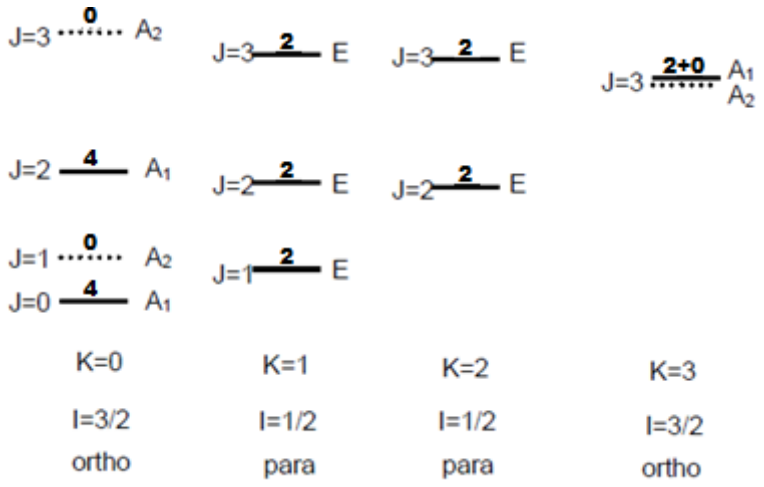

Figure 2.24 – allowed rotational levels, and nuclear spin statics and symmetries of CH_3, the bolded numbers on top of each energy level indicates the degeneracy of the level due to nuclear spin, 0 indicates that the level is missing.

At low temperature, in addition to electronic and vibration being on the ground state, only low rotational levels are occupied, hence CH_3 molecule is mainly in either of the two following states: $|J=1,K=\pm 1,I=\frac{1}{2}\rangle$, which we call the para state, or in $|J=0,K=0,I=\frac{3}{2}\rangle$, which we call the ortho state.

2.6 Zeeman shift of CH_3

The effective Hamiltonian used for the analysis of CH_3 Zeeman shift is following [55]

$$\hat{H}_{eff} = \hat{H}_{rot} + \hat{H}_{sr} + \hat{H}_{hf} + \hat{H}_{zeeman}(B_z)$$

Equation 2.58

From ref [55], we see that $\hat{H}_{hf} \propto a_f$, and $\hat{H}_{sr} \propto \epsilon_{bb}$, where a_f and ϵ_{bb} are molecular constants, and are given in Table 2.10. We see that value of a_f and ϵ_{bb} are small, compared to other terms in the effective Hamiltonian, B, C and $g_e \mu_B B_z$, with value of $g_e \mu_B B_z = 1.07\text{cm}^{-1} / Tesla \times B_z$. Hence, $\hat{H}_{sr}$ and $\hat{H}_{hf}$ can be neglected, ie $\hat{H}_{sr} \approx 0$ and $\hat{H}_{hf} \approx 0$.

(cm^{-1})	$CH_3\ X^2A_2"$
B	9.57789
C	4.74275
D_N	$0.770e-3$
D_{NK}	$-1.358e-3$
D_K	$0.634e-3$
a_f	0.0022
ϵ_{bb}	0.0117

Table 2.10 – molecular constants for ground state of CH_3, [55]

By setting $\hat{H}_{sr} \approx 0$ and $\hat{H}_{hf} \approx 0$, our effective Hamiltonian becomes

$$\hat{H}_{eff} = \hat{H}_{rot} + \hat{H}_{zeeman}(B_z)$$

Equation 2.59

According to ref [56], because spin rotation interaction is small, Hund's case (b) basis set should be used for ground state of CH_3, which we will denote to be $|N, K, S, J, I, F, M_F\rangle$ [57]. The matrix elements of the Hamiltonian in Equation 2.59 are given below.

The Hamiltonian $\hat{H}_{rot}$ is the symmetric top rotational Hamiltonian, which has matrix elements shown in Equation 2.60. We can discard the centrifugal distortion terms, because the values of D_N, D_{NK}, D_K are small, see Table 2.10.

$$\begin{aligned}\langle N,K,S,J,I,F,M_F \mid \hat{H}_{rot} \mid N,K,S,J,I,F,M_F \rangle &= BN(N+1)+(C-B)K^2 - D_N N^2(N+1)^2 \\ &\quad - D_{NK}N(N+1)K^2 - D_K K^4 \\ &\approx BN(N+1)+(C-B)K^2\end{aligned}$$

Equation 2.60

The Hamiltonian $\hat{H}_{zeeman}$ is the Zeeman Hamiltonian, the matrix elements for Zeeman Hamiltonian was taken from equation 34 of ref [57]. We have only taken the first term of the equation 34 of ref [57], which is the interaction between electron spin and the external B-field, see Equation 2.61. And we have discarded the other two terms from the equation 34 of ref [57], which are related to spin rotation interaction and interaction between nuclear spin and the external B-field.

$$\begin{aligned}\langle N,K,S,J',I,F',M_F \mid \hat{H}_{zeeman} \mid N,K,S,J,I,F,M_F \rangle = \\ \mu_B B_z (-1)^{F'-M_F} \begin{pmatrix} F' & 1 & F \\ -M_F & 0 & M_F \end{pmatrix} (-1)^{J'+I+F+1} \sqrt{(2F'+1)(2F+1)} \begin{Bmatrix} J' & F' & I \\ F & J & 1 \end{Bmatrix} \\ \times g_e (-1)^{N+S+J'+1} \sqrt{(2J'+1)(2J+1)} \begin{Bmatrix} S & J' & N \\ J & S & 1 \end{Bmatrix} \sqrt{S(S+1)(2S+1)}\end{aligned}$$

Equation 2.61 - where μ_B is the bohr magneton, B_z is the external B-field, g_e is the g factor of the electon, $(:::)$ is the 3j-symbol, $\{:::\}$ is the 6j-symbol

For $^2\Sigma$ term symbol, $S = 1/2$.

The lowest states are $|N=0,K=0\rangle$ and $|N=1,K=1\rangle$, which have $I = 3/2$ and $I = 1/2$ respectively. Then in the Hund's case (b), $J = N+S = N-1/2, N+1/2$, and $F = J+I$, with $|M_F| \le F$. For the lowest states $|N=0,K=0\rangle$ and $|N=1,K=1\rangle$, there are total of 20 basis functions in $|N,K,S,J,I,F,M_F\rangle$.

To get the values of B_z, we take the typical values of the B-field in our experiment, which is $0T...5T$.

The final result of Zeeman shift of CH_3 can be seen in Figure 2.25, which is obtained by adding Equation 2.60 and Equation 2.61, and diagonalizing the total Hamiltonian, and repeating the process at each value of B_z, in the range of $0T...5T$.

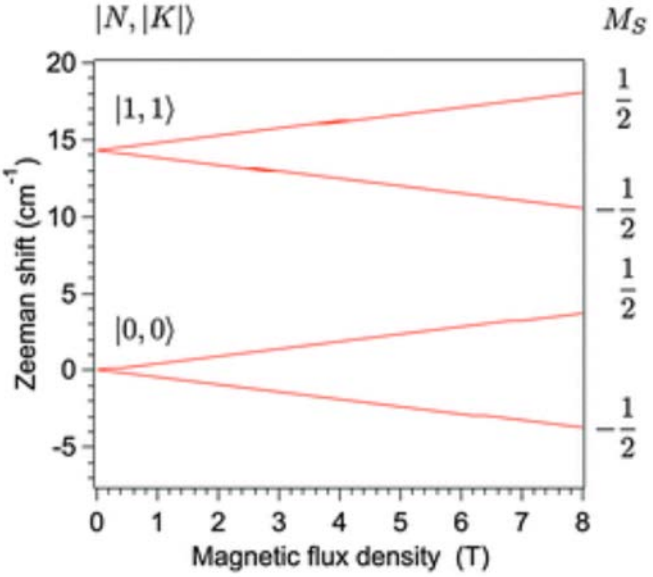

Figure 2.25 – the Zeeman shift of CH_3, for the $|N=0,K=0\rangle$ and $|N=1,|K|=1\rangle$ states. With our approximate Hamiltonian, the Zeeman shift of both levels are identical, and with the slope of $0.47cm^{-1}/Tesla$

In Figure 2.25, instead of labeling the states using $|N,K,S,J,I,F,M_F\rangle$, we have used $|N,K,S,M_S\rangle$ to label to states (for some reason).

The electron spin is decoupled from the molecular axis, and the electron spin is preferentially oriented relative to the external field. Then, each rotational state is split into two states that

can be characterized by the projection of the electron spin angular momentum along the space-fixed-axis, $M_S = \pm 1/2$.

It is important to note that the Zeeman shift is solely determined by the magnetic property of the electron for molecules in the doublet state in the high field limit. The shift does not depend on the rotational quantum numbers because of the decoupling of the rotational angular momentum N from the spin angular momentum S at high magnetic fields. Therefore, all rotational states split into two: one is the high field seeking state, and the other is the low field seeking state.

In summary, method of calculating Zeeman shift for ground state $X^2A_2"$ of CH_3 was described.

2.7 Transition frequencies and transition intensities of O_2

2.7.1 Transition frequencies of O_2

First is to understand the structure of the rotational levels in the ground and excited state of O_2 . The ground state is described naturally using Hund's case (b) basis set [58], and we shall label the level using Hund's case (b). To get N'', we first note that only odd N'' exists, due to nuclear spin statistics, which is not discussed in the text. Secondly, from supersonic expansion, we know that only low N'' levels are populated, in our case only the lowest two rotational levels were populated, ie $N''=1,3$. To get J'', we examine the term symbol $X^3\Sigma_g^-(v''=0)$, and deduce $\Lambda''=0$, $S''=1$, and the total angular momentum is $J''=\Lambda''+N''+S''=N''+1, N'', N''-1$ (Hund's case (b)). We have now obtained values for N'' and J'', see Equation 2.73, and hence we can label the levels of the ground state, see Figure 2.26.

The excited state is described naturally using Hund's case (a) basis set [58], and we shall label the level using Hund's case (a). To get Ω', we examine the term symbol $C^3\Pi_g(v'=2)$, and deduce $\Lambda'=1$, $S'=1$, and hence $\Sigma'=-1,0,1$, the total angular momentum projection is $\Omega'=\Lambda'+\Sigma'=0,1,2$ (Hund's case (a)). It must be noted that the addition of two projections is different than the addition of two angular momenta. To get J', we have the definition of $J'=\Omega'+N'$, where $\Omega'=0,1,2$ and $N'=0,1,2,3....$, where N' is the rotational quantum number of the excited state, and for the frequency range we are using, $N'=0...6$ is sufficient [59]. So, for each Ω', there are many values of N', and hence $\Omega'=0,1,2$ are named to be F_1, F_2 and F_3 branches. We have now obtained values for Ω' and J', see Equation 2.73, and hence we can label the levels of the excited state, see Figure 2.26.

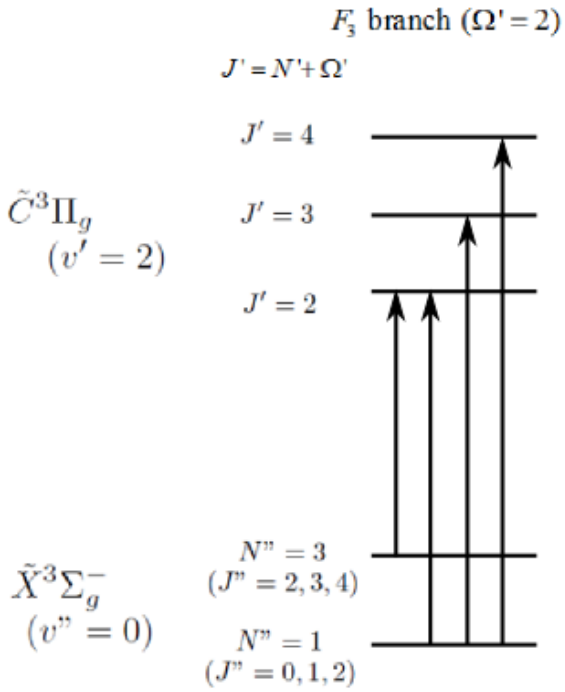

Figure 2.26 – Energy level diagram, of the ground rotational states, and one branch (out of three branches) of the excited rotational states.Plotted for example.The selection rules can be deduced from the 3j symbols of Equation 2.72

The actual values of the energy levels, can be obtained from ref [59]. Ref [59] calculated the rotational energy levels of $X^3\Sigma_g^-(v''=0)$ and $C^3\Pi_g(v'=2)$ states, using ref [60], and the results of ref [59] are quoted in Table 2.11 and Table 2.12 . And the transition frequency is just the difference of the energy levels between ground and excited state.

(cm^{-1})	$J''=N''+1$	$J''=N''$	$J''=N''-1$
$N''=1$	2.083	3.959	0.0
$N''=3$	16.387	18.336	16.253

Table 2.11 – The rotational energy levels (in cm^{-1}) of the ground $X^3\Sigma_g^-(v''=0)$ level of O_2

(cm^{-1})	$\Omega'=0$ (F_1)	$\Omega'=1$ (F_2)	$\Omega'=2$ (F_3)
band origin	69384.2	69468.6	69574.9

(cm^{-1})	$\Omega' = 0\ (F_1)$	$\Omega' = 1\ (F_2)$	$\Omega' = 2\ (F_3)$
$J' = 0$	1.642	*NaN*	*NaN*
$J' = 1$	4.823	5.028	*NaN*
$J' = 2$	11.186	11.582	5.145
$J' = 3$	20.731	21.412	15.324
$J' = 4$	33.458	34.520	28.894
$J' = 5$	49.370	50.905	45.854
$J' = 6$	68.467	70.569	66.201

Table 2.12 - The rotational energy levels and the band origins (in cm^{-1}*) of the excited* $C^3\Pi_g(v' = 2)$ *level of* O_2*.*

2.7.2 Transition intensities of O_2

The general theoretical expression of two photon absorption cross section, in the electric dipole approximation [50], is

$$I_{f0} = \left| \sum_i \frac{\langle f | \vec{\epsilon_1} \cdot \vec{r} | i \rangle \langle i | \vec{\epsilon_2} \cdot \vec{r} | 0 \rangle}{E_{i0} - \omega_1} + \frac{\langle f | \vec{\epsilon_2} \cdot \vec{r} | i \rangle \langle i | \vec{\epsilon_1} \cdot \vec{r} | 0 \rangle}{E_{i0} - \omega_2} \right|^2$$

Equation 2.62 - Where $|0\rangle$ is the initial state, $|f\rangle$ is the final state, and $|i\rangle$ is the intermediate state.

We assume each state wavefunction can be decomposed into product functions, of electronic, vibrational, and rotational wavefunctions. We also assume using two identical photons $\omega_1 = \omega_2 = \omega$, with linear polarization. We also assume E_{i0} is insensitive to rotational states of the excited level. Then Equation 2.62 can be transformed [50] into

$$I_{f0} = 4 \sum_{MM"} \left| \underbrace{\sum_{q'q"} \langle J"K"M" | D^{(1)*}_{0q'} D^{(1)*}_{0q"} | JKM \rangle}_{\text{rotational part}} \times \underbrace{\sum_{\text{in'}} (\mathrm{E_{i0}}\text{-}\omega)^{-1} \mu_{\mathrm{fi}}^{q'} \mu_{\mathrm{i0}}^{q"}}_{\text{vibronic part}} \right|^2$$

Equation 2.63 - The summation over $M, M"$ is necessary in the absence of external field.

$D^{(Q)}_{0,-q'-q"}$ is Wigner's D-matrix

From Equation 2.63, we discard the vibronic part, setting it to a constant, and we get Equation 2.64. By discarding the vibronic part, we simplify the calculation, but we also lose the information on vibronic transitions. The spectra we take are rotational spectra, hence we don't mind losing the information of the vibronic transitions.

$$I_{f0} \propto \sum_{MM"} \left| \sum_{q'q"} \langle J"K"M" | D^{(1)*}_{0q'} D^{(1)*}_{0q"} | JKM \rangle \right|^2$$

Equation 2.64

From Equation 2.64, using Equation 2.65 [50] [61], we contract two rotational matrix to get

Equation 2.66

$$D^{(1)*}_{0q'} D^{(1)*}_{0q"} = \sum_{Q} (2Q+1) \begin{pmatrix} 1 & 1 & Q \\ 0 & 0 & 0 \end{pmatrix} \begin{pmatrix} 1 & 1 & Q \\ -q' & -q" & q'+q" \end{pmatrix} D^{(Q)}_{0,-q'-q"}$$

Equation 2.65 – contraction of two rotational matrices

$$I_{f0} \propto \sum_{MM"} \left| \sum_{q'q"} \sum_{Q} (2Q+1) \begin{pmatrix} 1 & 1 & Q \\ 0 & 0 & 0 \end{pmatrix} \begin{pmatrix} 1 & 1 & Q \\ -q' & -q" & q'+q" \end{pmatrix} \langle J"K"M" | D^{(Q)}_{0,-q'-q"} | JKM \rangle \right|^2$$

Equation 2.66

In general, if the ground and the excited state use different Hund's basis, instead of the basis $|JKM\rangle$. If the ground state uses Hund's case (b), and the excited state uses Hund's case (a) (which happens to be the case for O_2), Then Equation 2.66 transforms into Equation 2.67 (we also swapped the bra and ket in Equation 2.67).

$$I_{f0} \propto \sum_{MM"} \left| \sum_{q'q"} \sum_{Q} (2Q+1) \begin{pmatrix} 1 & 1 & Q \\ 0 & 0 & 0 \end{pmatrix} \begin{pmatrix} 1 & 1 & Q \\ -q' & -q" & q'+q" \end{pmatrix} \underbrace{\langle \eta', \Lambda'; S', \Sigma'; J', \Omega' |}_{\text{excited state}} D^{(Q)}_{0,-q'-q"} \underbrace{| \eta", \Lambda"; N", S", J" \rangle}_{\text{ground state}} \right|^2$$

Equation 2.67

The matrix elements cannot be evaluated under different basis sets, hence transformation of basis is needed. The basis set we chose to work in is Hund's case (a) basis set. Using Equation 2.68, we transform Equation 2.67 into Equation 2.69.

$$\underbrace{|\eta, \Lambda; N, S, J\rangle}_{\text{Hund's case (b)}} = \sum_{\Sigma=-S}^{S} (-1)^{J-S+\Lambda} (2N+1)^{1/2} \begin{pmatrix} J & S & N \\ \Omega & -\Sigma & -\Lambda \end{pmatrix} \underbrace{|\eta, \Lambda; S, \Sigma; J, \Omega\rangle}_{\text{Hund's case (a)}}$$

Equation 2.68 – transformation from Hund's case (b) to Hund's case (a), see page 230 of ref [58]

$$I_{f0} \propto \sum_{MM"} \left| \sum_{q'q"} \sum_{Q} \sum_{\Sigma=-S}^{S} (-1)^{J-S+\Lambda} (2N+1)^{1/2} \begin{pmatrix} J" & S" & N" \\ \Omega" & -\Sigma" & -\Lambda" \end{pmatrix} \right.$$

$$\left. \times (2Q+1) \begin{pmatrix} 1 & 1 & Q \\ 0 & 0 & 0 \end{pmatrix} \begin{pmatrix} 1 & 1 & Q \\ -q' & -q" & q'+q" \end{pmatrix} \langle \eta', \Lambda'; S', \Sigma'; J', \Omega' | D^{(Q)}_{0,-q'-q"} | \eta", \Lambda"; S", \Sigma"; J", \Omega" \rangle \right|^2$$

Equation 2.69

In Equation 2.69, I_{f0} is the transition intensity from initial state $|0\rangle$ to the final state $|f\rangle$. $Q,\ q'\text{and}\ q''$ are summation indices. $D^{(Q)}_{0,-q'-q''}$ is Wigner's D-matrix. Single prime denotes the excited state, double prime denotes the ground state. The basis set used is Hund's case (a), see Figure 2.27: L and Λ are the electron orbital angular momentum and its projection onto molecular axis; S and Σ are the electron spin angular momentum and its projection onto molecular axis; N is the rotational angular momentum; J and M are the total angular momentum and its projection onto space fixed axis; Ω is defined as the sum of $\Omega = \Lambda + \Sigma$; η denotes all other quantum numbers which are not expressed explicitly, for example vibronic quantum numbers.

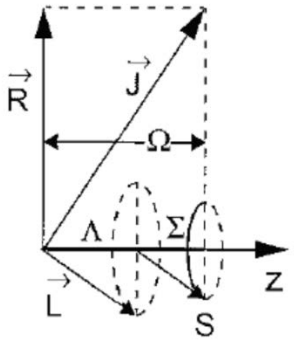

Figure 2.27 - Vector coupling diagram for Hund's case (a). R in the figure corresponds to N in the text.

Next, we expand Equation 2.69 into Equation 2.72, which is more explicit, using Equation 2.70 and Equation 2.71, and also dropping all constant.

$$|\eta,\Lambda;S,\Sigma;J,\Omega\rangle \equiv |\,J\Omega M\rangle = \sqrt{\frac{2J+1}{8\pi^2}}D^{J*}_{M,\Omega} = (-1)^{M-\Omega}\sqrt{\frac{2J+1}{8\pi^2}}D^{J}_{-M,-\Omega}$$

Equation 2.70 - Explicit form of rotational wavefunction, p105 of ref [61]

$$\int D^{J_3}_{M_3'M_3} D^{J_2}_{M_2'M_2} D^{J_1}_{M_1'M_1}\, d\Omega = 8\pi^2 \begin{pmatrix} J_1 & J_2 & J_3 \\ M_1' & M_2' & M_3' \end{pmatrix}\begin{pmatrix} J_1 & J_2 & J_3 \\ M_1 & M_2 & M_3 \end{pmatrix}$$

Equation 2.71 - Integral over product of three Wigner rotation matrices. p103 of ref [61]

$$I_{f0} \propto \sum_{MM''} \Big| \sum_{q'q''} \sum_{Q} \sum_{\Sigma=-S}^{S} (-1)^{J-S+\Lambda} (2N+1)^{1/2} \begin{pmatrix} J'' & S'' & N'' \\ \Omega'' & -\Sigma'' & -\Lambda'' \end{pmatrix} (2Q+1) \begin{pmatrix} 1 & 1 & Q \\ 0 & 0 & 0 \end{pmatrix} \begin{pmatrix} 1 & 1 & Q \\ -q' & -q'' & q'+q'' \end{pmatrix}$$
$$\times (-1)^{\Omega'-M'} (2J''+1)^{1/2} (2J'+1)^{1/2} \begin{pmatrix} J' & Q & J'' \\ M' & 0 & -M'' \end{pmatrix} \begin{pmatrix} J' & Q & J'' \\ \Omega' & -q'-q'' & -\Omega'' \end{pmatrix} \Big|^2$$

Equation 2.72– Important, general case of two photon rotational REMPI transition (subjected to the assumptions we mentioned above)

So far, the equation in Equation 2.72 is a general case of two photon rotational REMPI transition (subjected to the assumptions we mentioned above), for any system with excited state being Hund's case (a) and ground state being Hund's case (b).

For our specific case, we are using the transition $C^3\Pi_g(v'=2) \leftarrow X^3\Sigma_g^-(v''=0)$ of O_2.

Examining the term symbol of the ground state, we deduce $\Lambda''=0$, $S''=1$. After substitution of $\Lambda''=0$, $S''=1$. By examining the 1st 3j-symbol in Equation 2.72 (together with the selection rule of 3j-symbol), we also deduce $\Omega''=\Sigma''$. By examining the 2nd 3j-symbol, we deduce $Q=0,2$. By examining the 3rd 3j-symbol, we deduce $|q'|\leq 1$ and $|q''|\leq 1$. By examining the 3rd 3j-symbol, we deduce $|M'|\leq J'$ and $|M''|\leq J''$. And hence, we have obtained all the summation limits in order to calculate I_{f0}.

If we examine Equation 2.72 closely, we see the transition intensity is actually a function of four quantum numbers only, see Equation 2.73, two of which describes the ground state, and two of which describes the excited state, which is exactly what we want. Rest of the variables are either known, or are collapsed in the sums.

$$I_{f0} \rightarrow I_{f0}(\underbrace{\Omega', J'}_{\text{excited state}}; \underbrace{N'', J''}_{\text{ground state}})$$

Equation 2.73

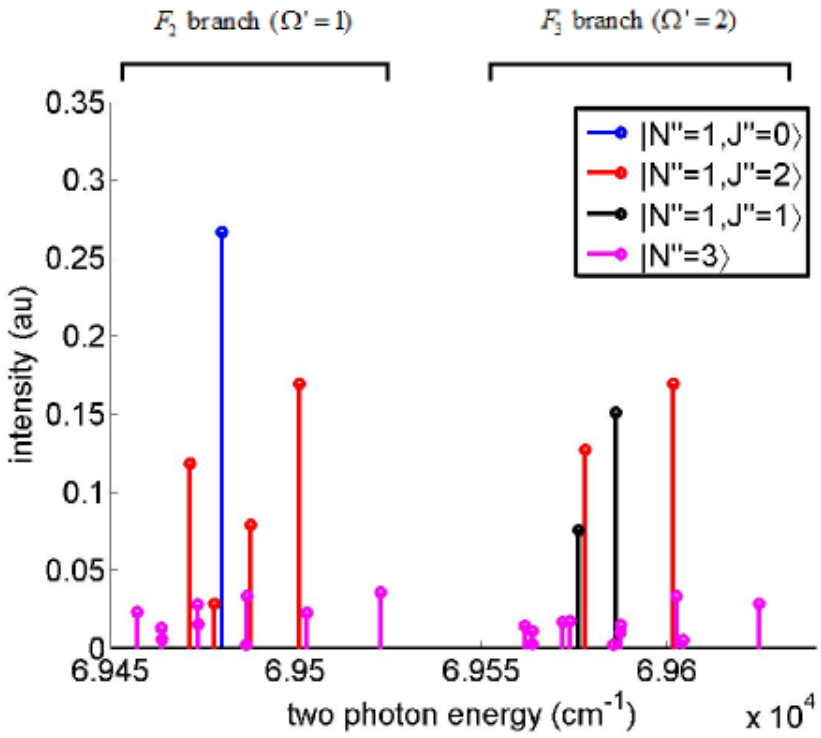

Figure 2.28 – The final simulated O_2 spectra, and its assignment, at rotational temperature of $10K$. Each peak can be broadened approximately, by a Lorentzian, to make comparison with experiment easier. The broadening is not essential for the analysis of the rotational temperature, which is the main purpose of the simulation of REMPI spectra.

In summary, Equation 2.72 describes the two photon REMPI transition intensity of O_2.

And combining Equation 2.72 with the transition intensity, Table 2.11 and Table 2.12, will result in the final result of simulation of O_2 REMPI spectra, see Figure 2.28.

2.8 Zeeman shift of O2

The rotational structure of O_2 and its Zeeman splitting of the vibronic ground state, $X^3\Sigma_g^-(v''=0)$, is described by an effective Hamiltonian, $\hat{H}_{eff}$ [58], [44]:

$$\begin{aligned}\hat{H}_{eff} &= \hat{H}_{rot} + \hat{H}_{ss} + \hat{H}_{sr} + \hat{H}_{zeeman}(B_z) \\ &= B\boldsymbol{N}^2 - D\boldsymbol{N}^4 + \frac{2}{3}\lambda(3S_z^2 - \boldsymbol{S}^2) + \gamma \boldsymbol{N}\cdot\boldsymbol{S} - g_e\mu_B \boldsymbol{S}\cdot\boldsymbol{B}\end{aligned}$$

Equation 2.74 - The effective Hamiltonian is the sum of rotational Hamiltonian $\hat{H}_{rot}$, spin-spin Hamiltonian $\hat{H}_{ss}$, spin-rotation Hamiltonian $\hat{H}_{sr}$, and the Zeeman Hamiltonian $\hat{H}_{zeeman}$.

The explicit form of the matrix elements of $\hat{H}_{rot}, \hat{H}_{ss}, \hat{H}_{sr}$ are given in section 10.4 of ref [58], see Equation 2.75, Equation 2.76 and Equation 2.77. Section 10.4 of ref [58] describes the field-free rotational spectra of $^3\Sigma$ state, using Hund's case (b) basis set. Central concepts used in these derivations are: theory of angular momentum, spherical tensors. [61]

$$\langle \eta, N, S, J, M_J \mid \hat{H}_{rot} \mid \eta, N, S, J, M_J \rangle = BN(N+1) - DN^2(N+1)^2$$

Equation 2.75 - where B is the rotational constant, and nothing to do with B-field.

$$\langle \eta, N, S, J, M_J \mid \hat{H}_{ss} \mid \eta, N', S, J, M_J \rangle = \lambda \frac{2\sqrt{30}}{3}(-1)^{J+N+S} \begin{Bmatrix} S & N' & J \\ N & S & 2 \end{Bmatrix}$$

$$\times(-1)^{N'} \begin{pmatrix} N & 2 & N' \\ 0 & 0 & 0 \end{pmatrix} \sqrt{(2N+1)(2N'+1)}$$

Equation 2.76 - where $N' = N-2, N, N+2$

$$\langle \eta, N, S, J, M_J \mid \hat{H}_{sr} \mid \eta, N, S, J, M_J \rangle = \gamma(-1)^{N+J+S} \begin{Bmatrix} S & N & J \\ N & S & 1 \end{Bmatrix} \sqrt{N(N+1)(2N+1)S(S+1)(2S+1)}$$

Equation 2.77

We see from Table 2.13 that γ is small compared to the terms B, λ and $g_e \mu_B B_z$, and hence spin rotation interaction $\hat{H}_{sr}$ is quite negligible, and can be ignored.

$g_e \mu_B B_z = 1.07 \mathrm{cm}^{-1} / Tesla \times B_z$.

(cm^{-1})	$^{16}O^{16}O(v=0)$
B	1.4222932
D	0.0000048
λ	1.9635485
γ	-0.0083354

Table 2.13 – Molecular parameters of O_2, in wavenumbers, used in Equation 2.75 … Equation 2.78, from p. 758 of ref [58]

The full description of $\hat{H}_{zeeman}$ are given in section 9.6 of ref [58], eq 9.177. The more boiled down version of the description is found in section 2.1.2 and appendix B of ref [44]. The explicit form of the matrix element of $\hat{H}_{zeeman}$ can be seen in Equation 2.78.

$$\langle \eta, N, S, J, M_J \mid \hat{H}_{zeeman} \mid \eta, N, S, J', M_J' \rangle = -g_e \mu_B B_z (-1)^{J - M_J + J' + N + 1 + S} \begin{pmatrix} J & 1 & J' \\ -M_J & 0 & M_J' \end{pmatrix}$$
$$\times \begin{Bmatrix} S & J' & N \\ J & S & 1 \end{Bmatrix} \sqrt{(2J+1)(2J'+1)S(S+1)(2S+1)}$$

Equation 2.78

g_e is the g-factor of electron, μ_B is the bohr magneton, B_z is the external B-field strength. From selection rule of 3j symbol, we have $J' = J-1, J, J+1$, and $M_J = M_J'$,

In Equation 2.75 … Equation 2.78, $S = 1$, since we are dealing with $^3\Sigma$ state. Molecular constants B, D, λ, γ are given in Table 2.13. The remaining undefined variables are N, J, M_J and B_z. The states will be labeled $\mid N, J, M_J \rangle$, and the Zeeman shift of each state will be a function of B_z, see Figure 2.29.

To get the values of N, J, M_J, we take the states with lowest energy, which are $|N=1, J, M_J\rangle$ and $|N=3, J, M_J\rangle$, where $J = N-1, N, N+1$, and $|M_J| \leq J$. This results in total of 30 basis functions in $|N, J, M_J\rangle$. The amount of basis functions we need is somewhat arbitrary, the stronger the coupling between different states, the more basis functions we need to include, and vice versa.

To get the values of B_z, we take the typical values of the B-field in our experiment, which is $0T \ldots 5T$.

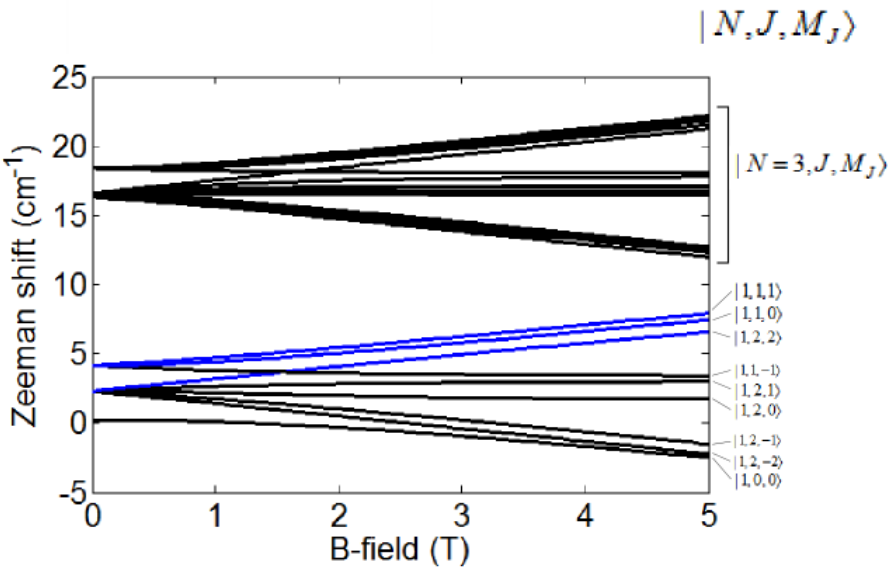

Figure 2.29 – the Zeeman shift of O_2, states are labeled $|N, J, M_J\rangle$, blue lines indicates LFS states of $|N=1, J=0,2,1, M_J\rangle$. $|N=3, J, M_J\rangle$ states are not labeled explicitly, because usually $|N=3, J, M_J\rangle$ states are not populated.

The final result of Zeeman shift of O_2 can be seen in Figure 2.29, which is obtained by adding Equation 2.75…Equation 2.78, and diagonalizing the total Hamiltonian, and repeating the process at each value of B_z, in the range of $0T \ldots 5T$.

In Figure 2.29, usually only the states $|N=1,J,M_J\rangle$ are populated after the supersonic expansion. And the state $|1,2,2\rangle$ is usually chosen to be the target state, because $|1,2,2\rangle$ has the highest population amongst the LFS states, and $|1,2,2\rangle$ also have the largest Zeeman shift amongst $|N=1,J,M_J\rangle$ states.

Note that in Figure 2.29, the states $|1,1,-1\rangle$ and $|1,2,2\rangle$ do not have an avoided crossing at $1.6T$. The reason is, in the expressions of the matrix elements, see Equation 2.75…Equation 2.78, there are no terms which couples two different M_J together, ie all matrix elements are diagonal in M_J.

The force which governs the motion of the molecules, is proportional to the slope of the Zeeman shift. $F \propto dU/dB$. The slopes of the LFS states in Figure 2.29 appear to be quite similar. However, when examined closer, see Figure 2.30, we note that there are very different, especially for B-field $< 2T$. Hence the motion of molecules in different LFS will also be very different, despite their Zeeman shifts look similar.

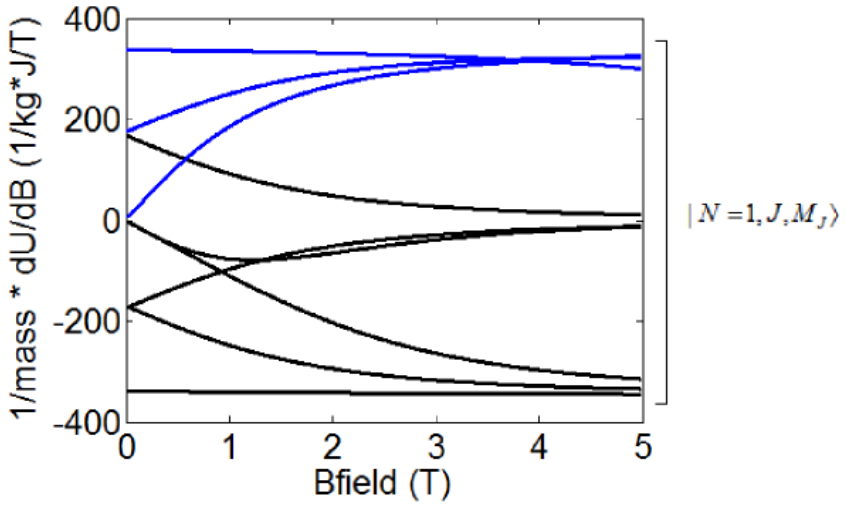

Figure 2.30 – The derivative of the Zeeman shift per unit mass, which is proportional to the force, of O_2, $|N=1,J,M_J\rangle$ states. Blue lines indicate LFS states of $|N=1,J,M_J\rangle$.

In summary, method of calculating Zeeman shift for ground state $X^3\Sigma_g^-(v''=0)$ of O_2 was described.

2.9 Majorana spin flip

Majorana spin flip happens when rapidly transitioning through near zero magnetic fields, where adiabatic approximation breaks down, and our molecules will transition into other states. For example, if we have a spin ½ particle, the spin flip would mean

$$|S=\tfrac{1}{2}, m_s=\tfrac{1}{2}\rangle \xrightarrow{spinflip} |S=\tfrac{1}{2}, m_s=-\tfrac{1}{2}\rangle$$

In our Zeeman decelerator setup, molecules travel along a straight line, along the beam axis, z-axis, and the molecules experience varying magnetic field, including near zero fields, while travelling down the decelerator. In this section, we examine how near is near zero magnetic field, what is the transition rate of this spin flip at near zero magnetic field, and whether we should be concerned about it in our experiments.

One good way to think about Majorana spin flip is to imagine Stern Gerlach experiment[62], where a beam of electrons, spin ½ particles, is deflected by an inhomogeneous magnetic field, and is split into two beams, depending on whether the spin was +½ or -½. However, if we take one of the beams, and pass it through a second inhomogeneous magnetic field, which is identical to the first field, right after the first field, then this beam will not be split again. But in a second experiment, we take the same beam after the first magnet, and pass it through a region with rapidly varying magnetic field first, where the process is nonadiabatic, then we pass the beam through the second an inhomogeneous magnetic field, the beam will be split into 2 beams. This is because, even though the beam was spin polarized (all particles were either spin up, or spin down) after the first magnet, the spins got randomized (half of the spins are up, and half of the spins are down) again in the nonadiabatic rapidly varying magnetic field.

2.9.1 Paper1: Spin-flip transitions in a magnetic trap

First, we look at a paper by Sukumar[63], where they give a simple approximate of the loss rate of a spin ½ particles for static magnetic traps with near zero field at the center due to nonadiabatic spin-flip transitions. The ability to trap neutral atoms in a static magnetic field comes from the interaction of the atomic magnetic moment with the field.

In the section of transverse phase stability, we saw that the molecules which are phase stable transversely, belongs to the stable region in the Mathieu stability diagram. The transverse oscillation of these molecules are synchronous to the varying external field, such that the effective field these transversely stable molecules see, is a constant and approximately harmonic potential. This means, our system is quite similar to a magnetic trap in the transverse direction. And hence we can try to use their analysis on our system. For example, their trap diameter, which is ~1mm, would correspond to our coil diameter.

The model of the field they used was a quadrupole field $B_x = \lambda x$, $B_y = -\lambda y$, where λ is the field gradient. In addition to the quadrupole field, there is a bias field, B_0, in the z direction $B_z = B_0$, to prevent the spin flip transition. Since $S_z = \frac{1}{2}$ is considered to be trapped, and $S_z = -\frac{1}{2}$ not trapped.

The loss, due to nonadiabatic spin-flip transition in the trap, was analyzed theoretically in the following way. Without going to details, they first identified non-adiabatic term as perturbation, and adiabatic Hamiltonian as a parabolic potential. This approximation holds as long as

$$\chi = \frac{\hbar\omega}{\mu_0 B_0} \ll 1$$

Equation 2.79

ie energy associated with oscillatory motion inside trap is much smaller than the split in energy level. Then oscillation frequency, ω, in the trap can be derived as,

$$m\omega^2 = 2\mu_0\lambda^2 / B_0$$

Equation 2.80

Then by using Fermi's golden rule, transition probability per second, w, from the wanted state to unbounded continuum is written down as $w = \frac{2\pi}{\hbar} |\langle i | \Delta T | f \rangle|^2 \rho_f$, where ΔT is the

perturbation, coming from the non-adiabatic term. And then the final simplified form, that we will be using, can be derived as :

$$w \approx 2\pi\omega e^{-4/\chi}$$

Equation 2.81 - where w is transition probability per sec, $\chi = \hbar\omega / \mu_0 B_0$ is a unitless parameter, with B_0 is background bias field, μ_0 is bohr magneton. ω is oscillation freq inside the trap $m\omega^2 = 2\mu_0\lambda^2 / B_0$, with m is the mass of the particle, λ is the field gradient, in units of G / cm.

Imagine, we now do the same analysis for O_2, $m = 32amu$, where $B_0 = 5G$, is assumed to be the minimum leak field inside the next coil stage, when the current coil is on (or in the process of being turned on/off), see Figure 2.31. $\lambda = 30000G / cm$ is the transverse field gradient at the center of the coil, and $\sim 1.5mm$ away from our beam axis. Using Equation 2.80, we get oscillation freq inside our "trap" to be

$$\omega = \sqrt{2\mu_0\lambda^2 / mB_0} = 250e3rad / s$$

First, we have to check if the inequality in Equation 2.79 holds, so that we know our assumptions are OK:

$$\chi = \frac{\hbar\omega}{\mu_0 B_0} = 0.006 \ll 1$$

Now that we know our assumptions are OK, we can continue. So, from Equation 2.81, we get the transition probability per sec to be

$$w \approx 2\pi\omega e^{-4/\chi} = 5e-300 \text{ transitions per sec}$$

Ie, essentially, using the analysis from [63], the prediction is that there is no spin flip transition for our system.

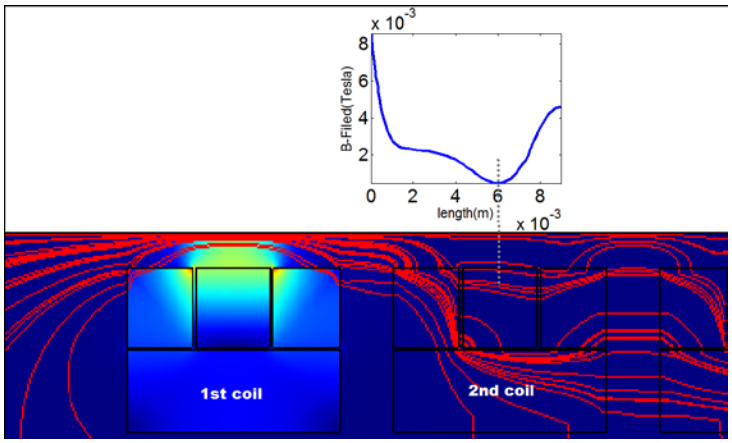

Figure 2.31 – leak field in the second coil when the first coil is at full power, 600Amperes. The field strength at minima, which is the center of the second coil, is ~5Gauss

There is always some doubt if we can use the same analysis from trap experiment for our deceleration experiment. So, next we will go through another analysis, which is spin flip calculation in magnetic guide experiment, and see if that analysis will also have the same conclusion of negligible spin flip, as this analysis did.

2.9.2 Paper2: Measurement and prediction of the speed-dependent throughput of a magnetic octupole velocity filter including nonadiabatic effects

In the paper by Nikitin [64], a magnetic octupole guide was used for the purpose of velocity filtering. The radial potential is approximately a forth order polynomial, and with a maximum field of 6250 Gauss at the edge of the octupole, and 0 Gauss on the beam axis. Inner diameter of the guide is 5mm. Length of the octupole guide is 3cm. And their target is alkali atoms such as Li, Rb and Cs. They state that their model applies to any system with a linear Zeeman splitting at low field.

The difference between magnetic guide vs Zeeman decelerator is that, Zeeman decelerator will have regions of near zero field in between the coils, compared with magnetic guide, which has near zero field at the center of the coils. And what we are trying to argue, is that we can manage to use the analysis in Nikitin's paper, to set an upper bound value to the loss due to

Majorana spin flip in our system. As molecules travel along the decelerator, the near zero field in between the coils is the region where spin flip is most likely to happen, see Figure 2.31. So, we can get an upper bound for loss due to spin flip, by assuming that the molecule is always travelling at this near zero fields. And with this assumption, we can see that our system approximately corresponds to Nikitin's model, and we just need to find the parameter b, that corresponds to our field minimum, which is the ~5Gauss, shown in Figure 2.31.

In Nikitin's paper [64] , they used the Majorana formula, and derived both the instantaneous probability for spin flip, and also the integrated form, which we will be using. The integrated from is obtained from numerically integrating instantaneous probability for spin flip from start to end of the octupole guide. They also fitted result from integration with a simple function. The fitted function of the integrated form of probability of spin flip, p, is

$$p = e^{-(\pi\xi)^{1/2}} \cos^2(2.1\xi^{1/4} + 0.54\xi^{1/2})$$

Equation 2.82 - where $\xi = \mu_B g B_0 b^4 / (2\hbar a^3 v_0)$ is called Massey parameter, $\mu_B \approx$ Bohr Magneton, g is the g factor, B_0 is the max field on the edge of guide, b is distance of particle from the beam axis, a is diameter of the guide(5mm), v_0 is the radial velocity.

This probability is the integrated probability of spin flip (from $t = -\infty$ to $t = \infty$, for a particle going in a straight path parallel to the beam axis, and misses the center of beam axis by an amount of b (ie particles oscillating inside the well who doesn't go through the center, for which the external field would be exactly zero. This looks sensible, since because at zero field, $\xi = 0$, and $p = 1$, ie spin flip will occur with 100% probability if the particle goes through the center of the guide where there is no field.

Trying out some typical values from our system, for example, let's say, $B_0 = 5Tesla$, $b = 0.7mm$, $v_0 = 3m/s$. Using Equation 2.82, we get

$$\xi = \frac{\mu_B g B_0 b^4}{2\hbar a^3 v_0} = 3e5, \text{ and } p = e^{-(\pi\xi)^{1/2}} \cos^2(2.1\xi^{1/4} + 0.54\xi^{1/2}) = 1e-400$$

The result we have here, we obtained by following steps. First, we assume our beam is on the center of beam axis. While this assumption is true, then the most losses due to spin flip will be at the lowest fields at beam axis, which is the field in the middle of adjacent coil, see Figure 2.31, and field at this point is approximately $5Gauss$, and by using our field simulation, we see that this corresponds to the value of $b = 0.7mm$ in Nikitin's analysis. This result of $p = 1e-400$ tells us that at the center of our beam axis, the loss due to spin flip is 1e-400 at maximum after travelling through the whole length of the decelerator.

We need to keep in mind that both attempts of analysis are very crude, however both analysis indicate, that the probability of spin flip is negligible, with background field of >5 Gauss. So, the conclusion is, we will not need an external constant bias field to prevent Majorana spin flip, as long as we are not 300 orders of magnitude wrong on our result of our estimation.

==========

"Any sufficiently advanced technology is indistinguishable from magic." *-Arthur Clarke*

==========

Chapter 3: The coil and the experimental setup

3.1 The coil

Zeeman decelerator is made of sequence of coils. Therefore the properties of the coils are important.

3.1.1 The design

The essential design requirements for the coils are, to generate high field and to have fast switching off speed. Magnetic field on the order of few Tesla will give adequate deceleration, higher magnetic field is preferred, but there will be practical limitation such as overheating. The switching off time can be estimated: the length of the coil, $L =\sim 1mm$, the speed of molecule $v_z = 250m/s$, therefore, molecule will spend time, $t = L/v_z =\sim 40\mu s$, inside each coil. This implies switching time of the coil should be on the order of few μs. The coils are designed in-house (with collaboration with Narvicius, Raizen, at University of Texas at Austin [31]) to meet these requirements. Figure 3.1 and Figure 3.2 shows the final design and dimensions of the coil, and measurements on this design showed satisfactory performance, see sections below.

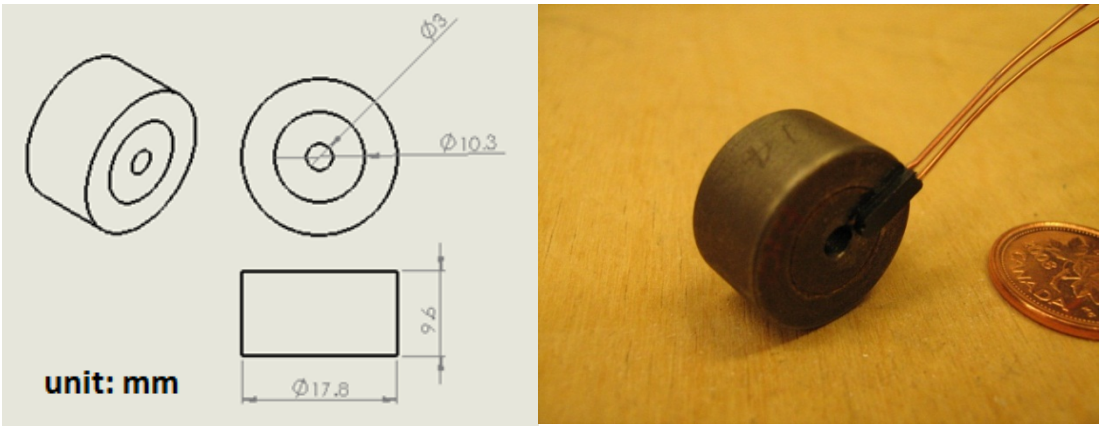

Figure 3.1 - Left figure shows Solidworks drawing of the coil, and its dimensions. The actual coil has outer diameter of 10.3mm, inner diameter of 3.0mm, shielding material have outer diameter of 17.8mm, and inner diameter of 10.3mm. Right figure shows picture of the coil, two copper wires secured with epoxy is attached.

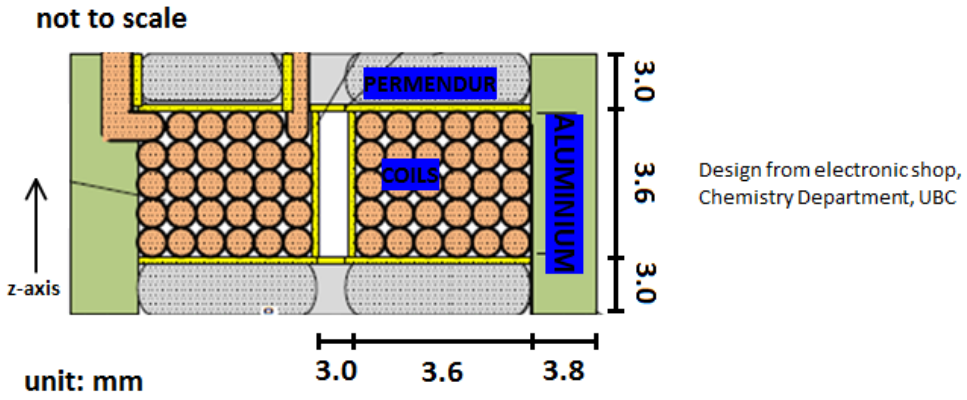

Figure 3.2 - cross section of the coil, 6x5 windings of copper wires in total, wire diameter 24 gauge (AWG) (or 0.51mm). Coils are separated from the casing with Kapton tape (yellow area) to prevent shorting.

3.1.2 Magnetic field Simulation

The tool used to simulate the static magnetic field inside the coil and the shielding effect is Poisson Superfish (will be referred as "Superfish" in remaining of the text), which is a collection of programs developed by LANL [65] [66] Superfish result is consistent with the simulated result from Switzerland and Texas at Austin [26] [67].

The shape of the B-field produced is shown in Figure 3.3: along the z-axis, there is a hill, which is used for deceleration; transverse to z-axis, there is a well (forming a saddle point) which contributes to focusing effects. The general features in Figure 3.3 (mainly shape and the depth of saddle point relative to the height) are be similar to ref [26] [67], despite that coil dimensions and current applied is different.

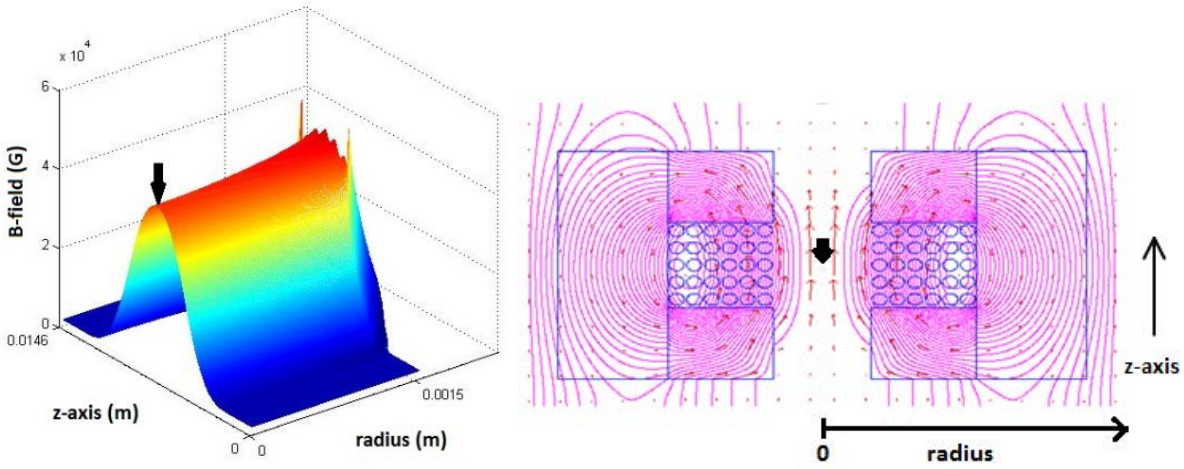

Figure 3.3 - Calculated B-field from superfish, 3D visualization (left) and 2D visualization (right). Not to scale. The potential is symmetrical at Radius=0m axis. The saddle point (which is also the center of the coil) is indicated by the thick black arrow. The input current is 700A, steel shielding, max B-field 4.4 Tesla in the center of the coil.

From Superfish calculation, the effect of shielding can be simulated. Figure 3.4 shows the enhancement and compression of the field due to shielding, with enhances the effectiveness of slowing of the coil. In Figure 3.4, without shielding material the B-field difference $(= B_{\max} - B_{\min})$ is $\sim 3T$, with shielding it increases to $\sim 4T$.

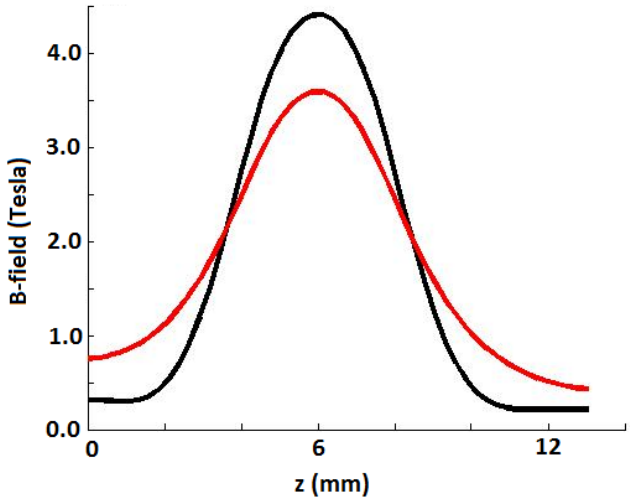

Figure 3.4 - Superfish calculation of coil without shielding (red), and coil with steel shielding (black). using design shown in Figure 3.2 and Figure 3.3, current 700A. Note the asymmetry in

the potential is due to boundary condition problem when solving Maxwell's equations, therefore only the side $z > 6mm$*, which is further away from the boundary, is used in further analysis and simulation.*

In order to simulate shielding effects of permendur in Superfish, the magnetization curve of permendur must be provided. The magnetization curve of permendur was not easily found, and hence it is included here in the text for convenience, see Figure 3.5.

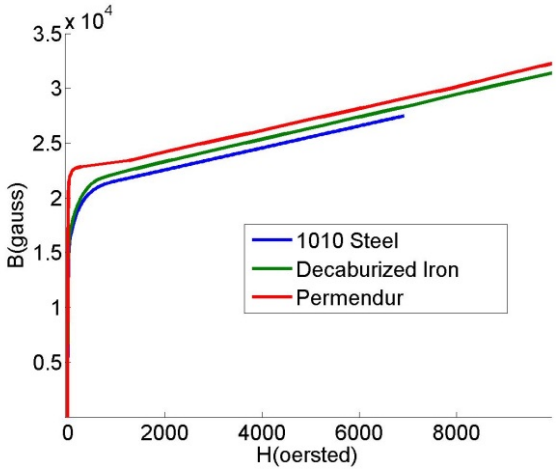

Figure 3.5 – magnetization curve for different materials. Extracted from internal materials table from Superfish, [66].

The magnetization curve is a measure of the ability of a material to support the formation of a magnetic field within itself. In other words, it is the degree of magnetization that a material obtains in response to an applied magnetic field. The definition of magnetization curve is $B(G) = \mu_r H(Oe)$, where μ_r is the relative permeability, H is the applied external magnetic field, and B is the magnetic flux density. [68]

The oersted is the CGS unit of magnetic flux density, which is closely related to the gauss. In vacuum, if the magnetizing field strength is 1 oersted, then the magnetic field density is 1 gauss. In SI units, $1\ oersted = 79.58 A/m$, and $1\ gauss = 1e-4T$.

We see in Figure 3.5, the permendur has the strongest shielding effect (largest response in B, given a value of H). This result is consistent with the measurement of the B-field, see Figure 3.8 in next section.

3.1.3 Magnetic field Measurement

The experiment used to measure the magnetic field inside each design of coil was Faraday Rotation experiment, where a Magneto-Optical crystal, TGG (Terbium Gallium Garnet) crystal was used [69]. In total, three different shielding materials were tested, permerdur, steel, and cast iron.

The Faraday rotation experiment setup consist of linearly polarized laser source, faraday rotator (TGG crystal), polarizer and photodiode detector. First step is to get the reference photocurrent in the detector, I_0, by rotating the polarizer to be at 0° to the polarization of the laser, allowing maximum transmission of the laser. Second step is to set polarizer to 90° relative to the laser, minimizing the transmission of the laser, then we pulse a current throught the coil, and a photocurrent I will be detected, which will indicate the strength of B-field generated by the current. The equation relating the B-field, and the signal we measure on the oscilloscope is following.

$$I / I_0 = \cos^2(VBd)$$

Equation 3.1 - $V = -134 Rad\ T^{-1}m^{-1}$ *is the Verdet constant [69],* $d = 2.35mm$ *is the distance of laser spent inside the TGG crystal,* B *is the magnetic field which is to be measured. Cosine is from the nature of the polarizer. Squared is something to do with turning electric field into intensity.*

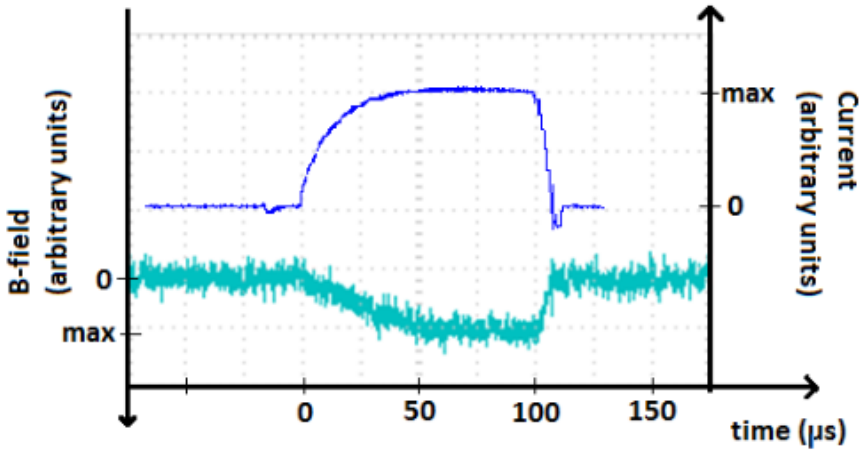

Figure 3.6 - This shows the current driving the coil (blue) and the Magnetic field in the center of the coil (purple) (using Faraday Rotation experiment). Switch on time is $\sim 50\mu s$*, then the field reaches its max value for* $\sim 50\mu s$ *(danger of overheating if not switched off), and is switched off in* $\sim 6\mu s$*.*

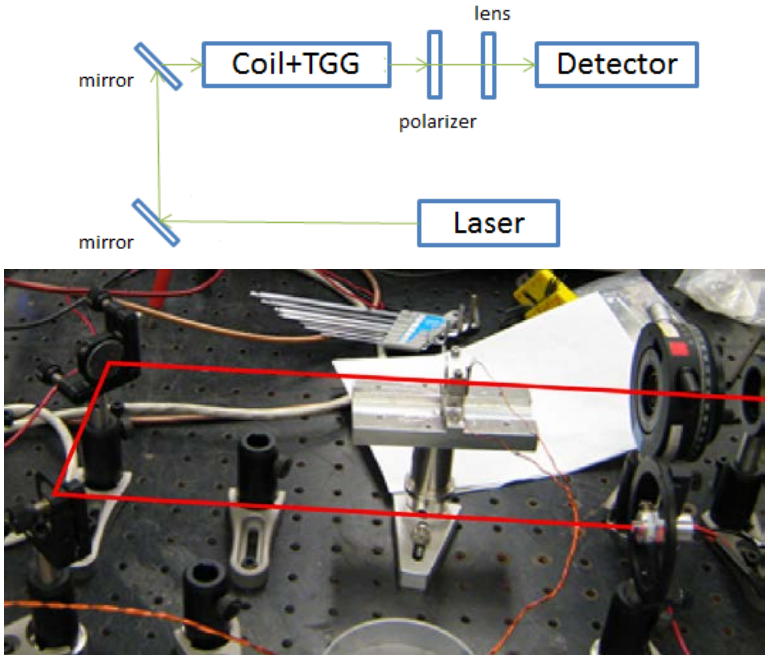

Figure 3.7 - Faraday Rotation experiment setup, red line is the laser path.

The results are summarized in Figure 3.8, and the sample data can be seen in Figure 3.6. The measurements showed that the relationship (while under the saturation value), between the

current, I, and the B field, B, is linear, as expected from the general B-field produced by solenoid equation: $B = \mu nI$, where n is windings per unit length, I is the current, and μ is the magnetic permeability.

B-field produced with permendur shielding is highest, and hence permendur will be used as the shielding material of choice.

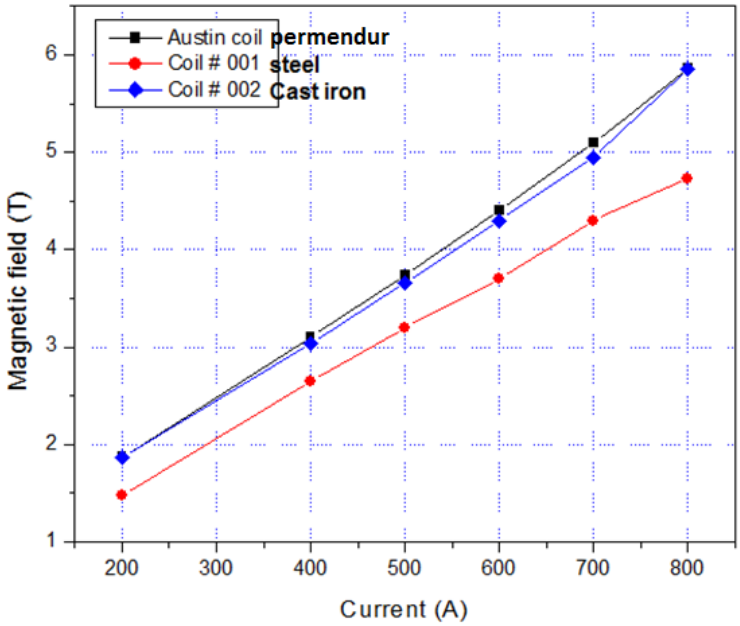

Figure 3.8 - Measurements on magnetic field produced by different shielding materials, permendur, steel, and cast iron, using Faraday rotation experiment. The error in the measurements are $\sim 10\%$ *, the error is compounded from repeated measurement of the same coil are fluctuating, and different coils give different measurements.*

The other requirement, fast switch off time, is limited by circuit design, and the inductance of the wire (we have assumed that ferromagnetic response time of the shielding material is not a concern). The current design of the electronics using IGBT, and current design of the coil gives a satisfactory and consistent switch off time of $\sim 6\mu s$, see Figure 3.6.

In summary, the design of the coil was similar to ref [31]. The shielding material was chosen to be permendur, due to magnetic shielding and thermal properties, and also due to practical reasons. Ramp up time of the coil is $\sim 50\mu s$, ramp down time is $\sim 6\mu s$. With active cooling, total time the coil can stay on (including ramp up time) without overheating is $\sim 100\mu s$. Maximum B-field reached in the current range of $600A...700A$, is $4T...5T$.

3.2 The experimental setup

The experimental setup consists of three main parts, the source (nozzle+skimmer), the 80 coil Zeeman decelerator, and the detection (ion optics+MCP), see Figure 3.9. Each part will be discussed in more detail in the following sections. In addition, there are many peripheral devices, which are not described, such as control boxes for different parts of the experiment, power circuits for the coil, feed throughs, probes, wires, pipes etc.

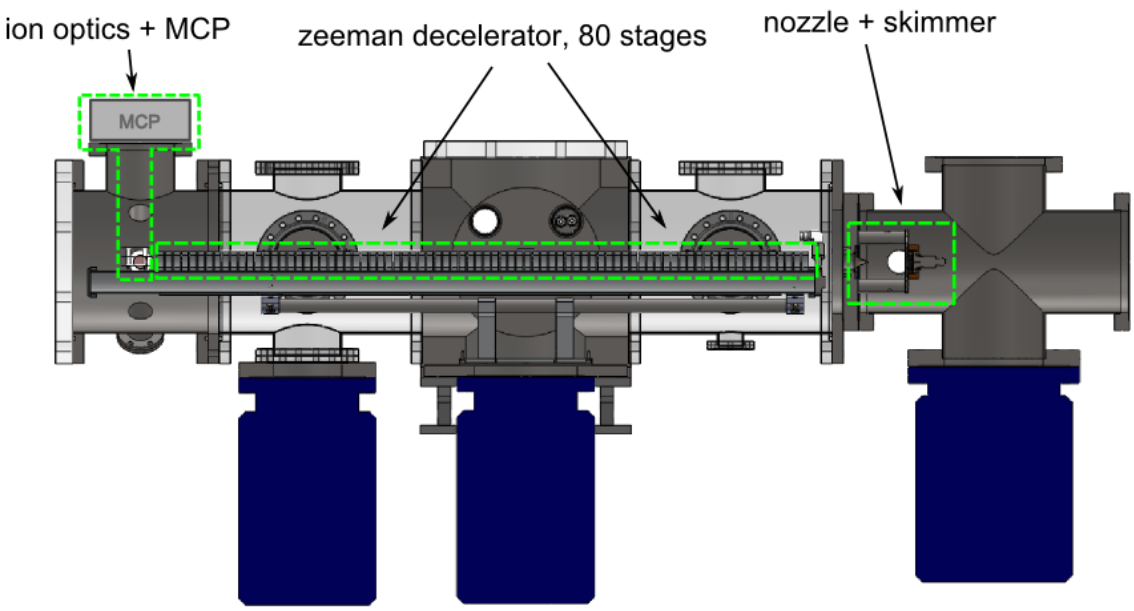

Figure 3.9 – a simplified drawing of the experimental setup. The total chamber volume is $7L+10L+30L+10L+10L \approx 70L$.

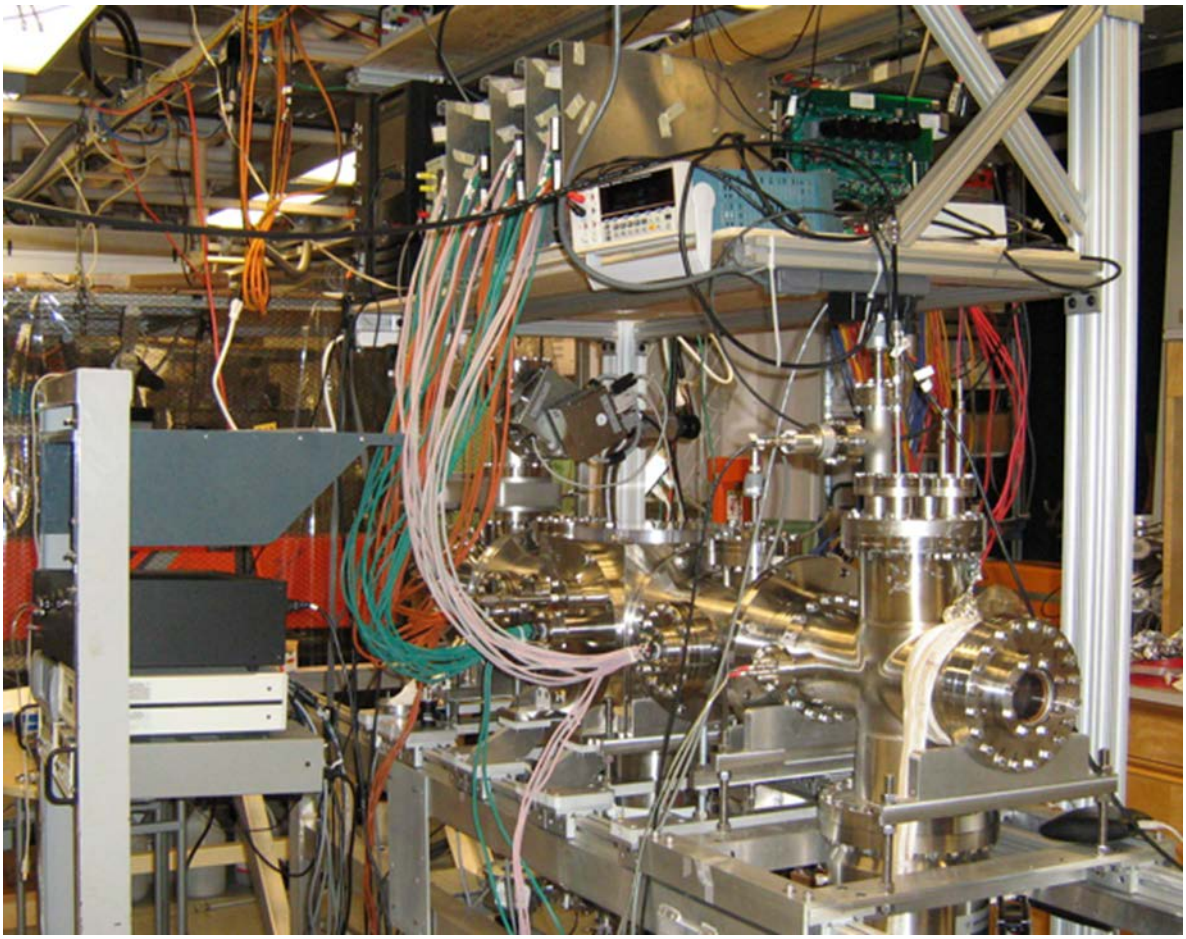

Figure 3.10 – picture of the experimental setup. 80 coil Zeeman decelerator. The arrangement is quite compact. Electronics are on the top and on the front side. Vacuum pumps are on the bottom. Laser is coming in from the back side.

3.2.1 Vacuum system and alignment

For the vacuum pumps in Figure 3.9, we have used Varian Turbo-V 1001 Navigator ($1050 L/s$) in the source chamber, and two Varian Turbo-V 551 Navigator ($550 L/s$) in the decelerator chamber and the detection chamber. All the turbo pumps are backed by a single Varian TriScroll 300 Inverter Dry Scroll Vacuum Pump [70] [71]

The size of the chambers were chosen, such that there is enough space to work inside the chamber, while keeping the chamber as small as possible to reduce pumping load.

Typical pressure values in the chamber are $0.5e-8torr...5e-8torr$ when idling.
$0.1e-6torr...1e-6torr$ during operation.

The alignment was done using a telescope. Both the nozzle and the skimmer are movable in x and y. The detection is mounted on the same optical rail as the coils. The optical rail can be adjusted in x and y in the front and in the back, providing enough degrees of freedom to be aligned with everything else. In practice, the nozzle, skimmer, and laser spot are aligned to the decelerator, and the decelerator itself is seldom adjusted.

3.2.2 The decelerator

The 80 coils that perform the deceleration are mounted in the slower chamber. A major challenge is to extract the heat generated by the coils. Each coil dissipated from 5 to 8 Watts of power per shot.

3.2.2.1 Mounting the coils and heat dissipation

An XT66 Optical Rail from Thor Labs plays a central role in the slower chamber, providing both a stiff and straight mounting platform for the coils (for alignment) as well as carrying the liquid nitrogen used to cool the assembly. Liquid Nitrogen is fed through the hollow center of the optical rail, allowing the coils and internal wiring to shed thermal energy when the slower is operating. Aluminum blocks are used to clamp the coils to the optical rail. The blocks provide a low resistance thermal path for the coils to dump heat into the rail, and hold the coils in the correct alignment.

Liquid nitrogen consumption for cooling of the coils is about 100L per day. The experiment is run at 3Hz. During the operation of Zeeman decelerator, the temperature probe mounted on the optical rail shows 90K…110K, depending on the flow rate of liquid nitrogen. When the experiment is paused, the temperature drops to 80K over time period of $\sim 10\,\mathrm{min}$.

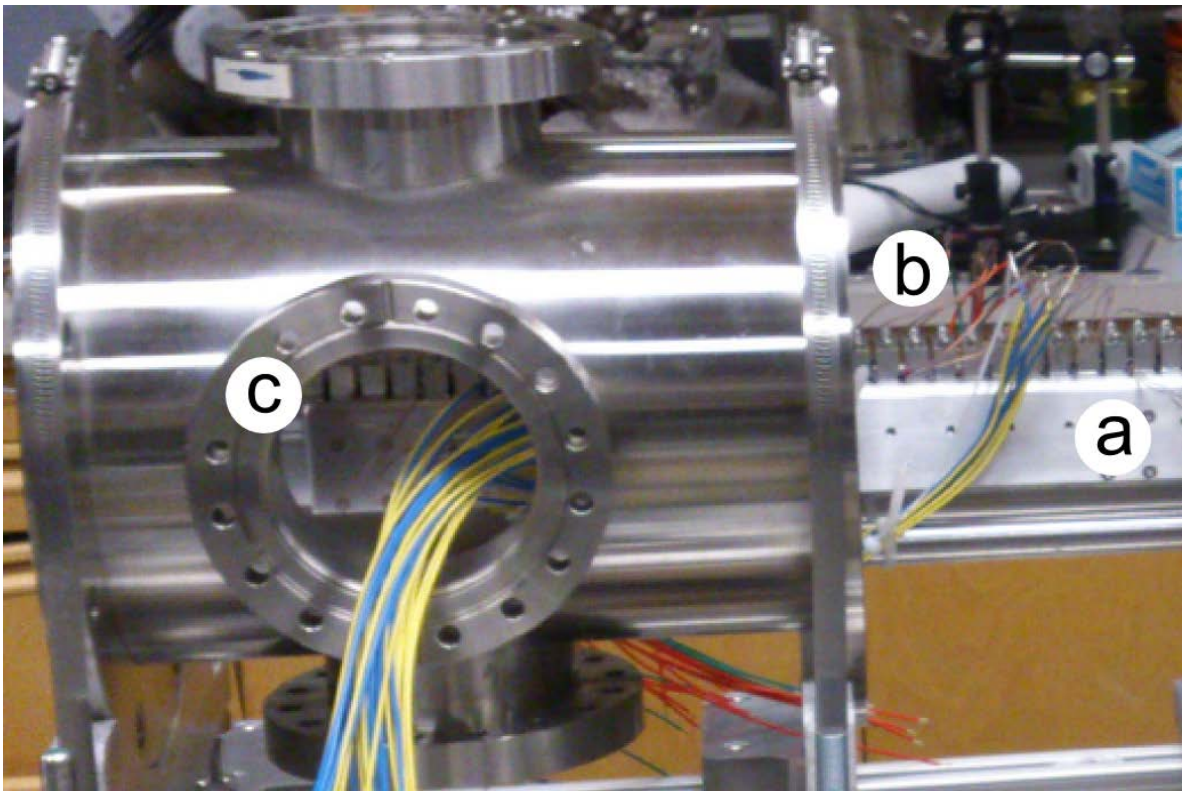

Figure 3.11 – 80 coil Zeeman during construction. a) optical rail (hollow inside for liquid nitrogen); b) Aluminum blocks/clamps holding the coils; c) one of the six feed throughs for the wires. Liquid nitrogen feed throughs not visible.

3.2.2.2 External Wiring of the coils

Painful experience taught us that even the coil wiring inside this chamber and the feed through will overheat and get burned, if the heat isn't sunk very well. It is also important to understand that the coils and wiring in the chamber are biased to 200V+, meaning that any exposed conductor area (for instance, at a wire crimp point) will act as a filament if allowed to get too hot. Exposed conductors along the wire and at the feed through will degrade if allowed to operate at high temperatures.

In order to reduce losses in the coil leads, the 24AWG wire used to construct the coil winding is spliced onto 18 ga Teflon coated wire a few inches outside of the coil housing. The splice is soldered, and the solder joint coated with high vacuum compatible epoxy to reduce off-gassing.

The Teflon wiring is color coded to help reduce errors when wiring to the feed throughs. While it is true that the Teflon wiring off-gasses more than the polyimide coating on the coil wires, the cryogenic cooling of the coil assembly keeps off gassing down to a manageable level.

The wire pairs from the coils are bundled into sets of 15 and routed to 32 pin high voltage feed throughs. The wire bundles are tied to a cold point just before entering the feed through, reducing the amount of heat transmitted to the feed throughs. Six 32 pin con-flat double ended circular connectors (Ceramtec MIL-C-26482) carry the 160 coil wires and 6 temperature sensor wires from the vacuum chamber to the external electronics.

3.2.2.3 Coil resistance at different temperatures

Care must be taken to keep wire lengths for all coils consistent, so that each coil is within a few percent of the target resistance (in our case, 0.30 Ohms). Coil resistance increases as the coil and wiring warm up. For a given applied voltage, the resulting coil current varies significantly as the coil temperature stabilizes. The experimenter needs to monitor the actual coil current, and adjust the coil voltage to maintain the desired current.

For example, when the system has been cooled to 81K (typically the lowest temperature reading seen in our system) a coil voltage of 150V will drive 700A pulses. After the system is run for a few minutes at 1Hz or faster, the coils will heat up, and 230V will be needed to drive the same 700A through the coil.

(Ω)	wire	coil	wire+coil
coil at 293K	0.152	0.070	0.222
coil at 80K	0.152	0.007	0.159

Table 3.1 – Resistance values at liquid nitrogen temperature vs room temperature, in ohms. Wire consist 90cm of 24 AWG copper wire attached to the coil, which is NOT cooled down to liquid nitrogen temperature. Coil consists of 5x6 windings of 24 AWG copper wires with inner diameter of 3mm.

We did a quick test on the resistance at different temperatures, the results are summarized in Table 3.1. The coils were connected to 90cm long wiring, to simulate the connection from the coil inside vacuum chamber to the driver electronics. The coils were cooling to liquid nitrogen temperature, but the wiring was not.

We tested the worst case scenario, where temperature varied from room temperature to liquid nitrogen temperature. The more realistic scenario would be temperature varied from idling temperature, $\sim 80K$ to operating temperature $\sim 100K$. From Table 3.1, we see that, as expected, the resistance of the coil changed a lot with temperature. However, the total resistance did not change too much, because the coil resistance has only a small contribution to the total resistance. Plus, there are additional resistances introduced from feed throughs, and possible extra lengths of wiring, which will make coil's contribution to total resistance even smaller. With all these factors in mind, we concluded that we didn't need to worry about variable resistance with respect to temperature.

The heat dissipation of the coil + permendur shielding was measured. The measurement was done by inserting one thermocouple to the inner windings of the coil; and inserting another thermocouple on the outer edge of the permendur shielding. The coil was driven with a steady current around $1...5Watts$, at room temperature, and the temperature difference of the two thermocouples was measured to be $9...14^{\circ}C/Watt$.

3.2.3 The nozzle

The goal is find a valve, which gives a short but intense pulse of molecular beam. The terms "valve" and "nozzle" are used interchangeably throughout the text.

Usually, more intensity is associated with longer opening of the nozzle, because of the slow mechanical response time of the nozzle at this time scale. However, in our case short pulse is desired, because it reduced the gas load on the vacuum pumps. Also because, we can only manipulate a part of the beam using Zeeman decelerator, which is $\sim 1mm$. The value $\sim 1mm$ is

about the size of the phase stable area, which is determined by the dimensions of the coil amongst other factors, see section about longitudinal phase stability, Section 2.2.

Ideally, the nozzle phase emittance should match the decelerator acceptance, so the short pulse should be $\sim 1mm$ in space, which corresponds to a duration of $t \approx 1mm/(400m/s) = 2.5\mu s$, where $400m/s$ is a rough estimate of the initial velocity. In practice, a balance between signal intensity and how short the pulse is need to be found. The value we have arrived at is opening durations $\sim 50\mu s$ in order to minimize the nozzle opening time, while achieving a detectable signal.

In the first generation of nozzle, we used Parker's general valve series 99 [72]. We found that the valve gave intense signal, but had long opening time $\sim 250\mu s$. In order to reduce the opening time, we then tried to use cantilever piezovalve by Janssen [73] as our second generation valve. The problem was that the piezo valve could not handle liquid nitrogen cooling (to get lower initial temperature), and the piezo valve also could not handle high enough backing pressure, we needed around $\sim 10bar$ (to get high flux).

The final generation was an in-house made valve, similar to the design of Even Lavie valve [74]. The main aspects which were varied in our valve were: different sealing technique, different plunger mass, and different spring for the plunger. After some trials, the in-house made valve had the desired properties of 1) short pulses $\sim 50\mu s$; 2) can be cooled to $\sim 80K$ without leaking; 3) can handle $\sim 10bar$ backing pressure without leaking. The in-house made valve was used in most of the experiments.

3.2.4 The detection

The detection is a standard ion optics + MCP (microchannel plate) setup. The molecules are photoionized in the center of the ion optics. The ionization laser is the second harmonic of a dye laser (Lambda Physik, ScanMate 2E, Rhodamine 6G) pumped by nano-second pulsed radiation at 532 nm (Spectra Physics/New Port, Quanta Ray Lab-130-10). The ions carry a

negative charge, and hence will be repelled by the ion optics with varying velocities, depending on the ions mass.

$$1/2mv^2 = q\Delta V \qquad \text{with} \qquad v = d/t$$

Equation 3.2 - m is the mass of the ion, v is the velocity of the ion due to ion optics, q is the charge on the ion, which is assumed to be same as charge of e^-, ΔV is the potential difference between the repeller and the round, see sections below. d is the length of the flight tube, and t is the flight time.

Then, the ions will collide with the MCP, where electron cascade occurs, amplifying the signal from single ion into a detectable avalanche of electrons, which can then be detected using an oscilloscope. Signal on the oscilloscope is similar to mass spectra, since each mass have different velocity, hence different flight time to reach MCP, see Figure 3.12.

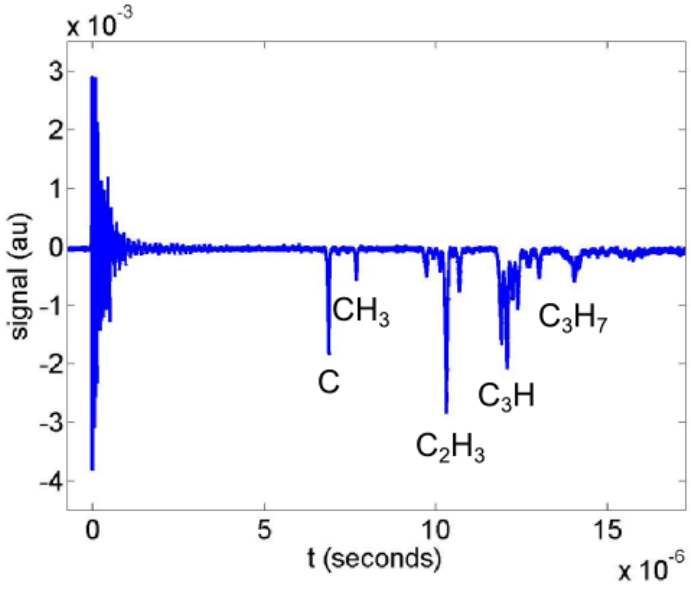

Figure 3.12 – sample oscilloscope trace. Taken in a dirty oily chamber, hence a lot of strong hydro carbon peaks. The measurement was not done using REMPI laser. When using REMPI laser, fewer peaks will be observed in the spectra. Assignment was done manually. The peak at $t = 0$ is from electrical shot noise.

3.2.4.1 Ion optics

The design of the ion optics is similar to ref [75]. There are differences in the dimensions used, in order to fit the ion optics in the chamber we are using.

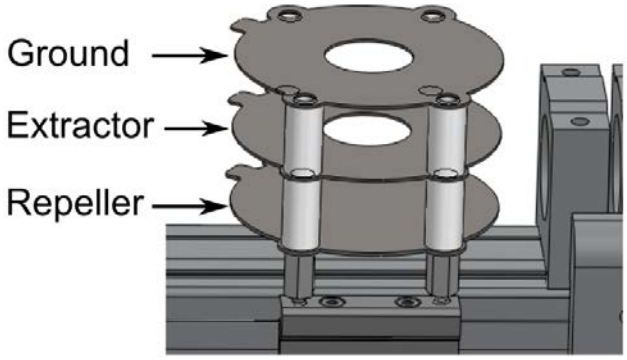

Figure 3.13 – drawing of the ion optics. Inner diameter of each plate $15mm$*, outer diameter of each plate* $45mm$*, spacing between plates* $13mm$*.*

The main purpose of the repeller is to repel ions upwards towards the MCP. A voltage difference of $\Delta V = V_R - ground = V_R$ is formed, when a voltage, V_R, is applied to the repeller , which will repel the ions towards MCP. There is also a voltage applied to the extractor, V_E, in order to collimate the ions, and enhance the amount of ions arriving at MCP.

According to ref [75], $V_E / V_R = 0.5...0.7$ should be used. The values we used in our setup is $V_E = 600V...800V$ and $V_R = 1200V$. Furthermore, by using a design similar to ref [75], we have the possibility to do velocity map imaging in the future if we so desire, by adding phosphor screen behind MCP.

3.2.4.2 MCPs

Each microchannel is a continuous-dynode electron multiplier, in which the multiplication takes place under the presence of a strong electric field. A particle or photon that enters one of the channels through a small orifice is guaranteed to hit the wall of the channel due to the channel being at an angle to the plate and thus the angle of impact. The impact starts a cascade of

electrons that propagates through the channel, which amplifies the original signal by several orders of magnitude. [76]

For our experiment, we used Del Mar Venture's MCP-GPS46 [77]. Typical voltages used were $V_I = -1500V \ldots -1800V$, with V_O grounded. V_{out} after amplification is $\sim 50mV$. Dark current was seen around $\sim -1850V$.

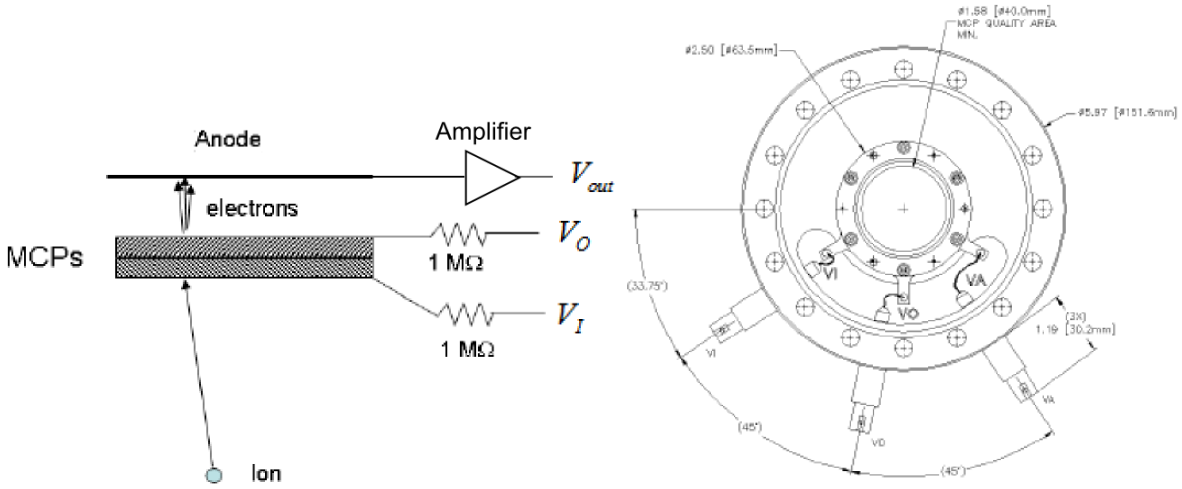

Figure 3.14 – left figure shows the schematics on how the MCP works, and the electric connections. Anode is a metal plate, which can be replaced with a phosphor screen for velocity map imaging. Right figure shows a drawing of the MCP mounted on a vacuum flange.

==========

"Never doubt that a small group of thoughtful, committed people can change the world. Indeed, it is the only thing that ever has." -*Margaret Mead*

==========

Chapter 4: Experimental results on deceleration of O_2

4.1 Results of 15 coils Zeeman deceleration of O_2

The first experiments were done using 15 stages of Zeeman coils on O_2, with following goals in mind 1) to confirm the effect of the coils on the molecular packet; 2) to confirm the validity of our simulation; 3) to strengthen our understanding of the effect of coils on the REMPI spectra; 4) to check the validity of some of the assumptions made in the simulation, such as transverse distribution.

The result of the first deceleration experiment can be seen in Figure 4.1, where pure O_2 was decelerated from initial velocity $v_{init} = 425m/s$, to final velocity $v_{final} = 415m/s$.

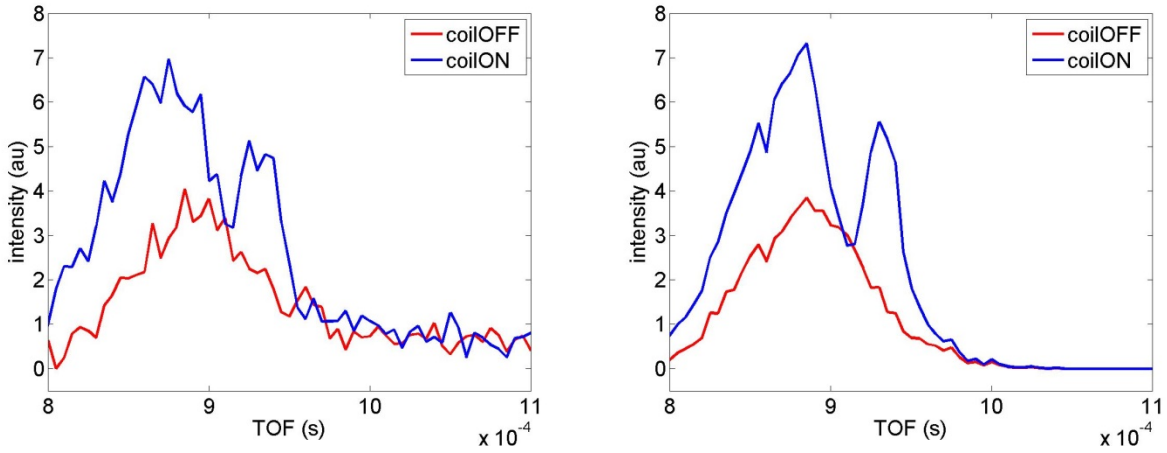

Figure 4.1 – Left figure is experiment, right figure is simulation. Pure O_2 was decelerated from initial velocity $v_{init} = 425m/s$, to final velocity $v_f = 415m/s$, using phase angle $\phi_0 = 45^\circ$, target state $|N''=1, J''=1, M_{J''}=1\rangle$, current through the coils $600A$, peak B-field on molecular axis $4.2T$, valve opening time $60\mu s$, backing pressure $4bar$, laser frequency $69570cm^{-1}$, laser power after frequency doubling is $5mJ/pulse$, number of average 10. coilOFF corresponds to the free flight of our molecular beam through the vacuum chamber, and coilON is when the decelerator is operated at $\phi_0 = 45^\circ$. Both figures are smoothed, using Savitzky-Golay, 3 points.

There are three interesting features of the result in Figure 4.1: 1) there is a peak at $0.93ms$, which corresponds to the arrival time of the synchronous molecule; 2) there is a dip at $0.915ms$, which correspond to the arrival time of the synchronous molecule without deceleration (ie free flight); 3) there is an overall increase of the signal when we turn the decelerator on.

$\lvert N'', J'', M_{J''}\rangle \rightarrow \lvert label\rangle$
$\lvert 1,0,0\rangle \rightarrow \lvert 1\rangle$
$\lvert 1,2,-2\rangle \rightarrow \lvert 2\rangle$
$\lvert 1,2,-1\rangle \rightarrow \lvert 3\rangle$
$\lvert 1,2,0\rangle \rightarrow \lvert 4\rangle$
$\lvert 1,2,1\rangle \rightarrow \lvert 5\rangle$
$\lvert 1,2,2\rangle \rightarrow \lvert 6\rangle$
$\lvert 1,1,-1\rangle \rightarrow \lvert 7\rangle$
$\lvert 1,1,0\rangle \rightarrow \lvert 8\rangle$
$\lvert 1,1,1\rangle \rightarrow \lvert 9\rangle$

Table 4.1 – re-labeling the quantum states for convenience, the lowest energy being $\lvert 1\rangle$ *, and the highest energy being* $\lvert 9\rangle$ *.*

The final TOF, which is what is obtained from the experiment, Figure 4.1, is a sum of some of the quantum states, weighted by Boltzmann's distribution. Each quantum state, $\lvert 1\rangle ... \lvert 9\rangle$, see Table 4.1, has a difference Zeeman shift, and Boltzmann's population, hence each quantum state contributes to the final TOF differently. To investigate in more detail, we have to rely on our numerical simulation. The best way to explain is to expand and plot the individual quantum states, see Figure 4.2.

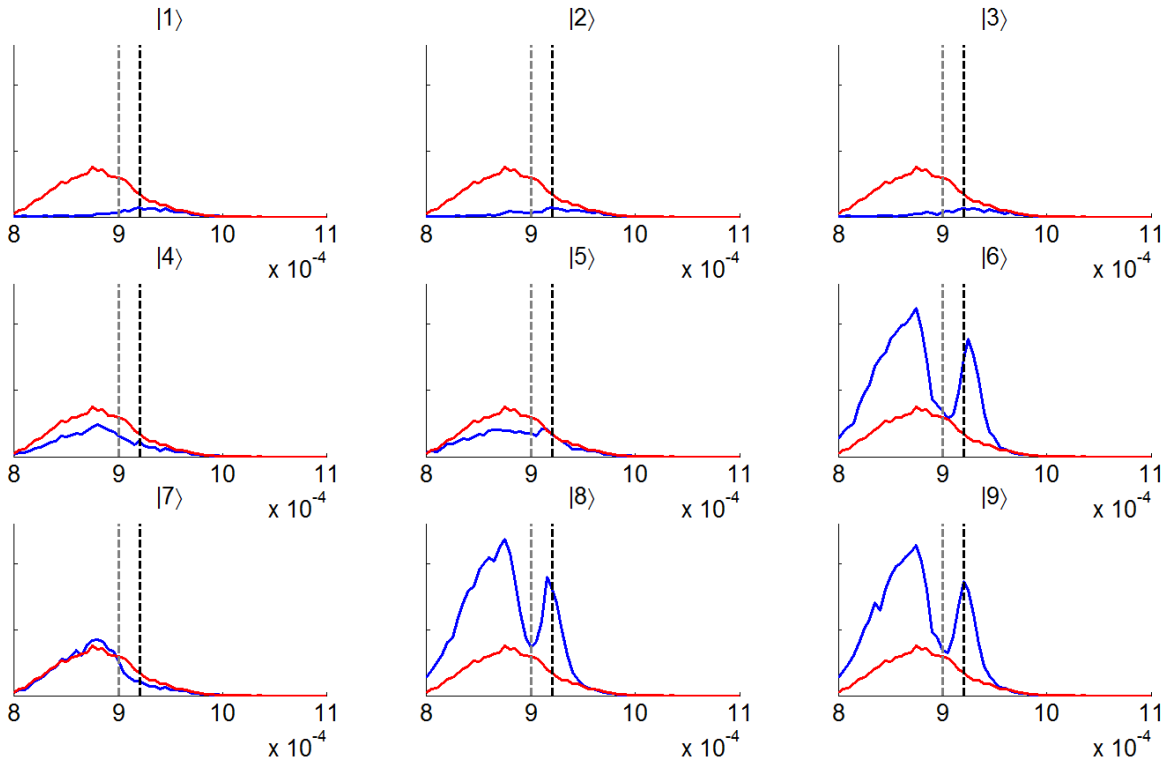

Figure 4.2 – simulation result to see the TOF for individual quantum state, before weighted by Boltzmann distribution. Red trace is coilOFF, blue trace is coilON. Vertical grey line indicates the position of "the dip", vertical black line indicates the position of "the peak". Xaxis label is TOF(s), Yaxis label is intensity.

As we saw in section 2.8, about Zeeman shift of O_2, at high enough magnetic fields, let's say $> 2.5 Tesla$, we can put the 9 states (see Table 4.1), roughly into three categories based on their Zeeman shifts: HFS (high field seeking), LFS (low field seeking) and states with small Zeeman shift.

States $|6\rangle, |8\rangle, |9\rangle$ are quite similar, and are LFS, which are the most interest, since the synchronous molecule is LFS. The double peak feature, seen in LFS states in Figure 4.2, can be explained in following way: 1) the increase of signal before the dip (before $0.915 ms$) is due to the transverse focusing of LFS which are faster than the synchronous molecule; 2) The decrease of signal at the dip at $0.915 ms$ and increase of signal at the peak at $0.93 ms$, is the actual

deceleration of LFS state. The molecules at the dip are decelerated, and hence arriving at later time, ie at the peak. Also note, the dip at $0.915ms$ carries information about our switching timing: the coil at each stage is switched off around the time, when the dip position of the packet has reached phase $\phi_0 = 45^\circ$.

States $|4\rangle,|5\rangle,|7\rangle$ are quite similar, and have small Zeeman shifts, the varying magnetic field have little effect on the molecules, hence the coilOFF and coilON signal for these states are quite similar, see Figure 4.2. It is worth noting that state $|7\rangle$ have a deceptively large Zeeman shift, yet it still behaves like state $|4\rangle \text{ and } |5\rangle$, The reason is, slope of the Zeeman shift at high magnetic field matters more, and at high magnetic field state $|7\rangle$ have a small slope in Zeeman shift.

States $|1\rangle,|2\rangle,|3\rangle$ are quite similar, and are strongly HFS. We see a huge overall decrease of signal when decelerator is on, see Figure 4.2, because HFS states are getting lost due to over focusing. Note that the small part of TOF that is not over focused, is around the position of the dip $0.915ms$, which coincide with the delay when we switch the coil off . And molecules that are faster than the synchronous molecule (arriving before the dip at $0.915ms$) are over focused and lost.

As an additional note, the frequency was set to $69570cm^{-1}$ to obtain the experimental TOF we see in, Figure 4.1. At the frequency of $69570cm^{-1}$, only states $|N''=1, J''=1, M_{J''}\rangle$ and $|N''=1, J''=2, M_{J''}\rangle$ are present, see section on O_2 REMPI. Hence the TOF in Figure 4.1 is the sum of 8 different states $|2\rangle...|9\rangle$, instead of 9 different states $|1\rangle...|9\rangle$, with each state weighted by the Boltzmann population, and the transition intensity.

4.1.1 Simulation notes on 15 coil Zeeman deceleration TOF

The parameters used in the simulation, which are fixed by the experiment, are for example longitudinal velocity distribution, timing of coil firing sequence, non-instant rise and fall time of

the magnetic field etc. Simulation parameters, which are not fixed by the experiment, which are free to vary are, exhaustively: transverse velocity distribution, detector volume and detector efficiency. Also, any jitter of experimental setup is not accounted for by the simulation. For example, jitter in duration of valve opening, jitter in mechanical delay of valve opening, jitter in max magnetic field generated shot by shot etc.

The simulation result of 15 coils Zeeman deceleration can be seen in Figure 4.1. The main features simulation succeeded to reproduce was 1) the double peaked shape of coilON; 2) the dip at $25\mu s$ to the right of peak of the free flight packet; 3) the peak is at $45\mu s$ to the right of peak of the free flight packet; 4) the width of the peak, which is $20\mu s$. The longitudinal velocity distribution was determined first, to match the free flight from experiment. And all other TOF simulation result followed naturally. It is also important to note, since the amount deceleration is small, the decelerated peak has not completely separated from the main packet, and hence many molecules which are not phase stable still remains inside the peak, and hence the peak is wider than expected.

The main difficulty for the simulation was, to reproduce the amount of signal increase due to the coils for LFS states (ratio between coilOFF vs coilON). In the end, we scaled coilON signal by factor of $1.4\times$ in order to match with the experimental TOF. There was a clear trend that with increasing initial transverse velocity distribution, or with decreasing detection volume, the ratio between coilOFF vs coilON improves, and is more similar to the experiment. We judged the scaling by factor of $1.4\times$ to be OK, since dynamics in the transverse direction was not directly measured, and therefore we assume that at certain parameter values, the simulation will match the experiment without artificial scaling. With large initial transverse velocity distribution and with small detection volume, the fraction of molecules arriving at the detection area becomes fractionally small. In order to get enough molecules into the detection area, initial number of particles had to be increased a lot, and the simulation becomes very time consuming. The more time consuming simulations were not run, and $1.4\times$ scaling happened at

transverse velocity distribution $10m/s$ ($\sim 2\%$ of initial longitudinal velocity) and at detector volume $2mm \times 2mm$.

4.2 REMPI results of 15 coils Zeeman deceleration

REMPI spectra, see Figure 4.3, was taken at the peak, $0.93ms$ which represent the arrival time of the decelerated packet as described above. The REMPI spectra were heavily correlated to the TOF spectra, one cannot analyze/simulate TOF and REMPI spectra separately. It is comforting to see our REMPI simulation results followed naturally from our TOF simulation results, and the analysis of REMPI spectra was consistent with the analysis of TOF spectra.

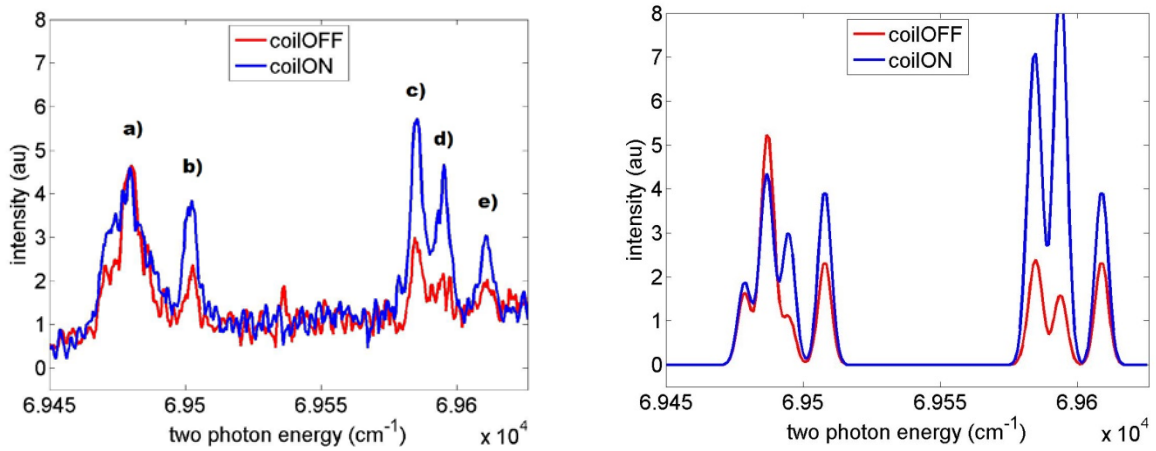

Figure 4.3 - Left figure is experiment, right figure is simulation. The REMPI spectra of O_2 was measured at the peak, with delay of $0.93ms$ in Figure 4.1. Fitted rotational temperature $5K$. Number of average 10. coilOFF corresponds to the free flight of our molecular beam through the vacuum chamber, and coilON is when the decelerator is operated at $\phi_0 = 45^\circ$. Experimental figure is smoothed, using Savitzky-Golay, 5 points. And the simulation figure was broadened using convolution with $2.3cm^{-1}$ FWHM gaussian, to match with the experiment.

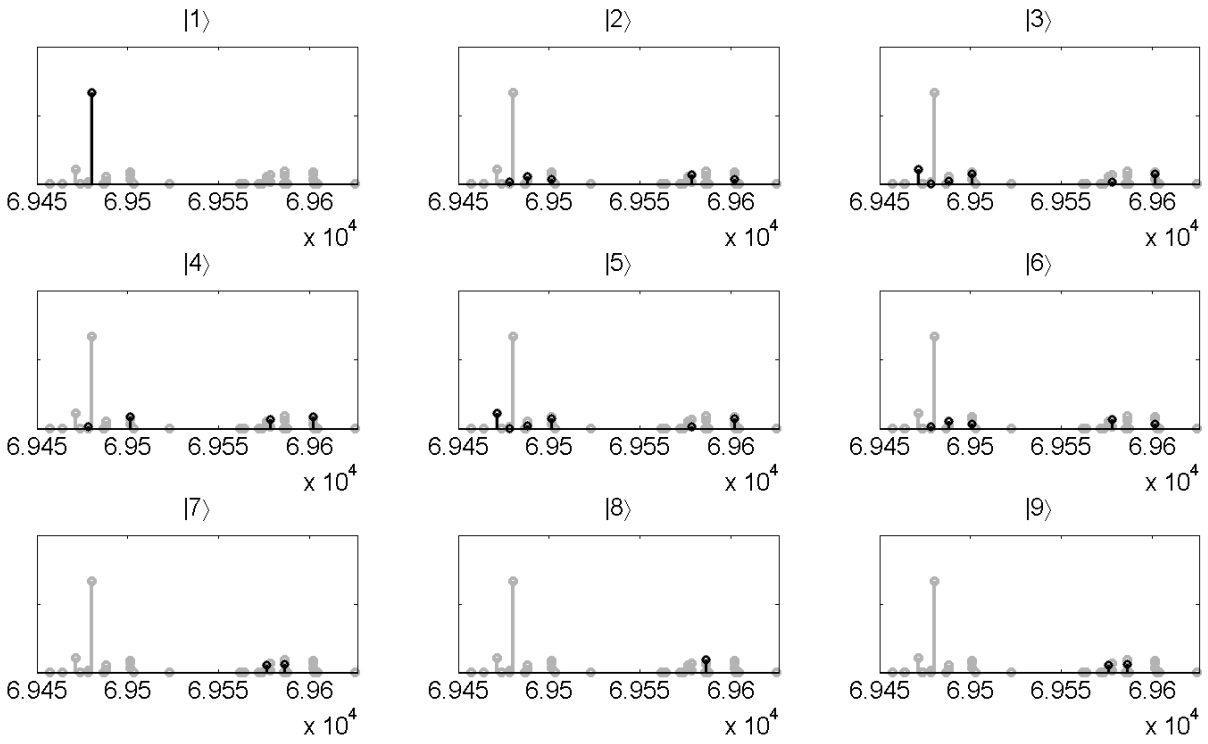

Figure 4.4 – simulation result to see the contribution to the REMPI spectra from different individual quantum state of O_2. Grey stem plot is the total REMPI spectra. Black stem plot is the REMPI spectra of the state in question. Xaxis label is Two photon energy(cm-1), Yaxis label is intensity.

The main interest, in Figure 4.3 is the effect on REMPI spectra due to the operation of the Zeeman decelerator. To analyze the REMPI spectra, we look at the change in intensity of the REMPI peaks, comparing coilON relative to coilOFF. All the changes described below are the change of coilON relative to coilOFF.

We can see peak b) in Figure 4.3, has increased. From Figure 4.4, we see that states $|2\rangle,|3\rangle,|4\rangle,|5\rangle,|6\rangle$ have approximately equal contribution to peak b). The change in REMPI signal is weighted by the transition intensity and the population change of each state at the specific delay. Hence, in the case of peak b), our weight from transition intensity is approximately the same from all five states. And therefore, the increase of peak b), is mainly

due to the change in population at the delay of $0.93ms$, which corresponds to the focusing of a LFS, state $|6\rangle$.

Similarly, peak c) only contains states $|2\rangle,|4\rangle,|6\rangle,|7\rangle,|9\rangle$, with approximately equal weight from transition intensity. In Figure 4.2 , at the delay of $0.93ms$, for states $|6\rangle,|9\rangle$ there is an increase of population, due to states $|6\rangle,|9\rangle$ are LFS, and are strongly focused. And therefore, the increase of peak c), is mainly due to focusing of LFS state $|6\rangle,|9\rangle$. We also note that peak c) increase is larger than peak b), in Figure 4.3, because peak c) contains more LFS states.

Peak d) is very similar to peak c), it contains states $|7\rangle,|8\rangle,|9\rangle$, two of which are LFS, and hence the increase.

Peak e) contains states $|2\rangle,|3\rangle,|4\rangle,|5\rangle,|6\rangle$, and the amount of increase is exactly the same as peak b), as they contain the same states.

In summary, all increase in REMPI peaks are due to the focusing and deceleration of LFS states, and the amount of increase is consistent with the TOF spectra analysis.

Looking carefully at the REMPI spectra, there are some discrepancies between the simulation and the experiment. Following features the simulation was not able to reproduce completely: peak c) is stronger than peak d); peak a) intensity does not change; and the intensity of the peaks around peak a).

The first two discrepancies, peak c) is stronger than peak d) and peak a) intensity does not change, might be accounted for, if we assume a $< 5\mu s$ systematic error in the delay. For example, if we assume REMPI scan was at $0.935ms$ delay instead of $0.93ms$, then these two discrepancies seem to disappear. Comprehensive analysis was not done on the possibilities of

systematic error, hence we leave possibility of systematic error as an idea to speculate, instead of a statement of fact.

The last discrepancy, the intensity of the peaks around peak a) does not match, can be explained by a oversight in the analysis, which didn't take into account the redistribution of $m_{J''}$ states at zero magnetic fields. We will discuss more on this topic in the 80 coil deceleration analysis.

4.2.1 Simulation notes on 15 coil Zeeman deceleration REMPI

There are three remarks on the REMPI spectra simulation, in addition to what has been discussed already.

Rotational temperature was fitted in the simulation, by matching the coilOFF REMPI spectra from experiment in Figure 4.3. Rotational temperature was determined to be $5K$.

When simulating the population change at certain delay, we had to take some width, ie $0.93ms \pm 2.5\mu s$, to get enough molecules for meaningful analysis, which might be a source of error.

There is the same $\times 1.4$ scaling factor as the TOF analysis, which we assume is due to the dynamics in the transverse direction, and assumed to be able to be corrected given enough effort.

4.3 Shifting the coil firing sequence

In another set of experiment, see Figure 4.5, we shifted the coil firing sequence by $20\mu s$ to earlier time. In other words, all coils in Figure 4.5 were fired $20\mu s$ earlier than in Figure 4.1. The effect of shifting the firing sequence is we now target a different part of molecular beam. As these were the first experiments, shifting the firing sequence also reassured us our understanding and control over the molecular beam.

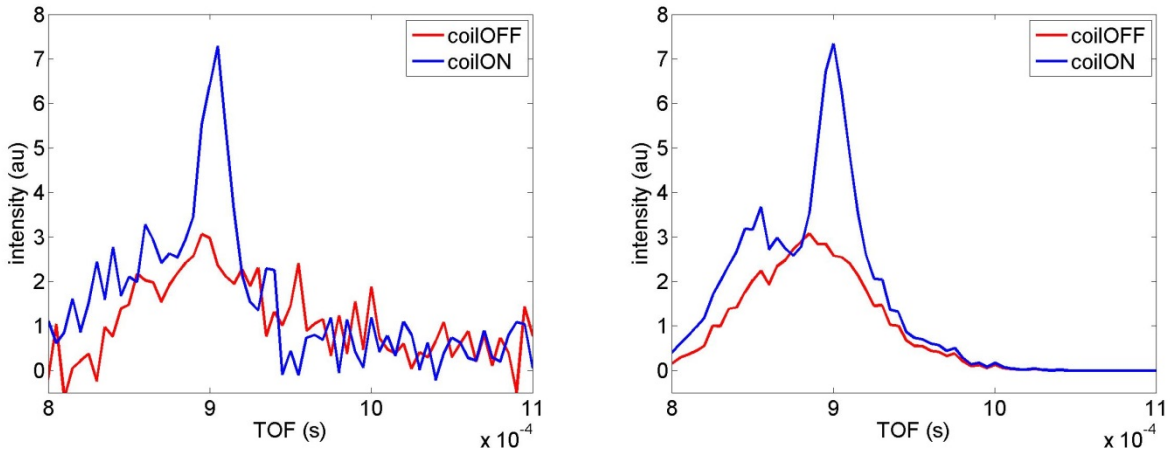

Figure 4.5 - Left figure is experiment, right figure is simulation. All coils are fired $20\mu s$ *earlier than in Figure 4.1. Otherwise all experimental conditions are identical to Figure 4.1. Amount of deceleration remains the same: from* $v_{init} = 425m/s$, *to* $v_f = 415m/s$. *Both figures are smoothed, using Savitzky-Golay, 3 points.*

The method of analysis is identical to the analysis of Figure 4.1. In summary, the main effect of shifting switching timing, is that we shifted the position of the dip relative to the free flight packet, from $0.915ms$ in Figure 4.1 to $0.895ms$ in Figure 4.5, which was expected by intuition, and confirmed by simulation. The shift of switching timing will make the peak before the dip (at $\sim 0.83ms$) so small, such that the peak is not observed in the experiment. What remains is the single peak feature (instead of double peak in Figure 4.1). The single peak feature arises is due to: we are turning off the magnetic field $20\mu s$ earlier, and hence the faster LFS molecules (before the dip) have less chance to get focused, and therefore the peak before the dip is not observed. The peak which is observed in Figure 4.5 is the decelerated peak, similar to Figure 4.1.

The shifted coil firing sequence experiment, Figure 4.5, has exact same experimental condition as Figure 4.1, except the firing sequence shift. It is comforting to see our simulation results for Figure 4.5 followed naturally from simulation result of Figure 4.1. The simulation managed to

reproduce: 1) the single peaked shape; 2) the location of the dip is at $5\mu s$ to the left of peak of the free flight packet; 3) the peak is at $15\mu s$ to the right of peak of the free flight packet; 4) the width of the peak is $20\mu s$.

REMPI spectra at $0.905ms$ in Figure 4.5 was also measured, see Figure 4.6. The analysis of REMPI spectra is identical to the analysis of Figure 4.3 in the section above. Comparing the current REMPI spectra, Figure 4.6, with the REMPI spectra above, Figure 4.3, interestingly they are very similar, which suggests that the physics are similar, which detailed analysis showed to be the case.

Simulation results predicts that, there should be 20% less in signal increase in peak c) and peak d) in Figure 4.6 compared to Figure 4.3. We can almost argue that this feature is also observed in the experiment, if we look at the relative intensity peak c) and peak d) to the intensity of peak a), instead of peak c) and d)'s absolute intensity.

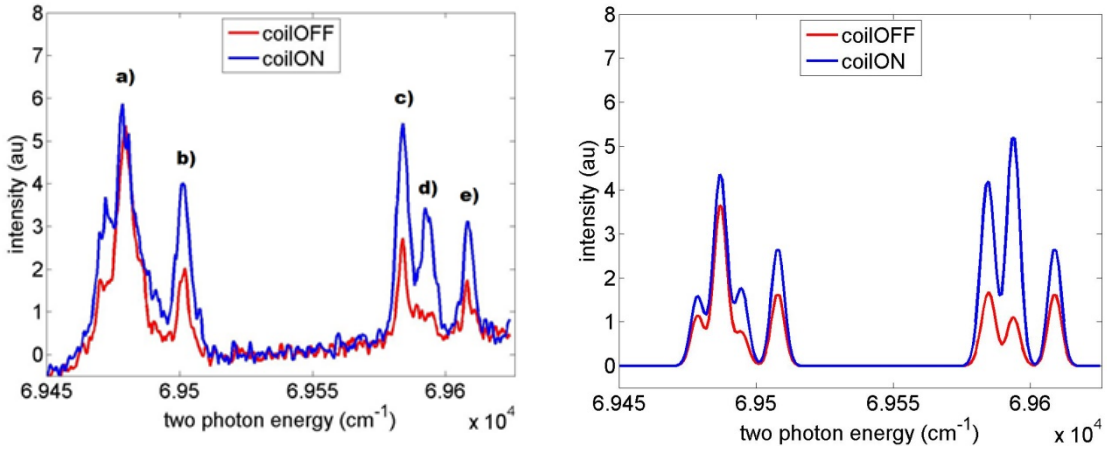

Figure 4.6 - Left figure is experiment, right figure is simulation. All coils are fired $20\mu s$ earlier than in Figure 4.3. Otherwise all experimental conditions are identical to Figure 4.3. Experimental figure is smoothed, using Savitzky-Golay, 5 points. And the simulation figure was broadened using convolution with $2.3cm^{-1}$ FWHM gaussian.

In summary, we presented our first experimental results for 15 coils Zeeman deceleration of O_2 . We have obtained two different TOF profile, and two REMPI spectra associated with the respective TOF spectra. And our simulation has succeeded in simulating our set of heavily correlated experimental data.

4.4 Results of 80 coils Zeeman deceleration of O_2

The goal of the decelerator is to decelerate the molecular beam as close to $0m/s$ as possible. One trivial way to increase the amount of deceleration is to add more coil stages to the decelerator. We have constructed a new Zeeman decelerator, consisting of 80 coil stages, with total length $0.96meters$. Compare this with before, 15 stages, total length $0.18meters$. In this section, the experimental result, simulation result and analysis of 80 coils Zeeman deceleration of O_2 will be presented.

The main result for the 80 coil Zeeman deceleration of O_2 is seen in Figure 4.7. Using 80 stages, $20\%\ O_2$ seeded in Kr was decelerated from the initial velocity of $v_{initial} = 320m/s$, to final velocities $v_f = 253m/s ... 53m/s$, using phase angle $\phi_0 = 30^\circ ... 49^\circ$. In terms of kinetic energy, initially we have $E_{kinetic} = \frac{1}{2}mv^2 = 2.72\text{e-}21joules$. For $\phi_0 = 30^\circ, 38^\circ, 43^\circ, 47^\circ, 49^\circ$, respectively, $37\%,\ 59\%,\ 76\%,\ 90\%,\ 97.4\%$ of initial kinetic energy has been removed.

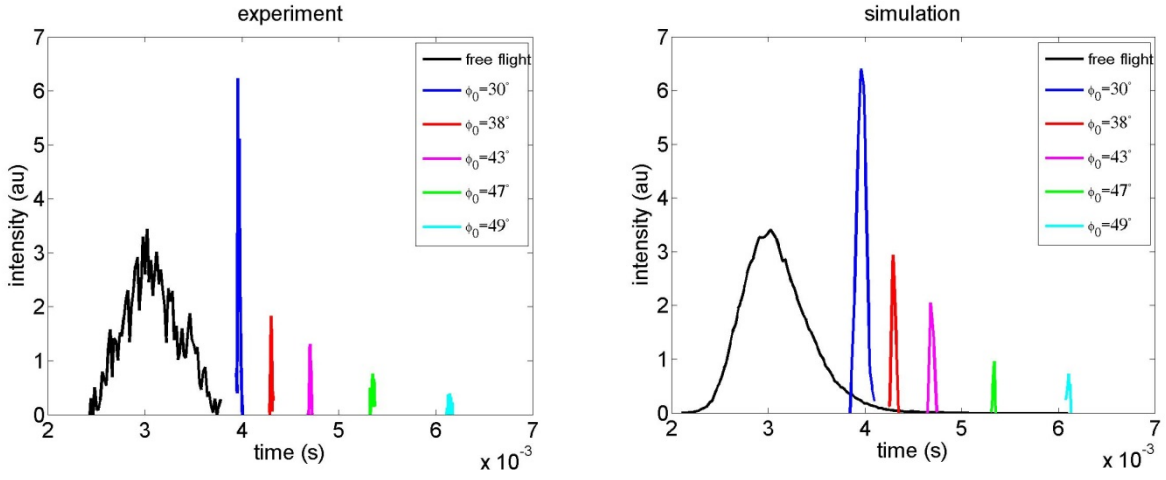

Figure 4.7 - Left figure is experiment, right figure is simulation. Using 80 stages, $20\%\ O_2$ seeded in Kr *was decelerated to various final velocities from the initial velocity of* $v_{initial} = 320m/s$. *For phase angle,* $\phi_0 = 30^\circ$, *final velocity is,* $v_f = 253m/s$; *For* $\phi_0 = 38^\circ$, $v_f = 205m/s$; *For* $\phi_0 = 43^\circ$, $v_f = 158m/s$; *For* $\phi_0 = 47^\circ$, $v_f = 102m/s$; *For* $\phi_0 = 49^\circ$, $v_f = 52m/s$. *Target state was* $|N" = 1, J" = 2, M_{J"} = 2\rangle$, *current through the coils* $600A$, *peak B-field on molecular axis* $4.2T$, *valve opening time* $60\mu s$, *laser frequency* $69568cm^{-1}$, *laser power after frequency doubling is* $6.5mJ/pulse$, *number of average* $40...80$.

In *Figure 4.7*, for the experimental data, the area under the peak between decelerated peaks and free flight is $\sim 10\%$, for $\phi_0 = 30^\circ$. Note that this efficiency is the combined effect of nozzle and decelerator together and not the efficicency of the decelerator alone.

We can see, all decelerated peaks in Figure 4.7 are separated from the main packet (black trace in Figure 4.7). Intuitively, only LFS states can be decelerated, and later in the analysis of REMPI spectra, we see it is indeed the case. Analysis of 80 coils deceleration, Figure 4.7, is similar to the analysis of 15 coil deceleration, Figure 4.1, but more simplified, due to the fact that only LFS states are present. To be more precise, instead of analyzing all nine states, $|1\rangle...|9\rangle$, in 15 coil deceleration. We only need to analyze three LFS states, $|6\rangle,|8\rangle,|9\rangle$, in 80 coil deceleration, see Figure 4.12.

The mean velocity of the main packet, black trace in Figure 4.7, is actually $380m/s$, with standard deviation of $40m/s$. However, the initial velocity we target is $v_{init} = 320m/s$, different from the mean velocity, which has initial velocity around $320m/s$.The reason is trivial, targeting a lower initial velocity will give us lower final velocity. The drawback is, there are fewer molecules at the velocity $320m/s$, since the mean velocity is at $380m/s$, and hence weaker signal for the decelerated peak. Through trial and error, we found that targeting $v_{init} = 320m/s$ gave us the largest amount of deceleration which we can still detect.

TOF scans on the main packet, for each corresponding decelerated peak, were not measured. Because as the decelerated peak becomes slower, their signal becomes weaker and narrower (See Section 2.2, about longitudinal phase stability). Hence, more averages with smaller steps are needed, and experiment becomes too time consuming if main packet had to be scanned as well.

There are couple of mismatches between the experiment and the simulation seen in Figure 4.7. Firstly, the simulation of the main packet, the black trace on the right in Figure 4.7, is reduced in intensity by factor of $0.1\times$ in order to match the experiment. In other words, the relative intensity of the main packet, and the decelerated peaks was not reproduced in the simulation. The reason we suspect is the transverse focusing effect, and wrongly assumed initial transverse velocity distribution. Despite of this mismatch, simulation still managed to reproduce the relative intensity between the decelerated peaks, which is more important to us.

Second mismatch is the peak width of the decelerated packet. At higher phase angles, $\phi_0 = 47^\circ, 49^\circ$, simulation reproduced the experimental result. However, at lower phase angles, $\phi_0 = 30^\circ, 38^\circ, 43^\circ$, the peak in the simulation is visibly wider than experimental result.

Further analysis on the simulation showed that, at low phase angle, there are some amount of molecules, which are not longitudinally phase stable (outside the separatrix), yet these molecule still exist at the end of the decelerator. The reason is, the molecules outside of the separatrix didn't oscillate fast enough in phase space to be lost, and hence wider decelerated peaks at lower phase angle. So, it is still unknown to us, why experimental result didn't show wider peaks at lower phase angle.

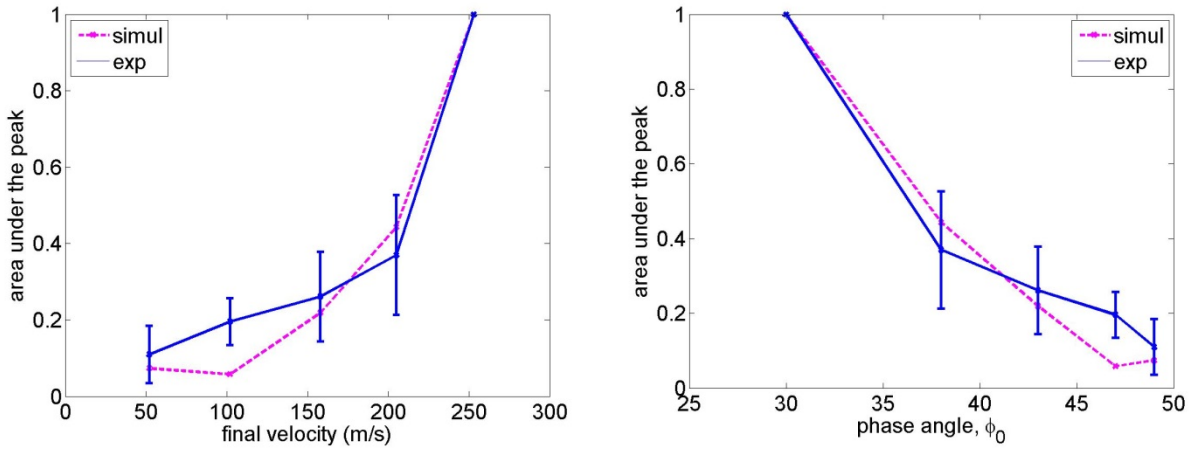

Figure 4.8 - Left figure is plot of final velocity vs area under the peak. Area under the peak shows the amount of decelerated molecule. Right figure is plot of phase angle vs area under the peak. Area under the peak for $\phi_0 = 30^\circ$ *is normalized to be one. All other data is relative to* $\phi_0 = 30^\circ$*. Reminding that at* $\phi_0 = 30^\circ$*, the deceleration efficiency is* $\sim 10\%$

We can summarize the deceleration results, the summary of Figure 4.7 can be seen in Figure 4.8. In Figure 4.8, the relative intensities of the decelerated peaks are compared. Normalization is done such that $\phi_0 = 30^\circ$ is normalized to be one, and all peaks are references to $\phi_0 = 30^\circ$. The error bars in the experiment comes from repeated measurements of the same signal in different experiment sessions. The simulation predicts the trend measured by the experiment within reasonable errors.

The signal to noise ratio in Figure 4.8 was not very good. Signal decreased as we increased the phase angle, which was to be expected from longitudinal phase stability analysis. At the highest phase angle, $\phi_0 = 49^\circ$, the signal to noise ratio was close to 1:1. And consequently, we were not successful in detecting any decelerated packet using higher phase angle than $\phi_0 = 49^\circ$, ie final velocity lower than $v_f = 52 m/s$ was not detected.

Note that, from analysis on transverse motion, transfer matrix method, the cut off velocity estimated by the theory was $v_f = 38m/s$. We want to speculate that cut off velocity may play a role, as to why we were not successful in detecting final velocities lower than $v_f = 52m/s$.

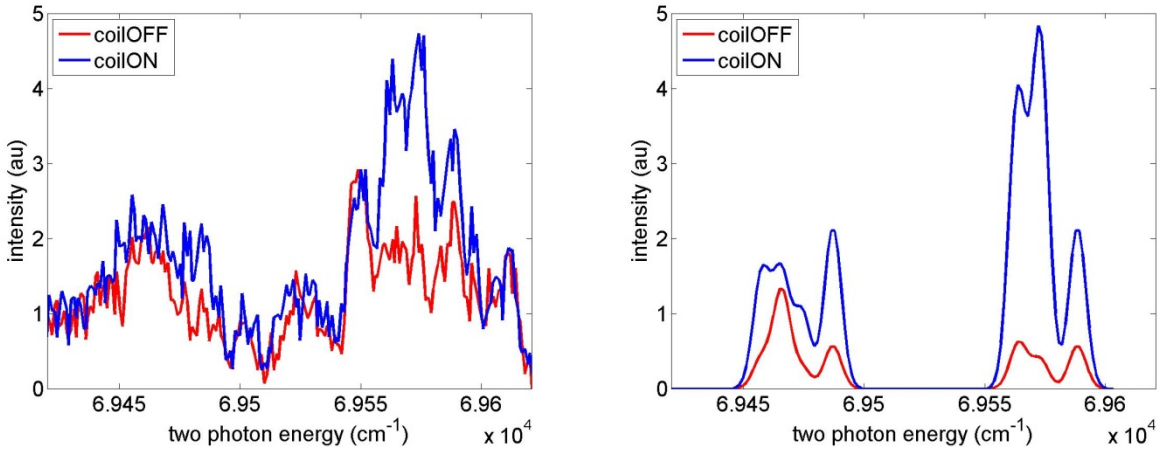

Figure 4.9 - Left figure is experiment, right figure is simulation. The REMPI spectra of O_2 was measured for $\phi_0 = 43^\circ$, $v_f = 158m/s$. The REMPI spectra were taken at delay of $4.70ms$ of Figure 4.7, corresponding to the decelerated peak. Assumed rotational temperature to be $5K$. Number of average 40. Experimental figure is smoothed, using Savitzky-Golay, 5 points, and the simulation figure was broadened using convolution with $3.5cm^{-1}$ FWMH gaussian.

The REMPI spectra was measured on the decelerated peak, $\phi_0 = 43^\circ$, $v_f = 158m/s$, see Figure 4.9. The REMPI spectra was measured for $\phi_0 = 43^\circ$, instead of $\phi_0 = 49^\circ$, is matter of signal to noise ratio. At $\phi_0 = 49^\circ$, the REMPI spectra becomes too noisy to analyze properly.

The analysis is identical to the analysis of REMPI for 15 coil decelerator, perhaps even easier, due to presence of fewer states, see Figure 4.3. Comparing experiment and simulation in Figure 4.9, we see they are somewhat different. This is due the bad vacuum we were suffering from during the time of the experiment. The vacuum pressure in the detection chamber was $> 5e-8torr$ (without pulsing of the nozzle). Evidently, at this pressure, there is enough residue

background O_2 to be detected. To summarize, in Figure 4.9, simulation result shows the REMPI for the decelerated peak, while experiment result shows REMPI of background + decelerated peak.

Due to the presence of high background in the experiment, it is not possible to fit a rotational temperature from Figure 4.9. Hence, we assumed our molecular beam is similar to the 15 coil experiments, which means we assumed rotational temperature to be $5K$.

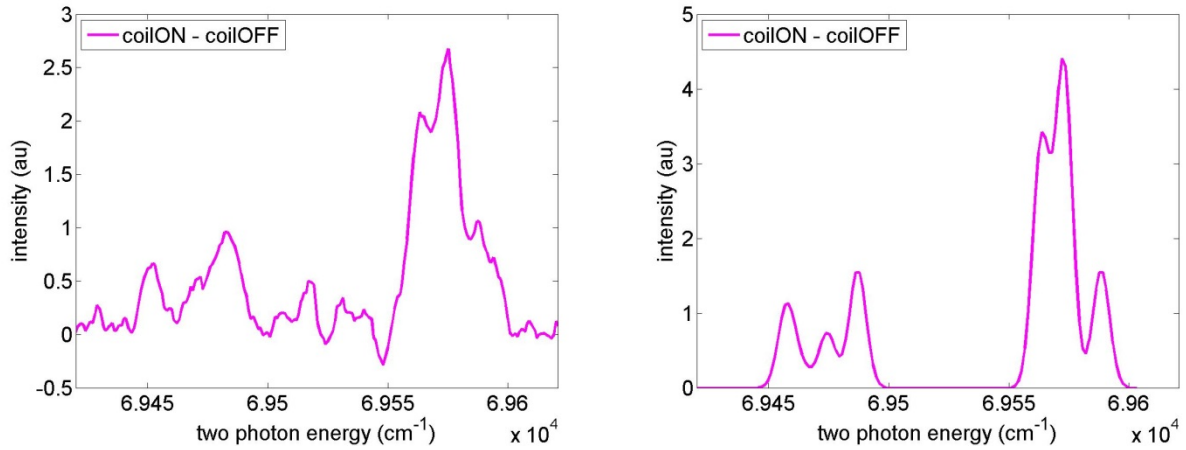

Figure 4.10 - Left figure is experiment, right figure is simulation. We see the subtraction of coilON and coilOFF of Figure 4.9, which indicates the change of REMPI spectra due to operation of Zeeman coils. The subtraction helps to eliminate the non-meaningful REMPI peaks due to background residue O_2.

Because of the high background residue, it is more meaningful to compare the subtracted signal, ie $coilON - coilOFF$, see Figure 4.10. The subtracted signal shows the effect due to operation of the Zeeman coils. There is a good match between the simulation and experimental result. Analysis of Figure 4.10, using Figure 4.4, shows that only LFS states are left in the decelerated peak, which is intuitive, because only LFS states can be decelerated.

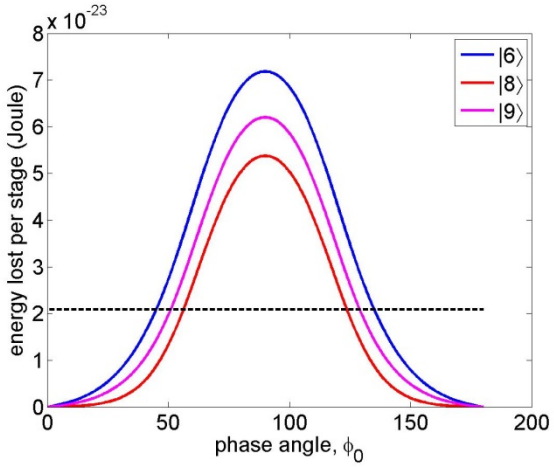

Figure 4.11 – the energy lost per stage for different states of O_2. The black dotted line indicates the amount of energy lost, when we decelerate state $|6\rangle$, at phase angle $\phi_0 = 45^\circ$. Exact same amount of energy is lost, if state $|9\rangle$ is decelerated at $\phi_0 = 51.5^\circ$; or state $|8\rangle$ is decelerated at $\phi_0 = 58^\circ$. Assuming current in coils $600A$, peak magnetic field along beam axis $4.2T$.

However, more precisely, the analysis shows that *all* LFS states, namely states $|6\rangle,|8\rangle,|9\rangle$, are present. The deceleration other than the target state is both observed in the REMPI spectra above, and in the numerical simulation. The reason is, the Zeeman shift of the LFS of O_2 are quite similar, see Figure 5.3.

From another perspective, we can examine the amount of kinetic energy lost per stage for different LFS states, see Figure 4.11. When we target state $|6\rangle$, at phase angle $\phi_0 = 45^\circ$, $2.087\text{e-}23 joules$ of kinetic energy is lost per stage. Same amount of energy is lost, if state $|9\rangle$ is decelerated at $\phi_0 = 51.5^\circ$; or state $|8\rangle$ is decelerated at $\phi_0 = 58^\circ$, ie accidental deceleration of non targeted states.

In other words, operating the decelerator to target state $|6\rangle$, at phase angle $\phi_0 = 45^\circ$, has the exact same timing sequence as operating decelerator to target state $|8\rangle$ at some higher phase angle. And if the Zeeman shifts between the states are very different, then the phase angle

difference between the target state, and the state which is accidentally decelerated, will be large. And when phase angle difference is large enough, there will not be any states other than the target state.

In summary, the deceleration of non-target state is accidental, and only happens when the Zeeman shift of the states are similar enough in the range of magnetic field that is typical for the experiment.

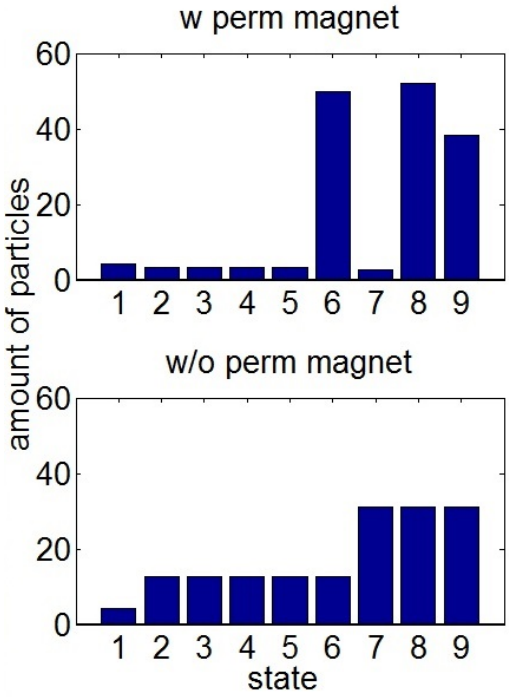

Figure 4.12 – population redistribution of states $|1\rangle ... |9\rangle$ *of* O_2 *. For labeling of the states, see Table 4.1. Top figure, when permanent magnet is present between last stage of decelerator and the detection point, the population of each* $M_{J"}$ *state is preserved. Bottom figure, without such magnet, the* $M_{J"}$ *states will collapse within the same* $J"$*, and the population of each* $M_{J"}$ *state is the average of all* $M_{J"}$ *states within the same* $J"$*.*

The last point on analysis of REMPI spectra is, population redistribution among $M_{J"}$ states within the same $J"$. There is population redistribution when there is not sufficient amount of external magnetic field to maintain the quantization axis of $M_{J"}$.

The top figure of Figure 4.12 shows the population distribution of states $|1\rangle...|9\rangle$ of O_2, if we maintain the quantization axis (which is not done in our experiments) by putting a permanent magnetic between the last deceleration stage and the detection region. And consequently, the top figure of Figure 4.12, is also the population distribution right after the decelerator, since the population in each state is conserved.

The bottom figure of Figure 4.12 shows the population of each state, after population redistribution among $M_{J"}$ states within the same $J"$. This is the case, when there is no magnetic field to preserve the quantization axis. We see that after population redistribution, $M_{J"}$ states within $|N"=1, J"=1, M_{J"}\rangle$ (ie states $|7\rangle,|8\rangle,|9\rangle$) are equal; $M_{J"}$ states within $|N"=1, J"=2, m_{J"}\rangle$ (ie states $|2\rangle,|3\rangle,|4\rangle,|5\rangle,|6\rangle$) are equal; and population of $|N"=1, J"=0, M_{J"}\rangle$ (ie state $|1\rangle$) doesn't change, since there is only one $M_{J"}$ state within $J"=0$.

The population redistribution, Figure 4.12, combined with the REMPI contribution of each state, Figure 4.4, will give the simulation result for REMPI spectra, which is seen in Figure 4.9. Without the careful consideration of redistribution of population, the simulated REMPI spectra will be different, see Figure 4.13, and will be less similar to the experiment. This would also explain the difference between experiment and simulation seen in peak a) in Figure 4.3, since at that time, redistribution of population was not carefully considered.

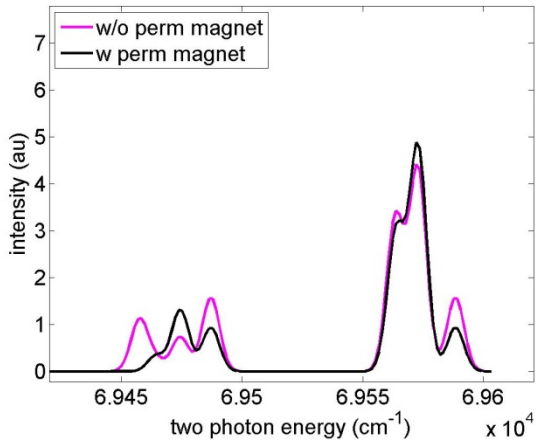

Figure 4.13 – Purple trace is the same simulation result we see in Figure 4.9. Black trace is the REMPI spectra we would detect, if we had a permanent magnet between last stage of decelerator and the detection point. The function of magnet is to preserve $M_{J''}$*, see Figure 4.12.*

In summary, details on deceleration of O_2 were presented in this section. The most deceleration we got with detectable signal is $v_f = 52m/s$, S/N ratio has to be improved slightly if the goal is to trap O_2.

==========

"If you reject reason, then for a little while everything is possible." -*some famous writer*

==========

Chapter 5: Experimental results on deceleration of CH_3

5.1 Results of 15 coils Zeeman deceleration of CH_3

There are two sets of experiments done on 15 coil deceleration of CH_3. First set of experiment is the deceleration compared vs focusing of the CH_3 beam, see Figure 5.1 a) and c). And the second set is varying amount of deceleration by varying phase angle, see Figure 5.1 b) and d). Both set of experiments have similar logical progression as the 15 coil and 80 coil deceleration of O_2. The purpose of the experiments is to verify we can understand and control the deceleration process of CH_3.

First set of experiment is the deceleration and focusing of the CH_3 beam, see Figure 5.1 a) and c). Experiments on deceleration of CH_3 were done with 15 coils Zeeman decelerator, after the 15 coil O_2 experiments. CH_3 was decelerated from initial velocity $v_{init} = 510 m/s$, to final velocity $v_f = 470 m/s$, using phase angle $\phi_0 = 60^\circ$, see Figure 5.1. Nozzle temperature $135K$, laser frequency $69854.4 cm^{-1}$ (Q branch), laser power after frequency doubling is $5 mJ / pulse$, number of average 20. Target state is $|N = 0, K = 0\rangle$. CH_3 was produced by discharging $15\%\ CH_4$ in Ar, using discharge voltage $750V$, discharge duration $50 \mu s$.

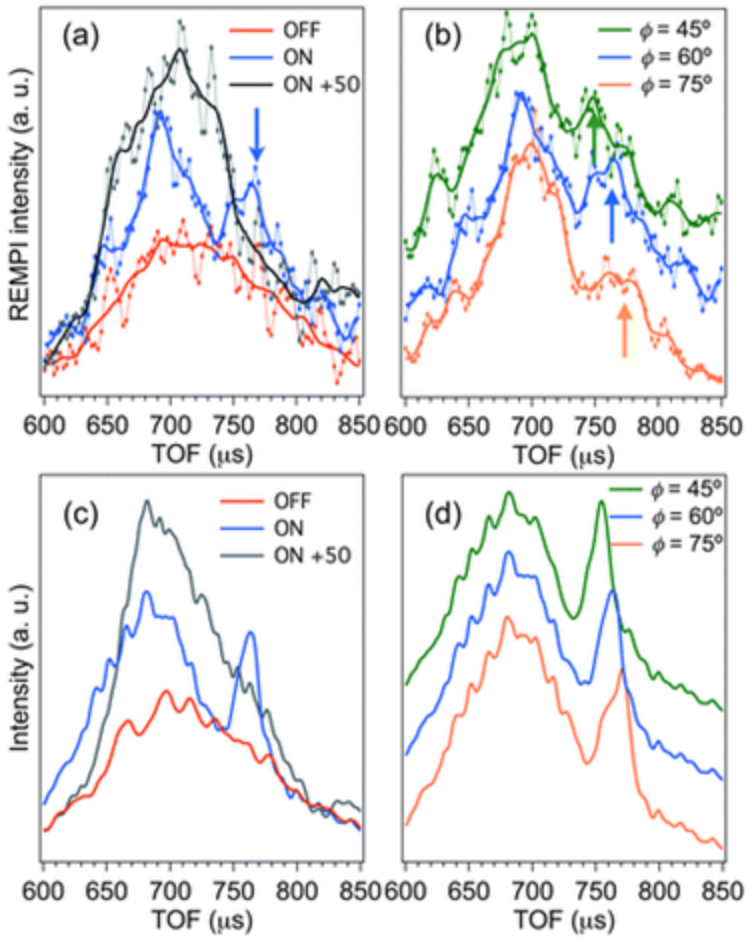

Figure 5.1 - Figure (a) is the experimental Time of Flight, TOF, signal of CH_3 with the magnetic fields off (red trace) and on (blue and grey traces). Blue trace is when the center of the free flight packet is targeted. Grey trace is when we shift the switching timing by $50\mu s$, effectively focusing the beam. Solid lines represent the smoothed data, and connected dots represent raw data. Figure (b) is experimental TOF of CH_3, with different switching phases: green, $\phi_0 = 45^\circ$; blue, $\phi_0 = 60^\circ$; and orange, $\phi_0 = 75^\circ$. The baseline of each trace is shifted for clarity. Figure (c) is simulation for (a). Figure (d) is simulation for (b).

In the deceleration experiment, blue trace of Figure 5.1 a) and c), the center of the main packet was targeted, we see a dip forming at $740\mu s$, and a decelerated peak forming at $770\mu s$. We

also see signal is enhanced for $< 740\mu s$, which correspond to the focusing of molecules that are faster than the synchronous molecule.

When we shift our coil firing sequence by $50\mu s$ to a later time, grey trace of Figure 5.1 a) and c), we effectively decelerate a region which is outside of the main packet, and hence no decelerated peak is seen. We see only the focusing effect, as the whole length of the molecular beam passes through the coil before the coil was switched off.

In the second set of experiments, the deceleration of CH_3 at different phase angle was measured, see Figure 5.1 b) and d). Phase angles, $\phi_0 = 45^\circ, 60^\circ, 75^\circ$, were used, and as expected, deceleration at higher phase angle makes decelerated peak arrival at later time, ie lower final velocity. The intensity of the decelerated peak should decrease with increasing phase angle, however, this was not observed experimentally, due to noisy experimental data.

We note that relatively high phase angle was use, $\phi_0 = 60^\circ, 75^\circ$. Such high phase angle is rarely used in deceleration experiments, because they give extremely weak signal, due to longitudinal phase stability. However, in our proof of principle experiments, our signal for the decelerated peak is still strong enough to be detectable. The reason is, there are molecules which are not longitudinally phase stable, yet they still exist at the position of the decelerated peak, due to short flight time, ie due to the short decelerator, consisting of only 15 stages. For this reason, there are no 80 coil experiments with high phase angle.

There are few remarks on the simulation results in Figure 5.1.
First, unlike the simulation for 15 coil O_2 (see Simulation notes on 15 coil Zeeman deceleration TOF), there are no longer artificial scaling factors between coilON and coilOFF in the simulation. The simulation in Figure 5.1 managed to match the experiment quite well. The reason, why simulation for CH_3 worked out better than simulation for O_2, is unknown. The simulation

result in Figure 5.1 was obtained with following assumed parameters: initial transverse velocity distribution, $\sigma_{v_{x,y}} = 7.7 m/s$, detection area $1mm \times 1mm$.

Secondly, when examined closely, we can see ripples in the TOF traces in simulation results in Figure 5.1. These ripples are an artefact from the simulation code and the way counting was done, hence the ripples are nonphysical, and we don't need to worry about them.

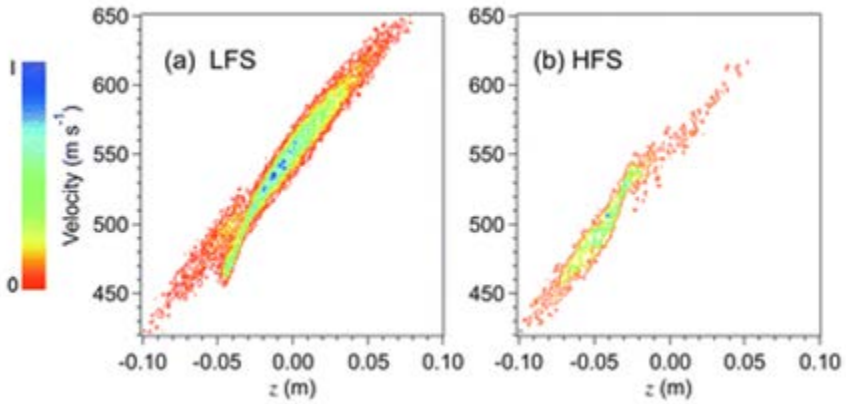

Figure 5.2 - Figure (a) is the phase space plot $\{z, v_z\}$ for the LFS state with the magnetic field switching sequence corresponding to the blue trace in Figure 5.1 (b). And Figure (b) is the phase space plot $\{z, v_z\}$ for the HFS state. Colorbar indicates the relative intensities in different regions.

Furthermore, we can plot and look at the phase space, $\{z, v_z\}$, of CH_3. Figure 5.2 shows the final snap shot in phase space, when the target molecule reaches the detection region. LFS state is $|N = 0, K = 0, M_S = \frac{1}{2}\rangle$, and HFS state is $|N = 0, K = 0, M_S = -\frac{1}{2}\rangle$.

The phase space initially is a two dimensional gaussian, the gaussian is then slanted during the deceleration process, due to the velocity difference in different parts of the distribution.

The decelerated packet can be clearly seen in LFS state, Figure 5.2 a), as the packet starts to separate from the main packet in phase space, while no such packet is present in HFS state, Figure 5.2 b), which is expected. We also see a clear focusing and defocusing effect for LFS and HFS respectively. Only molecules that are faster than the synchronous molecule will experience the focusing/defocusing force. Molecules slower than the synchronous molecule will not experience such force, because field is turned off at the synchronous molecule.

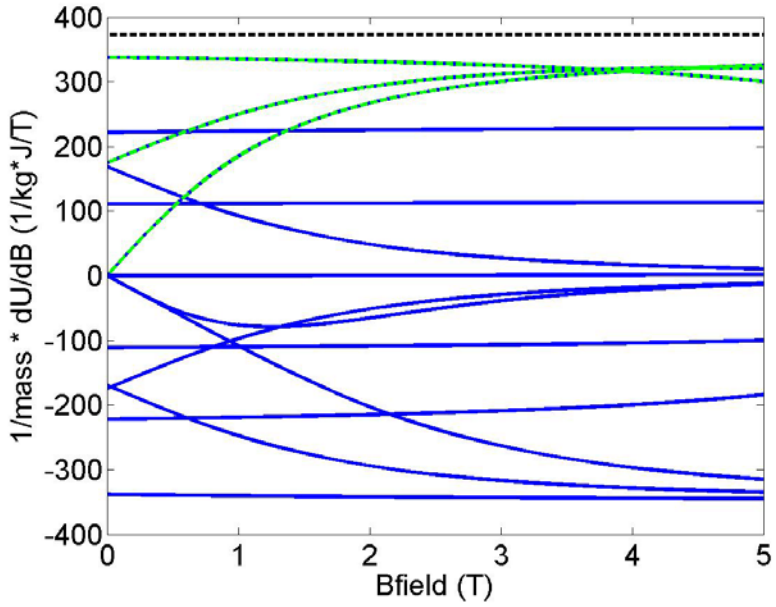

Figure 5.3 - Comparison of gradient of Zeeman shift and mass ratio of LFS states of O_2 and LFS states of CH_3. Green dotted lines are LFS states, states $|6\rangle,|8\rangle,|9\rangle$, of O_2. Black dotted lines on the top are LFS states of CH_3. Blue lines are other low lying states of O_2, for reference.

The analysis of Figure 5.1 is very similar to previous analysis on O_2. More surprisingly, even the results resemble the result of O_2, see Figure 4.1. The similarity originates from the similarity of Zeeman shift gradient, dU / dB, to mass ratio, m, between O_2 and CH_3, see Figure 5.3.

We recall from the section on principle of deceleration, the acceleration of molecule in a field is

$a_z = F_z / m = (dU / dB \times dB / dz) / m$

$\Rightarrow a_z \propto (dU / dB) / m$

Equation 5.1

Similar acceleration, a_z , or $(dU / dB) / m$, will yield similar trajectory, and hence similar TOF. We observe in Figure 5.3, $(dU / dB) / m$ for O_2 and CH_3 are quite similar in the operation range of the coil, $2T \sim 5T$. And hence, the TOF spectra were quite similar as well, compare Figure 5.1 and Figure 4.1. The similarity of $(dU / dB) / m$ between O_2 and CH_3 can justify further, why O_2 was chosen to test our system.

In summary, CH_3 behaved in an expected way in the 15 coil deceleration experiments, and this behavior is similar to O_2.

5.2 Results of 80 coils Zeeman deceleration of CH_3

Experiments on deceleration of CH_3 were done with 80 coil Zeeman decelerator, after the 80 coil O_2 experiments. CH_3 was decelerated from initial velocity $v_{init} = 480 m/s$, to final velocity $v_f = 432 m/s$, using phase angle $\phi_0 = 30^\circ$; and to $v_f = 368 m/s$ using $\phi_0 = 35^\circ$, see Figure 5.4. In terms of kinetic energy, initially we have $E_{kinetic} = \frac{1}{2} m v^2 = 2.87\text{e-}21 joules$. For $\phi_0 = 30^\circ, 35^\circ$, respectively, 19%, 41% of initial kinetic energy has been removed.

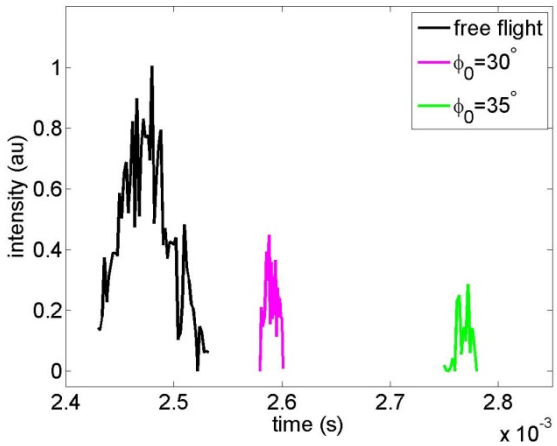

Figure 5.4 - Raw data of deceleration of CH_3 *is presented here.* 20% CH_4 in Ar *was expanded from the nozzle, backing pressure* $8bar$*, valve opening time* $65\mu s$*. Discharge conditions, discharge voltage* $-1kV$*, and discharge duration* $60-140\mu s$*. Deceleration from initial velocity of* $v_{init} = 480m/s$*, to final velocity of* $v_f = 432m/s$*, using phase angle* $\phi_0 = 30^\circ$*; and to* $v_f = 368m/s$*, using* $\phi_0 = 35^\circ$*. Target state is* $|N=0, K=0\rangle$*. Laser frequency* $69858.4cm^{-1}$*, laser power after frequency doubling is* $6.5mJ/pulse$*, number of average* 80*. Current through the coils* $600A$*, peak B-field on molecular axis* $4.2T$*.*

In Figure 5.4, the area under the peak between decelerated peaks and free flight is $\sim 20\%$ and $\sim 10\%$, for $\phi_0 = 30^\circ$ and $\phi_0 = 35^\circ$ respectively. Note that this efficiency is the combined effect of nozzle and decelerator together and not the efficicency of the decelerator alone.

The original goal was to decelerate to a velocity low enough that CH_3 can be trapped. A trappable velocity is about $\sim v_f = 30m/s$, which corresponds to a temperature $\sim 500mK$. However we were not able to achieve the goal, the most deceleration we could get was $v_f = 368m/s$. The problem is similar to 80 coil O_2 deceleration experiments. The signal rapidly decreased, as amount of deceleration was increased. In the case of CH_3, the situation is even worse than O_2, because the discharge efficiency is low, initial velocity is high, so absolute

number of molecules is low at lower velocities. Even without deceleration, the free flight of CH_3 had $\sim 10\times$ worse signal to noise ratio compared with O_2.

With deceleration, the signal to noise ratio of CH_3 approached 1:1 around $\phi_0 = 35^\circ$, $v_f = 368 m/s$. Attempts on decelerating further were not successful: the signal was lost in the noise.

At this point, we were aware that difficulty does not lie in the deceleration process, because from the analysis of 15 coil and 80 coil experiments, we saw that behavior of CH_3 was predictable, and was similar to O_2. Instead, the main difficulty in deceleration of CH_3 is to get a good and bright source of CH_3. See the next section on discharge experiments of CH_3. Without a good source of CH_3, the trapping of CH_3 will not be feasible.

5.3 Results of discharge experiments of CH_3

There are several different techniques to produce radicals from a parent species. The four main methods for creating radicals are photolysis, radio frequency (RF) discharge, direct current (DC) discharge, and chemical reactions. [78] DC discharge is technically simplest method out of the four methods.

The DC discharge method of producing radicals involves the ionization of molecules by electron impact, motions of charged particles in the electric field, and electron avalanches [79]. Consider the molecules between a -HV discharge plate, and a ground plate. The initial electrons are accelerated by the applied -ve high voltage. The electron-electron collisions create a Maxwell Boltzmann distribution, and small fraction of the electrons of the high energy tail will have high enough energy, $\sim 100eV$, to ionize atoms on impact. The ionization produces secondary electrons, and the avalanche grows. Typical timescales of avalanche formation are $1\mu s...1ms$. Electrons in the avalanche are lost due to recombination, wall collisions, and attachment to electronegative molecules. The discharge can only be sustained if the rate of production of secondary electrons exceeds this loss rate. [80]

5.3.1 CH_3 discharge experimental results

We will present the experimental results on DC discharge of methane CH_4 seeded in Ar, to produce methyl radical, CH_3. The discharge design is mainly inspired by ref [78]. The valve design is mainly inspired by ref [81]. Several different parameters where varied to obtain the strongest CH_3 signal, while keeping the rotational temperature and the beam velocity as low as possible.

The parameter space which was probed more systematically was following: For discharge, discharge current $1\mu s...400\mu s$; Discharge voltage $-500V...-1500V$. For the gas sample, concentration $10\%...50\%\ CH_4\ \text{in}\ Ar$; backing pressure $4...12bar$.

In addition, following ideas have been tried briefly: two different nozzle geometry/design; single vs multiple discharge pulses; usage of electron emitting filament near the discharge; reversing the polarity of the discharge plate. Other variable parameters in the system, which was paid less attention to: driving voltage and duration for the nozzle; Ballast resistor for the discharge.

There are a lot of variables we can vary to improve the discharge process, as shown in text above. Hence, it is impossible to map out the whole parameter space, as it will be >10 dimensional. The approach we took was, to assume none of the parameters are heavily correlated to another parameter, hence assuming each parameter can be optimized separately.

To avoid heavy correlations misleading our search for the optimum parameter set, we have to examine the landscape randomly. Then any correlation in the parameters can be treated as an error bar. For example, we assume there is no correlation between discharge voltage and the concentration. However, if there is a correlation between discharge voltage and the concentration, then to save time, we will not map out the whole landscape; we will only examine few random data points in the landscape, and then collapse all the data point into an error bar in discharge voltage or in concentration.

In practice, we found that the main difficulty the optimization is the bad signal to noise ratio, and the correlation of parameters was less of a problem in comparison. The error in the intensity of CH_3 from bad signal to noise ratio is $>10\%...20\%$. Therefore, optimization of any parameter which improved the signal by $<10\%...20\%$ will not be obvious from the data.

Next, we will present and examine our experimental DC discharge data in more detail.
All data in this section was collected using $69856cm^{-1}$, corresponding to the Q-branch of CH_3.
Data from different figures are not normalized, due to usage of different laser and beam alignment, different MCP gain, fluctuating laser power etc. Hence the comparison of plots from different figures is meaningless, and should be avoided.

5.3.2 Discharge voltage experiment and the beam velocity

The first variable parameter is the discharge voltage. Higher discharge voltage should give more signal, and it is also known that higher discharge voltage increases the initial beam velocity, and the rotational temperature [82], [81], [78].

The discharge voltage used by other group is in the range of $-700V \ldots -2000V$ [82], [79], [83], [84], [78]. We are dealing with pulsed DC discharge, and one of the limiting factor was the high voltage switch, which limited our discharge voltage to $-1500V$. In practice, for discharge voltage $< -700V$, the signal was too noisy; for $> -1000V$, the rotational temperature and beam velocity became too large.

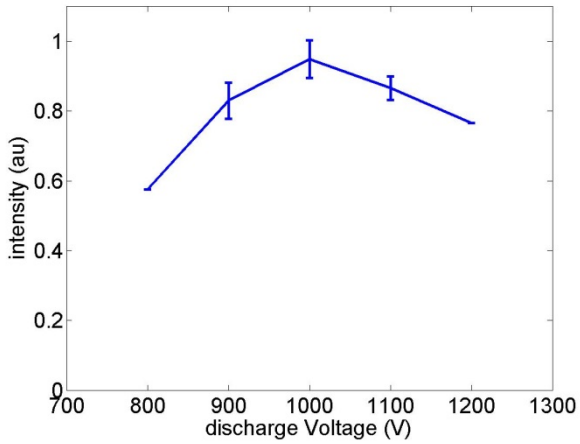

Figure 5.5 - $20\%\ CH_4$ *in* Ar*, at backing pressure* $12bar$*. Valve opening time* $55\mu s$*, valve temperature* $130K$*. Two photon energy* $69856cm^{-1}$*, laser power after frequency doubling* $6mJ\ /\ pulse$*. Discharge duration* $70 \ldots 170\mu s$*. Number of average* 20.

The intensity variation of the CH_3 signal with respect to the discharge voltage is plotted in Figure 5.5. The intensity seems to be highest at $-1000V$, the drop off at $> -1000V$ was not expected. Possible explanation is that the unexpected trend is due to random error, since the experiment at high voltages was not repeated.

We discarded using discharge voltage $> -1000V$, because in high voltage region, we observed rapid increase to initial beam velocity, see Figure 5.6, and rapid increase of rotational temperature, see next subsection about REMPI results.

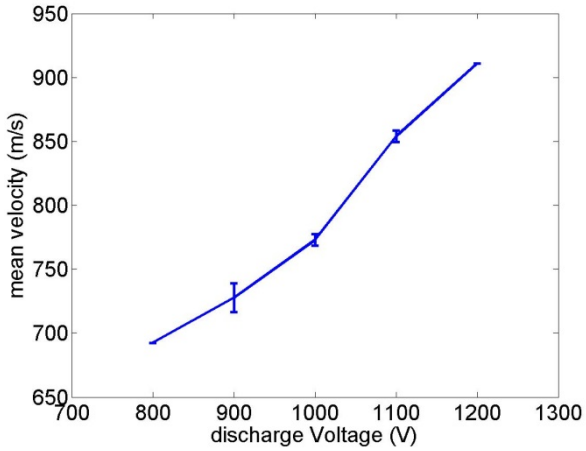

Figure 5.6 – the initial beam velocity, as a function of discharge voltage. Same data set as Figure 5.5. Higher than usual initial beam velocity, mainly due to higher backing pressure.

By increasing the discharge voltage from $-800V$ to $-1200V$, we have increased the initial translational energy of the beam, from $6.1e-21J$ to $10.1e-21J$, a 65% increase, which Is highly undesirable. Nevertheless, in the later experiments, discharge voltage of $-1kV$ was frequently used, because of signal to noise ratio was too low at $< -1kV$.

As an additional note, the electric field gradient in the discharge setup is around $\sim 10kV/cm$. Compare this value to the fields used in Stark decelerators $\sim 100kV/cm$, which are much stronger. However, there is no discharge in the Stark decelerator, because of much lower density of molecules inside the Stark decelerator vs the discharge region here.

5.3.3 Discharge duration experiment and the REMPI spectra

The duration and the starting time of the high voltage discharge is varied between $1\mu s...400\mu s$.

Starting time of the discharge can be varied to determine the mechanical delay of our nozzle, which is important. Otherwise, the starting time of the discharge is always selected to coincide with the arrival of the molecular packet in the discharge region.

Typical free flight TOF signal can be seen in Figure 5.7. The raw data is presented in Figure 5.7, to show the typical noise level of our signal, which is higher than our likings.

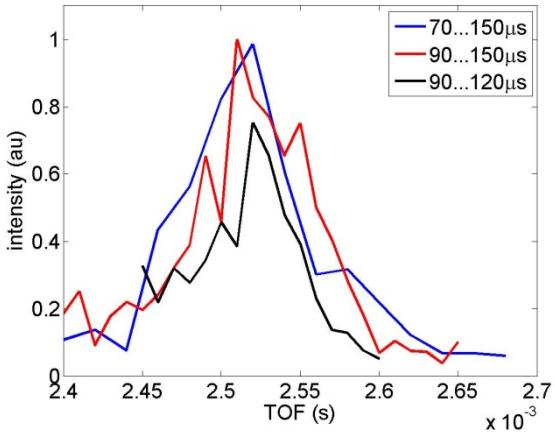

Figure 5.7 - $20\%\ CH_4$ *in* Ar*, at backing pressure* $6.5bar$*. Valve opening time* $60\mu s$*, valve temperature* $130K$*. Two photon energy* $69856cm^{-1}$*, laser power after frequency doubling* $6mJ\ /\ pulse$*. Discharge voltage* $-1kV$*. Number of average* 20*. Raw data.* $0\mu s$ *corresponds to the trigger of the nozzle.*

Discharge duration was varied in the region $1\mu s...400\mu s$. The longer discharge duration, the more increase in the rotational temperature of CH_3, similar to ref [78]. Therefore, discharge durations $>100\mu s$ were not typically used.

However, the shorter the discharge duration, the weaker the signal becomes, see Figure 5.7. The balance was found to be $30\mu s...60\mu s$

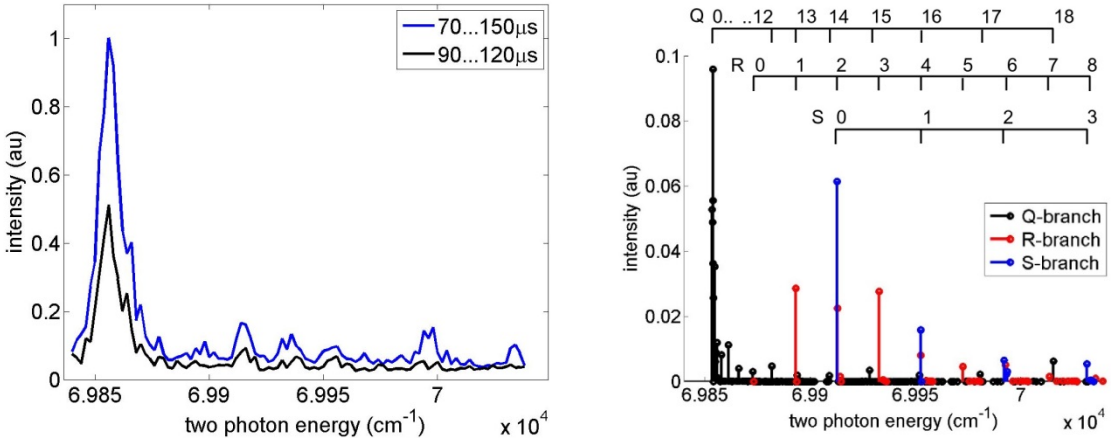

Figure 5.8 – Right figure is the REMPI simulation and assignment for CH_3, at rotational temperature $25K$. Left figure is the experimental REMPI spectra of Figure 5.7. In the left figure, rotational temperature of black trace $\sim 15K$; rotational temperature of blue trace $>15K$. Note that the intensity of Q branch relative to R and S branches is arbitrary.

The REMPI spectra, Figure 5.8, corresponding to the TOF, Figure 5.7, can be examined. We observe that shorter discharge duration have lower rotational temperature. The rotational temperature of experimental data was determined by comparing features with simulation result.

The rotational temperature of $90...120\mu s$ discharge was estimated to be $\sim 15K$, because of: for $>15K$, S2+R6 and R8+S3 peak starts to appear, which is not observed in the experiment; for $<15K$, R3 peak should disappear, but R3 was observed in the experiment.

The rotational temperature of $70...150\mu s$ discharge was estimated to be $>15K$: for S2+R6 and R8+S3 peak starts to appear, which is observed in the experiment. The upper bound for rotational temperature cannot be determined from the REMPI spectra.

The rotational temperature estimated for CH_3 is reasonable, compared with ref [82], where varieties of diatomic free radicals were produced by pulsed DC discharge, and their typical rotational temperature was $5K...50K$.

From Figure 5.8, we note that the simulation and experiment does not fully match. For example the intensity of R2 and S0 in simulation is much stronger than in the experiment. The reason is, in the simulation, Boltzmann population distribution (thermal ensemble) was assumed. And in the experiment, due to the discharge process, the population distribution is very unlikely to be Boltzmann, because there are not enough collisions in the molecular packet to thermalize the ensemble. The discrepancy between simulation and experiment confirms that, indeed after discharge, the population distribution is not Boltzmann. Strictly speaking, we cannot assign a temperature to an ensemble which doesn't obey Boltzmann's distribution, and the rotational temperature is better thought as the highest N" state which is occupied.

Interestingly, we happened to have conducted the similar discharge experiment in a smaller vacuum system, which showed lower rotational temperature, $5K...10K$ (compared with $15K$, Figure 5.8), although higher discharge voltage was used, $-1300V$ (compared to $-1kV$, Figure 5.7). All other parameters are somewhat similar. The difference is, the distance from nozzle to detection is shorter $\sim 0.4m$ (compared to $\sim 1.0m$), and the absence of Zeeman coils (compared to with coils). Currently, we hypothesize that, the decrease of rotational temperature in the shorter vacuum chamber might be due to the lack of elastic collision between the molecular beam and the Zeeman coil. Further confirmation is necessary.

5.3.4 Varying the concentration

Concentration of CH_4 in Ar can be varied. From knowledge of supersonic expansion, it is trivial that: larger concentration of CH_4 will give more signal, and will increase the initial beam velocity. We wanted to test that other parameters, such as discharge voltage and backing pressure, will not correlate to the concentration too much, and vice versa. For example, we can

imagine, by varying the concentration of CH_4 might shift a critical threshold in discharge voltage, and hence behavior might be very different.

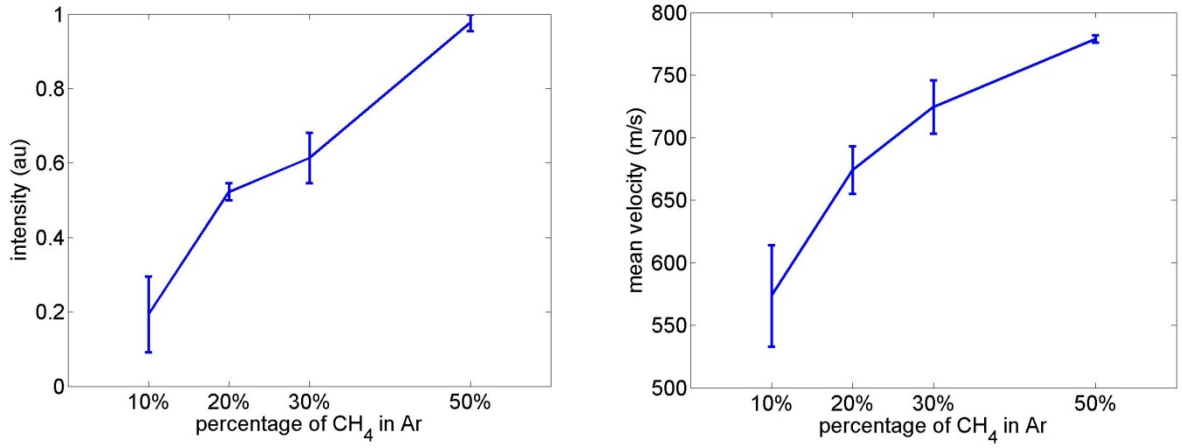

Figure 5.9 – Left figure is the intensity dependence on concentration. The right figure is the initial beam velocity dependence on concentration. Experimental conditions: backing pressure $6...12bar$ *. Valve opening time* $50\mu s$ *, valve temperature* $130K$ *. Two photon energy* $69856cm^{-1}$ *, laser power after frequency doubling* $6mJ/pulse$ *. Discharge voltage* $-0.9kV...-1.1kV$ *. Discharge duration* $130...150\mu s$

The experimental results are shown in Figure 5.9. The main contribution to the errorbar in Figure 5.9 is from backing pressure. The expected behavior was observed: increase in concentration increased the signal, and increase in concentration increased the initial beam velocity. And, the correlation to other parameters was verified to be not very strong for the parameter values we typically use.

5.3.5 Changing the design of the nozzle

Two designs of the nozzle were tested: a pinhole nozzle, and a conical nozzle [81]. And various discharge plate configuration was tested. The main difficulty was, we lacked a detailed model or simulation of the expansion and discharge process with respect to the design. Nevertheless, we still want to present the observations we made, in the texts below.

First design, see Figure 5.10, we used a pinhole, expanding into a cylindrical channel, about $\sim 3mm$ in length, and $1mm$ in diameter. Presence of channel is due to technical reasons. After the channel, there was a discharge region, which had length d, which we varied from $1.6mm$ to $7.4mm$.

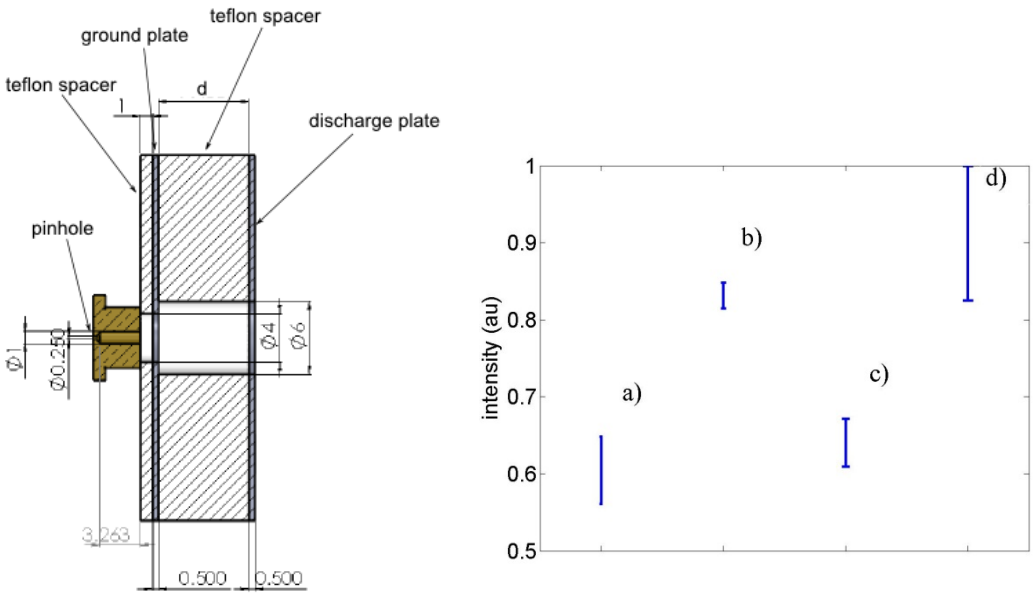

Figure 5.10 – left figure is design of the pinhole nozzle and discharge system, in which we varied the length of the discharge region, d. Right figure is the intensity we measured under various conditions for a) $d = 1.6mm$, b) $d = 2.0mm$, c) $d = 3.6mm$, d) $d = 7.4mm$

The trend in Figure 5.10 was not monotonically increasing or decreasing. A possible explanation is: the longer the discharge region is, the more time molecules will spend inside the discharge region, and hence higher probability to produce radical; on the other hand, the longer the discharge region is, the weaker the electric field gradient, since the electrode are further apart, and hence lower probability to produce radical. The trend in Figure 5.10 is probably due to the combination of these effects.

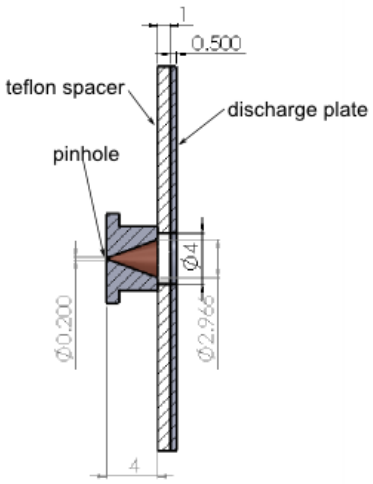

Figure 5.11 – The final configuration. The design of the conical shaped nozzle and the discharge plate, with ground plate removed.

The second design tried was with the conical shaped nozzle, see Figure 5.11. Similar discharge configuration as Figure 5.10 was tested, and found to be not as good as the configuration in Figure 5.11. The configuration in Figure 5.11 gave about $4\times$ more signal, compared with the configuration in Figure 5.10. And consequently, the configuration of Figure 5.11 was the final configuration we settled to. The reason for the increase of the signal is speculated to be: the discharge plate was moved much closer to the nozzle, with the ground plate removed, this allows the discharge to happen in a region with high density of molecules, and hence the increased number of radicals was produced.

The difference from Figure 5.10 is: 1) the shape of the nozzle; 2) the –HV discharge plate now moved much closer to the nozzle, and there is no ground plate between the –HV and nozzle. Originally, the ground plate was present to protect the nozzle from the discharge current. From our experience, apart from some carbon deposits near the nozzle, it seems there is no harm done to the nozzle by removing the protective grounded plate.

In the course of our investigation, we have also briefly tried placing a hot filament near the discharge region, in order to initiate the discharge more easily, similar to ref [78]. However, the presence of the filament showed no improvement of the signal intensity.

We have also briefly tried reversing the polarity of the discharge plate [81], instead of using $-1kV$, we would use $+1kV$, the direction of electron flow would change, and possibly increase the number of radicals produced. However, the reversing of polarity showed no improvement of the signal intensity.

5.3.6 Single vs multiple discharge pulse

Ref [79] reported that having multiple short discharge pulse instead of one long DC pulse will stabilize the discharge. The idea was interesting, and we tested briefly the effect in our system.

The result, see Figure 5.12, was surprising, and presented here for further speculation. For single discharge we used $10\mu s$ pulse at high voltage of $-1.5kV$. For multiple discharge pulse, we used three pulsed, with durations $3\mu s + 10\mu s + 3\mu s$ at high voltage of $-1.5kV$.

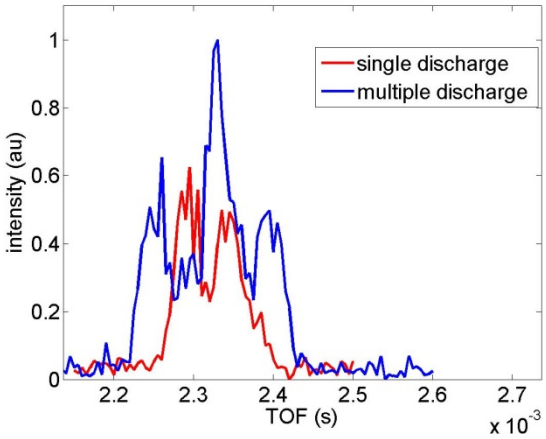

Figure 5.12 - Single pulse: $95...105\mu s$*, Multiple pulse:* $91...94\mu s, 95...105\mu s, 106...109\mu s$*. Concentration* $20\%\ CH_4$ in Ar*. Backing pressure* $9bar$*. Valve opening time* $50\mu s$*, valve*

temperature $150K$ *. Two photon energy* $69856cm^{-1}$*, laser power after frequency doubling* $4...5mJ$ / *pulse*. *Discharge voltage* $-1.5kV$.

It is interesting to note the peak structure of TOF, both in single and in multiple discharges. The peaks are formed at the switch on/off timing of the discharge voltage, which may be caused by the fly back voltage of the high voltage switch. Also, the signal intensity of multiple discharges is $2\times$ more than the single discharge pulse. Furthermore, the signal intensity from multiple discharges in Figure 5.12 is $>5\times$ larger than the signal intensity of what we typically use, see Figure 5.7. The $>5\times$ increase in signal is due to using high voltages, together with multiple discharges.

However, the rotational temperature and the initial beam velocity were not measured. Also, multiple discharges at lower voltage was not tested. Hence further measurement and analysis is needed to determine the usefulness of the method of multiple discharge pulses.

5.3.7 Additional notes

Firstly, the experimental TOF data presented in this section was collected using Q-branch transition of CH_3, because Q-branch is the most intense transition. We have also tried and centered our frequency on R1 and S0 transitions, in hope to see a stronger signal, because R1 and S0 peaks only contain the LFS states we decelerate. Unfortunately, using R1 or S0 decreased the signal intensity.

We also tried to use REMPI detection through the $3p_z\,^2A_2''$, instead of $4p_z\,^2A_2''$ level [15]. Unfortunately, $3p_z\,^2A_2''$ decreased the signal intensity.

Secondly, the efficiency of the discharge was not determined experimentally, the discharge efficiency was estimated to be $\sim 1\%$ at most. The estimation was made, by roughly looking at the absolute signal intensity of the free flight CH_3 vs O_2, after normalizing for MCP gain and

backing pressure. The estimation is also consistent with ref [81], in ref [81], they used for the dielectric barrier DC discharge, which is advertised to be more efficient than our DC discharge configuration. And yet, in ref [81] the discharge efficiency was determined to be $1\%...2\%$.

Thirdly, Ref [82] reported in their DC discharge experiments, although the rotational temperature of the diatomic radicals was low $5K...50K$, but the vibrational temperature was high, several thousand kelvins. This might be a concern for the production of CH_3 radical, since so far, we have not investigated the vibrational temperature of CH_3 . Further investigations are required on vibrational temperature.

5.3.8 Summary of discharge experiment of CH_3

In summary, the strongest CH_3 signal, while keeping the rotational temperature and the beam velocity as low as possible, was obtained using the following configuration and parameter values: pinhole diameter $0.2mm$, which expands into diameter $4mm$ opening in a cone shape, at angle 40° . The discharge plate is placed $1mm$ away from the nozzle, using a teflon spacer.

The nozzle is grounded, and a typical discharge voltage of $-700V...-1000V$ is applied to the discharge plate. The discharge duration is typically $30...60\mu s$ targeted at the middle of the packet. For the sample, $15\%...30\%$ CH_4 in Ar was used, with backing pressure of $6...9bar$.

==========

"Do not under estimate [how] miracles [are achieved]" -Monkey D Luffy, One piece

==========

Chapter 6: Conclusion

We have constructed the Zeeman decelerator experimental setup, and successfully reproduced the result for the deceleration of O_2 [31]. We can argue that there is slight improvement on the deceleration of O_2 over ref [31], we have achieved a slower final velocity of $52m/s$, compared to ref [31], which reached the final velocity of $83m/s$.

REMPI simulation and analysis was carried out on O_2, which gave more insight on the deceleration process. Especially for the shorter Zeeman decelerator (15 coils), for which the analysis of REMPI is more complex, because of present of non low field seeking states. Our work on REMPI of O_2 was carried out in parallel to the work of ref [1].

We have succeeded in the deceleration of a polyatomic radical, CH_3, from initial velocity of $480m/s$ to a final velocity of $368m/s$, corresponding to a removal of 41.2% of the initial translational energy. We have shown that the deceleration process of the radical can be well reproduced using simulations, and is similar to deceleration of non-radical species. And the limiting factor of further deceleration is the signal to noise ratio.

6.1 How to improve

The ultimate goal is to slow and trap radical species. A trappable final velocity is around $<50m/s$. In order to get final velocity of $<50m/s$, it is necessary to improve the signal to noise ratio of the decelerated radical beam. The signal to noise ratio can be improved, by improving either the source, deceleration process, or the detection.

The source can be improved by investigating different nozzle skimmer configurations, and/or by improving the discharge efficiency. In this thesis, we have presented the results of DC discharge. However, there are other methods to produce CH_3 radical, which need to be investigated. These methods are, for example, RF discharge, dielectric barrier discharge [81], photodissociation [13], DC discharge before nozzle expansion etc.

The deceleration process can be improved by changing into the moving trap decelerator, which has been demonstrated by ref [33] to be generally superior to the conventional Zeeman decelerator (this thesis). If reconstructing the whole setup is to be avoided, then there might be room for improvement by improving the switching sequence of the coils, either by analysis of the dynamics of the beam [42] [19], or by optimization using genetic algorithm [85] [86], see Appendix B about genetic algorithm.

The detection can be improved by investigating different possible transitions, and/or investigating different spectroscopical methods, see introduction Section 1.2 about methyl radicals.

One limitation is that detection method has to be resolved in time, on the order of $<1\mu s$, which corresponds to the width of the decelerated packet. The time resolution issue is the reason why residual gas analyzer (RGA) was attempted but not used in the end for our experiments. However, if we combine REMPI (time resolution) with RGA (might have better sensitivity), we might have better chance in seeing slower packets of decelerated radical beam. Another limitation is that detection method has to resolve rotational states, which is another reason why REMPI was used. However we can relax this limitation with some caution [87], because the deceleration process itself is somewhat state selective. Once we relax the limitation of state selectivity on the detection, then we have much wider range of method fordetection that we can potentially use.

Bibliography

[1] A. Wiederkehr, H. Schmutz, M. Motsch, and F. Merkt, “Velocity-tunable slow beams of cold o2 in a single spin-rovibronic state with full angular-momentum orientation by multistage zeeman deceleration,” *Molecular Physics*, vol. 110, no. 15-16, pp. 1807–1814, 2012.

[2] I. W. M. Smith, *LOW TEMPERATURES AND COLD MOLECULES Low temperatures and cold molecules*. Imperial College Press, 2008.

[3] B. F. R Krems, W Stwalley, *Cold Molecules Theory, Experiment, Applications*. CRC Press, 2009.

[4] L. D. Carr, D. DeMille, R. V. Krems, and J. Ye, *Cold and ultracold molecules: science, technology and applications*, vol. 11. New J. Phys 11 055049, 2009.

[5] M. T. Bell and T. P. Softley, *Ultracold molecules and ultracold chemistry*, vol. 107. ., 2009.

[6] S. Y. T. van de Meerakker, H. L. Bethlem, N. Vanhaecke, and G. Meijer, *Manipulation and Control of Molecular Beams*, vol. 112. ., 2012.

[7] R. V. Krems, “Cold controlled chemistry,” *Phys. Chem. Chem. Phys.*, vol. 10, pp. 4079–4092, 2008.

[8] P. Kelly and S. G. Westre, “Resonance raman spectroscopy of the methyl radical,” *Chemical Physics Letters*, vol. 151, no. 3, pp. 253 – 257, 1988.

[9] A. W. Jasper, S. J. Klippenstein, L. B. Harding, and B. Ruscic, “Kinetics of the reaction of methyl radical with hydroxyl radical and methanol decomposition・” *The Journal of Physical Chemistry A*, vol. 111, no. 19, pp. 3932–3950, 2007. PMID: 17388366.

[10] T. Momose, Y. Liu, S. Zhou, P. Djuricanin, and D. Carty, “Manipulation of translational motion of methyl radicals by pulsed magnetic fields,” *Phys. Chem. Chem. Phys.*, vol. 15, pp. 1772–1777, 2013.

[11] S. H. Wilson, J. D. Howe, K. N. Rosser, M. N. Ashfold, and R. N. Dixon, “A reinvestigation of the near-ultraviolet photodissociation dynamics of the methyl radical,” *Chemical Physics Letters*, vol. 227, no. 4・, pp. 456 – 460, 1994.

[12] D. R. Alfonso and S. E. Ulloa, “Molecular-dynamics simulations of methyl-radical deposition on diamond (100) surfaces,” *Phys. Rev. B*, vol. 48, pp. 12235–12239, Oct 1993.

[13] G. Herzberg, “The bakerian lecture. the spectra and structures of free methyl and free methylene,” *Proceedings of the Royal Society of London. Series A, Mathematical and Physical Sciences*, vol. 262, no. 1310, pp. pp. 291–317, 1961.

[14] C. Yamada, E. Hirota, and K. Kawaguchi, “Diode laser study of the nu [sub 2] band of the methyl radical,” *The Journal of Chemical Physics*, vol. 75, no. 11, pp. 5256–5264, 1981.

[15] J. W. Hudgens, T. G. DiGiuseppe, and M. C. Lin, “Two photon resonance enhanced multiphoton ionization spectroscopy and state assignments of the methyl radical,” *The Journal of Chemical Physics*, vol. 79, no. 2, pp. 571–582, 1983.

[16] P. Zalicki, Y. Ma, R. Zare, E. Wahl, J. Dadamio, T. Owano, and C. Kruger, “Methyl radical measurement by cavity ring-down spectroscopy,” *Chemical Physics Letters*, vol. 234, no. 4・, pp. 269 – 274, 1995.

[17] H. L. Bethlem, G. Berden, A. J. A. van Roij, F. M. H. Crompvoets, and G. Meijer, “Trapping neutral molecules in a traveling potential well,” *Phys. Rev. Lett.*, vol. 84, pp. 5744–5747, Jun 2000.

[18] H. L. Bethlem, F. M. H. Crompvoets, R. T. Jongma, S. Y. T. van de Meerakker, and G. Meijer, “Deceleration and trapping of ammonia using time-varying electric fields,” *Phys. Rev. A*, vol. 65, p. 053416, May 2002.

[19] L. Scharfenberg, H. Haak, G. Meijer, and S. Y. T. van de Meerakker, “Operation of a stark decelerator with optimum acceptance,” *Phys. Rev. A*, vol. 79, p. 023410, Feb 2009.

[20] L. P. Parazzoli, N. Fitch, D. S. Lobser, and H. J. Lewandowski, “High-energy-resolution molecular beams for cold collision studies,” *New Journal of Physics*, vol. 11, no. 5, p. 055031, 2009.

[21] H. L. Bethlem, A. J. A. van Roij, R. T. Jongma, and G. Meijer, “Alternate gradient focusing and deceleration of a molecular beam,” *Phys. Rev. Lett.*, vol. 88, p. 133003, Mar 2002.

[22] R. Fulton, A. I. Bishop, and P. F. Barker, “Optical stark decelerator for molecules,” *Phys. Rev. Lett.*, vol. 93, p. 243004, Dec 2004.

[23] S. A. Meek, H. L. Bethlem, H. Conrad, and G. Meijer, “Trapping molecules on a chip in traveling potential wells,” *Phys. Rev. Lett.*, vol. 100, p. 153003, Apr 2008.

[24] A. Marian, H. Haak, P. Geng, and G. Meijer, “Slowing polar molecules using a wire stark decelerator,” *The European Physical Journal D*, vol. 59, no. 2, pp. 179–181, 2010.

[25] A. Osterwalder, S. A. Meek, G. Hammer, H. Haak, and G. Meijer, “Deceleration of neutral molecules in macroscopic traveling traps,” *Phys. Rev. A*, vol. 81, p. 051401, May 2010.

[26] S. D. Hogan, D. Sprecher, M. Andrist, N. Vanhaecke, and F. Merkt, “Zeeman deceleration of h and d,” *Phys. Rev. A*, vol. 76, p. 023412, Aug 2007.

[27] E. Narevicius, C. G. Parthey, A. Libson, J. Narevicius, I. Chavez, U. Even, and M. G. Raizen, “An atomic coilgun: using pulsed magnetic fields to slow a supersonic beam,” *New Journal of Physics*, vol. 9, no. 10, p. 358, 2007.

[28] S. D. Hogan, A. W. Wiederkehr, M. Andrist, H. Schmutz, and F. Merkt, “Slow beams of atomic hydrogen by multistage zeeman deceleration,” *Journal of Physics B: Atomic, Molecular and Optical Physics*, vol. 41, no. 8, p. 081005, 2008.

[29] S. D. Hogan, A. W. Wiederkehr, H. Schmutz, and F. Merkt, “Magnetic trapping of hydrogen after multistage zeeman deceleration,” *Phys. Rev. Lett.*, vol. 101, p. 143001, Sep 2008.

[30] A. W. Wiederkehr, M. Motsch, S. D. Hogan, M. Andrist, H. Schmutz, B. Lambillotte, J. A. Agner, and F. Merkt, “Multistage zeeman deceleration of metastable neon,” *The Journal of Chemical Physics*, vol. 135, no. 21, p. 214202, 2011.

[31] E. Narevicius, A. Libson, C. G. Parthey, I. Chavez, J. Narevicius, U. Even, and M. G. Raizen, “Stopping supersonic oxygen with a series of pulsed electromagnetic coils: A molecular coilgun,” *Phys. Rev. A*, vol. 77, p. 051401, May 2008.

[32] E. Lavert-Ofir, L. David, A. B. Henson, S. Gersten, J. Narevicius, and E. Narevicius, “Stopping paramagnetic supersonic beams: the advantage of a co-moving magnetic trap decelerator,” *Phys. Chem. Chem. Phys.*, vol. 13, pp. 18948–18953, 2011.

[33] E. Lavert-Ofir, S. Gersten, A. B. Henson, I. Shani, L. David, J. Narevicius, and E. Narevicius, “A moving magnetic trap decelerator: a new source of cold atoms and molecules,” *New Journal of Physics*, vol. 13, no. 10, p. 103030, 2011.

[34] A. Trimeche, M. Bera, J.-P. Cromi 鑽 es, J. Robert, and N. Vanhaecke, “Trapping of a supersonic beam in a traveling magnetic wave,” *The European Physical Journal D*, vol. 65, no. 1-2, pp. 263–271, 2011.

[35] S. D. Hogan, M. Motsch, and F. Merkt, “Deceleration of supersonic beams using inhomogeneous electric and magnetic fields,” *Phys. Chem. Chem. Phys.*, vol. 13, pp. 18705–18723, 2011.

[36] S. D. Hogan, C. Seiler, and F. Merkt, “Rydberg-state-enabled deceleration and trapping of cold molecules,” *Phys. Rev. Lett.*, vol. 103, p. 123001, Sep 2009.

[37] S. Merz, N. Vanhaecke, W. Jäger, M. Schnell, and G. Meijer, “Decelerating molecules with microwave fields,” *Phys. Rev. A*, vol. 85, p. 063411, Jun 2012.

[38] D. A. McQuarrie and J. D. Simon, *Physical Chemistry: A Molecular Approach*. University Science Books, 1997.

[39] M. D. Morse, “Supersonic beam sources,” *Experimental Methods in the physical sciences*, vol. 29B, 1996.

[40] I. M. A. Al-Qadi, *THREE-DIMENSIONAL NUMERICAL SIMULATION OF A SUPERSONIC UNDER-EXPANDED RECTANGULAR JET*. PhD thesis, The Ohio State University, 2003.

[41] G. Scoles, *Atomic and Molecular Beam Methods: Volume 1*. Oxford University Press, 1971.

[42] A. W. Wiederkehr, S. D. Hogan, and F. Merkt, “Phase stability in a multistage zeeman decelerator,” *Phys. Rev. A*, vol. 82, p. 043428, Oct 2010.

[43] S. van de Meerakker, *Deceleration and Electrostatic Trapping of OH Radicals*. PhD thesis, Fritz-Haber-Institut der Max-Planck-Gesellschaft, 2006.

[44] A. Wiederkehr, *Multistage Zeeman deceleration of atoms and molecules*. PhD thesis, ETH, 2012.

[45] W. G. Kaenders, F. Lison, I. Müller, A. Richter, R. Wynands, and D. Meschede, “Refractive components for magnetic atom optics,” *Phys. Rev. A*, vol. 54, pp. 5067–5075, Dec 1996.

[46] N. Konenkov, M. Sudakov, and D. Douglas, “Matrix methods for the calculation of stability diagrams in quadrupole mass spectrometry,” *Journal of the American Society for Mass Spectrometry*, vol. 13, no. 6, pp. 597 – 613, 2002.

[47] S. Y. T. van de Meerakker, N. Vanhaecke, H. L. Bethlem, and G. Meijer, “Transverse stability in a stark decelerator,” *Phys. Rev. A*, vol. 73, p. 023401, Feb 2006.

[48] J. F. Black and I. Powis, “Rotational structure and predissociation dynamics of the methyl 4p[sub z](v=0) rydberg state investigated by resonance enhanced multiphoton ionization spectroscopy,” *The Journal of Chemical Physics*, vol. 89, no. 7, pp. 3986–3992, 1988.

[49] B. M. Haya, I. Zapater, P. Quintana, M. Men 駭 dez, E. Verdasco, J. Santamaria, L. Ba res, and F. Aoiz, “Photodissociation of dimethyl sulfide at 227.5 nm: resonance-enhanced multiphoton ionization of the methyl fragment,” *Chemical Physics Letters*, vol. 311, no. 3・, pp. 159 – 166, 1999.

[50] K. m. Chen and E. S. Yeung, “Rovibronic two photon transitions of symmetric top molecules,” *The Journal of Chemical Physics*, vol. 69, no. 1, pp. 43–52, 1978.

[51] webqc.org, “Point group symmetry character tables,” 2013.

[52] M. Houde, “The symmetry of rovibronic wave functions,” 2011.

[53] H. J. W ner, “Spectroscopy fs13,” 2013.

[54] P. R. Bunker, *Molecular Symmetry and Spectroscopy*. Academic Press, 1979.

[55] S. Davis, D. T. Anderson, G. Duxbury, and D. J. Nesbitt, “Jet-cooled molecular radicals in slit supersonic discharges: Sub-doppler infrared studies of methyl radical,” *The Journal of Chemical Physics*, vol. 107, no. 15, pp. 5661–5675, 1997.

[56] K.-m. Chen, “Rotational line strengths of the v2-active two-photon transitions of the methyl radical,” *The Journal of Chemical Physics*, vol. 119, no. 14, pp. 7163–7167, 2003.

[57] I. C. Bowater, J. M. Brown, and A. Carrington, “Microwave spectroscopy of nonlinear free radicals. i. general theory and application to the zeeman effect in hco,” *Proceedings of the Royal Society of London. A. Mathematical and Physical Sciences*, vol. 333, no. 1594, pp. 265–288, 1973.

[58] J. M. Brown and A. Carrington, *Rotational Spectroscopy of Diatomic Molecules*. Cambridge University Press, 2003.

[59] S. Katsumata, K. Sato, Y. Achiba, and K. Kimura, “Excited-state photoelectron spectra of the one-photon forbidden {C3IIg} rydberg state of molecular oxygen,” *Journal of Electron Spectroscopy and Related Phenomena*, vol. 41, no. 2, pp. 325 – 335, 1986.

[60] J. T. Hougen, “The calculation of rotational energy levels and rotational line intensities in diatomic molecules,” *NBS Monograph 115*, 1970.

[61] R. N. Zare, *Angular Momentum: Understanding Spatial Aspects in Chemistry and Physics*. Wiley-Interscience, 1991.

[62] M. Inguscio, “Majorana spin-flip and ultra-low temperature atomic physics,” *PoS*, vol. EMC2006, p. 008, 2006.

[63] C. V. Sukumar and D. M. Brink, “Spin-flip transitions in a magnetic trap,” *Phys. Rev. A*, vol. 56, pp. 2451–2454, Sep 1997.

[64] E. Nikitin, E. Dashevskaya, J. Alnis, M. Auzinsh, E. R. I. Abraham, B. R. Furneaux, M. Keil, C. McRaven, N. Shafer-Ray, and R. Waskowsky, “Measurement and prediction of the speed-dependent throughput of a magnetic octupole velocity filter including nonadiabatic effects,” *Phys. Rev. A*, vol. 68, p. 023403, Aug 2003.

[65] K. Halbach and R. F. Holsinger, “Superfish - a computer program for evaluation of rf cavities with cylindrical symmetry,” *Part. Accel.*, vol. 7, pp. 213–222. 29 p, Jun 1976.

[66] L. A. A. C. Group, “Poisson superfish,” 2012.

[67] C. G. Parthey, *Pulsed Magnetic Slowing of Supersonic Beams*. PhD thesis, The University of Texas at Austin, 2007.

[68] wikipedia, “Permeability,” 2013.

[69] northropgrumman, “Product > speciality crystal > tgg,” 2011.

[70] Varian, “Varian agilent,” 2013.

[71] V. Inc, “Vacuum technology seminar,” 2012.

[72] Parker, “Home > products > miniature-micro-dispensing valves > series 99 - miniature high speed and pressure dispense valve,” 2013.

[73] D. Irimia, D. Dobrikov, R. Kortekaas, H. Voet, D. A. van den Ende, W. A. Groen, and M. H. M. Janssen, “A short pulse (7?us fwhm) and high repetition rate (dc-5khz) cantilever piezovalve for pulsed atomic and molecular beams,” *Review of Scientific Instruments*, vol. 80, no. 11, pp. –, 2009.

[74] Even and Lavie, “Even lavie valve,” 2013.

[75] A. T. J. B. Eppink and D. H. Parker, “Velocity map imaging of ions and electrons using electrostatic lenses: Application in photoelectron and photofragment ion imaging of molecular oxygen,” *Review of Scientific Instruments*, vol. 68, no. 9, pp. 3477–3484, 1997.

[76] wikipedia, “Microchannel_plate_detector,” 2013.

[77] D. M. Ventures, “Del mar ventures> product list> mcp products,” 2013.

[78] H. Lewandowski, E. R. Hudson, J. Bochinski, and J. Ye, “A pulsed, low-temperature beam of supersonically cooled free radical {OH} molecules,” *Chemical Physics Letters*, vol. 395, no. 1・, pp. 53 – 57, 2004.

[79] M. N. Bera, *Zeeman Deceleration of Supersonic Beam trapping of Paramagnetic Atoms in a Traveling Magnetic Wave*. PhD thesis, LAC - Laboratoire Aim・Cotton, 2011.

[80] D. M. Egorov, *Buffer-Gas Cooling of Diatomic Molecules*. PhD thesis, Harvard University, 2004.

[81] K. Luria, N. Lavie, and U. Even, “Dielectric barrier discharge source for supersonic beams,” *Review of Scientific Instruments*, vol. 80, no. 10, pp. –, 2009.

[82] R. Schlachta, G. Lask, S. Tsay, and V. Bondybey, “Pulsed discharge source of supersonically cooled transient species,” *Chemical Physics*, vol. 155, no. 2, pp. 267 – 274, 1991.

[83] Z. Ren, M. Qiu, L. Che, D. Dai, X. Wang, and X. Yang, “A double-stage pulsed discharge fluorine atom beam source,” *Review of Scientific Instruments*, vol. 77, no. 1, pp. –, 2006.

[84] I.-C. Lu, W.-J. Huang, C. Chaudhuri, W.-K. Chen, and S.-H. Lee, “Development of a stable source of atomic oxygen with a pulsed high-voltage discharge and its application to crossed-beam reactions,” *Review of Scientific Instruments*, vol. 78, no. 8, pp. –, 2007.

[85] J. J. Gilijamse, J. Küpper, S. Hoekstra, N. Vanhaecke, S. Y. T. van de Meerakker, and G. Meijer, “Optimizing the stark-decelerator beamline for the trapping of cold molecules using evolutionary strategies,” *Phys. Rev. A*, vol. 73, p. 063410, Jun 2006.

[86] Y. Salathe, *Optimizing zeeman deceleration of atomic Hydrogen by evolutionary algorithms*. PhD thesis, ETH Zurich, 2009.

[87] N. Fitch, D. Esteves, M. Fabrikant, T. Briles, Y. Shyur, L. Parazzoli, and H. Lewandowski, “State purity of decelerated molecular beams,” *Journal of Molecular Spectroscopy*, vol. 278, no. 0, pp. 1 – 6, 2012.

[88] M. Keijzer, J. Merelo, G. Romero, and M. Schoenauer, “Evolving objects: A general purpose evolutionary computation library,” in *Artificial Evolution* (P. Collet, C. Fonlupt, J.-K. Hao, E. Lutton, and M. Schoenauer, eds.), vol. 2310 of *Lecture Notes in Computer Science*, pp. 231–242, Springer Berlin Heidelberg, 2002.

[89] Wikipedia, “Three-valued logic.”

[90] J. West, “The quantum computer,” 2000.

[91] P. Shor, “Algorithms for quantum computation: discrete logarithms and factoring,” in *Foundations of Computer Science, 1994 Proceedings., 35th Annual Symposium on*, pp. 124–134, 1994.

[92] D. Deutsch, “Lectures on quantum computation.”

[93] D. DeMille, “Quantum computation with trapped polar molecules,” *Phys. Rev. Lett.*, vol. 88, p. 067901, Jan 2002.

[94] S. Zhou.

Appendices

Appendix A The 2nd generation decelerator

At the beginning of the project, we have constructed a 15 coil Zeeman decelerator (aka 1st generation, not discussed in the thesis). After the 1st generation, and before building the 80 coil Zeeman decelerator which is described in the thesis (aka 3rd generation), we have constructed a 2nd generation Zeeman decelerator, which didn't quite work due to technical reasons. Here is a description of it.

For the 2nd generation decelerator, we have tried to move the coils outside the vacuum chamber. The main motivation being, replacing burned coils (which happened somewhat often) is troublesome, if the coils are inside the vacuum. Because of opening and closing chamber, pumping, alignment, accessibility etc.

And if we only enclose the beam line in the vacuum, and put the coils outside the vacuum chamber, then many of the problems will disappear. The design idea was taken from ref [30], in which they showed the viability of putting coils outside the vacuum chamber.

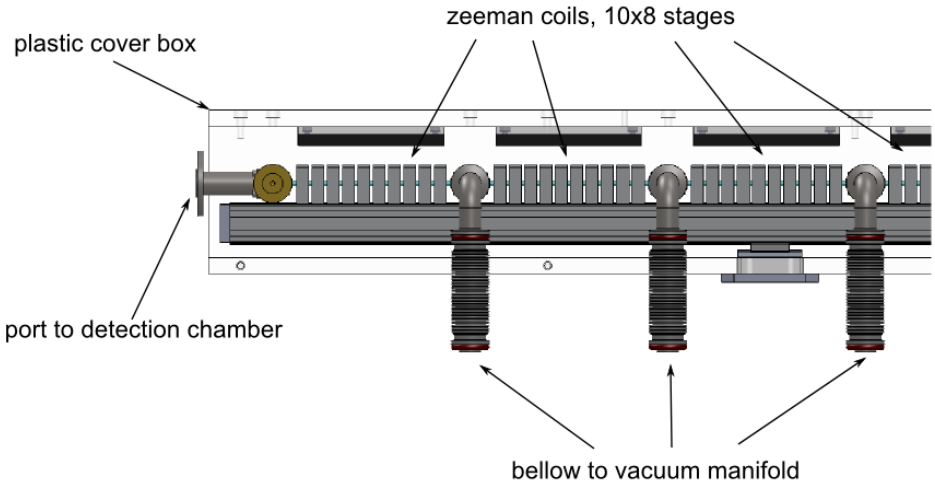

Figure 6.1 – drawing of the 2nd generation Zeeman decelerator. Every 10 stages, there is a tower, which is connected to the turbo pumps through a vacuum manifold. The plastic cover was to hold nitrogen gas to prevent condensation of water when the coils are cooling down the liquid nitrogen temperature.

One concern of if the magnetic field was strong enough in the beam line, since there is a tube, which holds the vacuum, between the coil and the beamline. In the end, simulation showed the loss of B-field strength is minimal, and hence no need to worry.

Figure 6.2 – Picture of 2nd generation Zeeman decelerator. We have actually built it, and it looks pretty.

The main problem, which eventually made us to change the design was following. We need to hold the vacuum for the beamline inside the coils. We do this by using a quartz tube and O-ring seals. The alignment of the coils was done using the optical rail beneath of the coils, which should be sufficient. However, we failed to realize that each coil is slightly different (due to construction stage), so even if the bottom of the coils are perfectly alignment, it doesn't mean the center of the coils are perfectly aligned. The slightly misalignment is not obvious visually, but it was obvious when we tried to put quartz tube in the middle, and clamp everything down, because quartz tube cracked under stress, due to slight misalignment. And there is no easy technical solution to the alignment problem at that time.

Next, we tried to use kapton coated bronze tubes, instead of quartz. Bronze is a metal, hence malleable to some extent. However, the problem with bronze tubing was, despite the kapton coating, the coil was shorting to the bronze tubing, burning a hole, and destroying the vacuum, with possibilities of damaging the turbo pumps. And in the end, we decided to give up on this design due to all the techniqueal difficulties involved.

Note that the same problem was not present in ref [30], because they have built the coil directly on the quartz tube. As opposed to us, where we build the coils first, and then try to fit a quartz tube inside.

Appendix B Genetic algorithm

A genetic algorithm (GA) is a method for solving both constrained and unconstrained optimization problems based on a natural selection process that mimics biological evolution. The algorithm repeatedly modifies a population of individual solutions. At each step, the genetic algorithm randomly selects individuals from the current population and uses them as parents to produce the children for the next generation. Over successive generations, the population "evolves" toward an optimal solution.

Idea of evolutionary computing was introduced in the 1960s by I. Rechenberg in his work "Evolution strategies" (Evolutionsstrategie in original). His idea was then developed by other researchers. Genetic Algorithms (GAs) were invented by John Holland and developed by him and his students and colleagues. This lead to Holland's book "Adaption in Natural and Artificial Systems" published in 1975.

In 1992 John Koza has used genetic algorithm to evolve programs to perform certain tasks. He called his method "genetic programming" (GP). LISP programs were used, because programs in this language can be expressed in the form of a "parse tree", which is the object the GA works on.

Here, I want to present what other people have accomplished using GA on the decelerator experiments and simulations. I will present two papers: Optimizing the Stark-decelerator beamline for the trapping of cold molecules using evolutionary strategies [85], and Optimizing Zeeman deceleration of atomic hydrogen by evolutionary algorithms [86]

B.1 Paper1: Optimizing the Stark-decelerator beamline for the trapping of cold molecules using evolutionary strategies

In this paper by Gilijamse et al [85], neutral polar molecules were decelerated using Stark decelerator. The efficiency of the decelerator and trap-loading process critically depends on the exact timings of the switching of Stark electrodes. There are 100 Stark electrodes that need to

be controlled individually, but in a synchronous manner. This is effectively a 100 dimensional space, and they are trying to find the optimal solution, the timing sequence that yields the slowest molecular beam, and highest phase space density. A manual optimization of this timing sequence is practically impossible, due to the large dimensionality of this parameter space. Hence in this paper, they wanted to implement Evolutionary algorithm, in order to automatically optimize the switching sequence. The result yielded an increase of 40% of the number of trapped OH radicals.

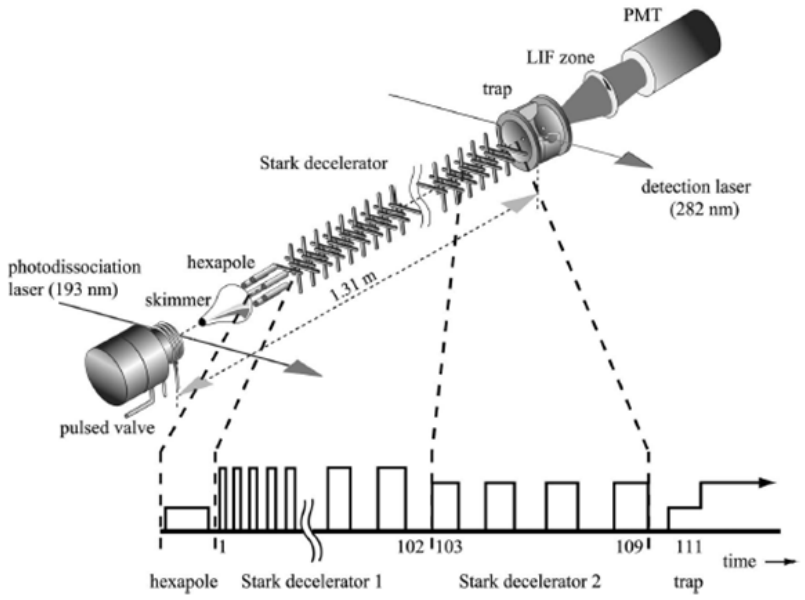

Figure 6.3 - The decelerator itself consist of, first 101 stages, which they referred to as decelerator 1. And after decelerator1, there are seven stages of Stark decelerator, referred to as decelerator2, which electronically and mechanically decoupled from decelerator1. Plus the trap after that. [85]

LIF signal of OH radicals density in the trap was used as objective (fitness) function. Method used was the Evolving Objects (EO) framework implementation of the Evolutionary algorithm. [88]

The key procedure in their EA is that they have reduced the high dimensionality (100 dimensions) of the parameter space into a relatively low dimensional space. This was done by encoding switching sequence of all electrodes with three reduced sets of parameters. And each electrode was not optimized independently. The encoding scheme was to encode all 100 electrodes into two sets of polynomial expansion coefficients. The order of the polynomial is around 20, this is required to describe the timing with sufficient accuracy of $5\mu s$. This encoding reduces the dimensionality of the problem from 100 dimensions to 20 dimensions.

To further reduce the dimensionality of the problem, they have only encoded and optimized the differences between the calculated time sequences to the optimized timing sequence $t_i - t_{i,0}$. And they have found that 2nd order polynomial be sufficient to describe this difference for the first 103 stages, and 1st order polynomial to describe the difference for stages 103-106. For the last five deceleration stages, and the trap-loading and trapping configurations, which are the most critical timings, these were optimized individually, resulting in a 10 dimensional parameter space.

$$t_i = t_{i,0} + \sum_{j=0}^{o_1} p_{j+1}(i-1)^j,$$

Equation 6.1 - The polynomial coefficients that was optimized was p, t_i,0 was the theoretical timing.

Typically a population size of five or ten individuals was used, with population sizes up to 40 in some runs. Typically 30 offsprings were generated every generation. The most successful mutation and crossover rates were 75%. Elitism was not applied.

B.2 Paper2: Optimizing Zeeman deceleration of atomic hydrogen by evolutionary algorithms

This is the bachelors thesis by Salathe [86]. The experiment was to expand NH3 seeded in Ar, ratio 10:1, then by using a 193 nm photolysis laser to produce H. The H is decelerated using 12 stages of Zeeman decelerator, and loaded into a quadrupole magnetic trap.

The technique used was called Covariance Matrix Adaptation Evolution Strategy (CMA-ES), which is a variation of Evolution Strategy under the broad category of evolutionary algorithms. Intuitively, the covariance matrix generalizes the notion of variance to multiple dimensions. As an example, the variation in a collection of random points in two-dimensional space cannot be characterized fully by a single number, nor would the variances in the x and y directions contain all of the necessary information; a 2×2 matrix would be necessary to fully characterize the two-dimensional variation.

There are two objective functions that were optimized simultaneously, first object was to maximize the number of trapped particles inside the magnetic quadrupole trap, and second objective was to minimize the mean total energy of the trapped particle. An optimization with these two objectives will also optimize the local phase-space density of the trap. Since the total energy determines how far a particle can move up the potential hills which compose the trap and is at the same time an upper bound on the kinetic energy of the particles.

The parameters to optimize were the timing sequence of each stage individually. Hence the parameter space consists of 12 stages, plus the opening and closing of the trap, so in total, a 14 dimensional optimization.

The optimization result is enhancement of the number of trapped atoms by more than a factor of 6, from 0.2% of the total number of sampled particles to about 1.6%.

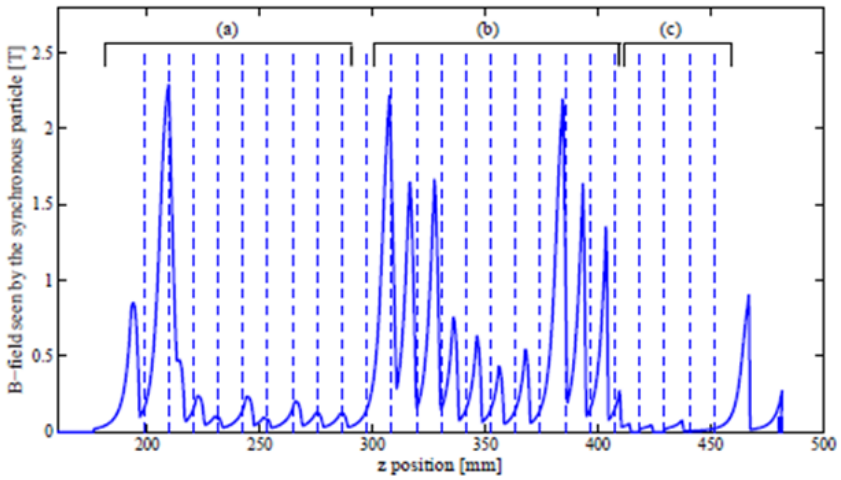

Figure 6.4 – Sample output coil firing sequence from salathes thesis.

B.3 Feasibility study

In Salathes thesis, for each function evaluation it takes about 90 seconds, with number of particles = 500. Each population consists of 16 individuals, and number of required function evaluations is typically on the order of 10^4 to 10^5. Parallelization is necessary.

Assuming in our case, we can also reduce our dimensionality to around 10, and assuming we would also need 10^5 function evaluations. At current level of parallelization of our code, in case of 500 particle, dt=1us, each function evaluation is roughly ~1min, and 10^5 function evaluations would take ~70 days. By our estimation, by rewriting part of the code in C, instead of matlab, and by parallelizing our code better, we can reduce the calculation time by a factor of 10. In this case, one full optimization is possible to be done in 7 days, which is more realistic.

However, there are always the disadvantage of evolutionary algorithm, which is that is give little physical insight on WHY the optimized timing sequence is better. And hence intelligent and systematic way to improve on the optimized result, from evolutionary algorithm, is nearly impossible.

Appendix C What is quantum computer?

In the field and cold and ultracold molecules, quantum information and quantum computation has always been mentioned as one of the possible motivations of the field. For example, ultracold polar molecules have been mentioned to be a potentially superior candidate for the realization of quantum bits in a scalable quantum computer [3] And for example, the study of well-localized Ultra-Cold Molecular Ions have been mentioned to be very attractive physical systems for studying multi-particle entanglement as well as for quantum computer research. [2] Ultracold molecules might be a new platform for quantum computing [5]

However, in these reviews and publications, where experts talk to other experts, it is taken for granted that the reader knows what a quantum computer is, and hence there no further discussions about the concept of quantum computer. On the other hand, in popular science, where the concept of quantum computer is not completely alien, but the description of quantum computer is just insufficient. They would throw big words such as entanglement, qubit, and superposition without understanding implication and meanings of those words.

For the intermediately educated ones, such as myself, the most fundamental, yet the simplest question is, What is a Quantum Computer? And how is quantum computer related to the field and ultradcold molecules? In this section, my goal is to clarify the concept of What is Quantum Computer, and its relation to the field of ultracold molecules, and to point out to useful references about this topic. I'll do this as best as I can, with the hope of enlightening other intermediately educated people, so that they don't need to go through all the confusion I went through to obtain such knowledge.

The steps I'll take, in order to explain quantum computer is following. First, I need to remind ourselves, what is a (classical) computer? Then the notion of universality is introduced, followed by a important discussion on distinguishing algorithms from physical implementation of these algorithms. Then I talk about quantum computer side by side against the classical computer, using the latter as a reference in order to stay sane in the quantum world. After that,

I'll show the simplest quantum algorithm step by step, and lastly, physical implementation of such algorithm.

C.1 The classical computer

To start, we need to first remind ourselves what is a (classical) computer. We can think a computer is a black box, translating set of inputs into set of outputs in a systematic deterministic way. More precisely, computer is a physical implementation of an algorithm, which does the things above. Let me clarify.

C.2 Algorithm and notion of universal gates

An algorithm, not a computer, translates a set of input into a set of output in a systematic way. Another way to think about this is, Algorithm is just a set a instructions, with a goal to solve some problems which interests us. In the case of computer algorithm, Boolean logic is used, that is, all information, all the input and all the outputs are represented in 0's and 1's, instead of 0's 1's and 2's for example. And in Boolean logic, logic gate is just a function, which takes one or more boolean inputs, and produces a single boolean output. Example of logic gate is AND-gate, OR-gate, XOR-gate etc.

One might ask, why we are using this Boolean logic, ie why are we using 0's and 1's? The answer to this is probably due to historical reasons, and probably this is the form of the logic that we human beings find the easiest to understand. In fact, people have tried to make non-boolean logic to work, and one such non-boolean system is called Three-valued logic. [89] In Three-valued logic the basis is +'s -'s and 0's, instead of 1's and 0's, and the logic is quite different from what we are used to. Here I merely want to make the reader aware such logic exists.

A simple example of an algorithm is a sorting algorithm, where the problem at our hand is, we are given list of number, A, and we need to sort the list in descending/ascending order. The

solution to our problem is simple, we look at two consequtive element at a time, swap them if they are in the wrong order, and we do this until A is sorted.

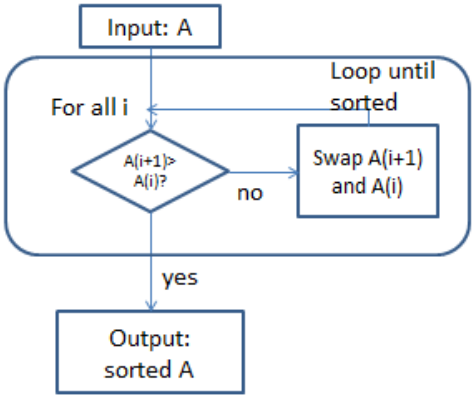

Figure 6.5 - A simple sortying algorithm

For our discussion, the correct question is ask is, how do we represent the operations, A(i+1)>A(i)? and Swap A(i+1) and A(i), using the Boolean logic gates? It turns out that there is a notion, called universal logic gates, which can reproduce the functions of all the other logic gates . In Boolean logic, example of such set of universal gates is {AND, NOT}, and another set of universal gates are {NAND}.

For our example. The logic gate A(i+1)>A(i)? can be reproduced by only using {NAND} gate. However, I'll omit the details about how to construct a digital comparator from NAND gates here, as it goes too deep into digital circuitry. But we will trust that the logic gate A(i+1)>A(i)? can be reproduced by only using {NAND} gate is a fact.

To get a feeling about universal logic gates, I show how would we get a OR gate, from NAND gate. We would want a truth table, which corresponds to the gate OR, and it works out that the truth table following combination of NAND gate, NAND(NAND(A,A),NAND(B,B)), is exactly equal to the truth table of OR gate. And hence our task is complete.

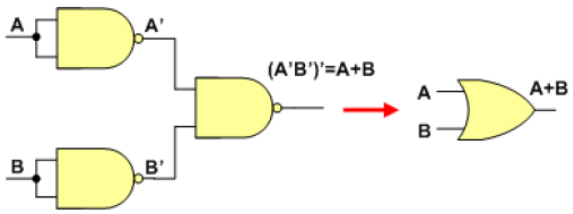

Figure 6.6 - universality of NAND

Truth Table

Input A	Input B	Output Q
0	0	0
0	1	1
1	0	1
1	1	1

Figure 6.7 - truth table of NAND

C.3 Physical implementation of the algorithm

So far, we have only discussed about the logical part of our classical computer. Next, we need to discuss how to construct such logics in our physical world. Remember, the Boolean logic, algorithms, and gates discussed above are independent of our physical implementation of them. We will choose whatever is convenient for us, as long as our physical system behaves identically to our logical system. As we all know, computers in our era are made from transistors, and integrated circuit boards. The transistor-transistor implementation of a set of universal gates can be seen here. Simple circuit analysis shows that in AND gate, both A and B need to be at +volt for output to be +volt, otherwise output is 0volt. And for the NOT gate, the input is the base of a transistor connected to the ground, hence acting like a NOT gate.

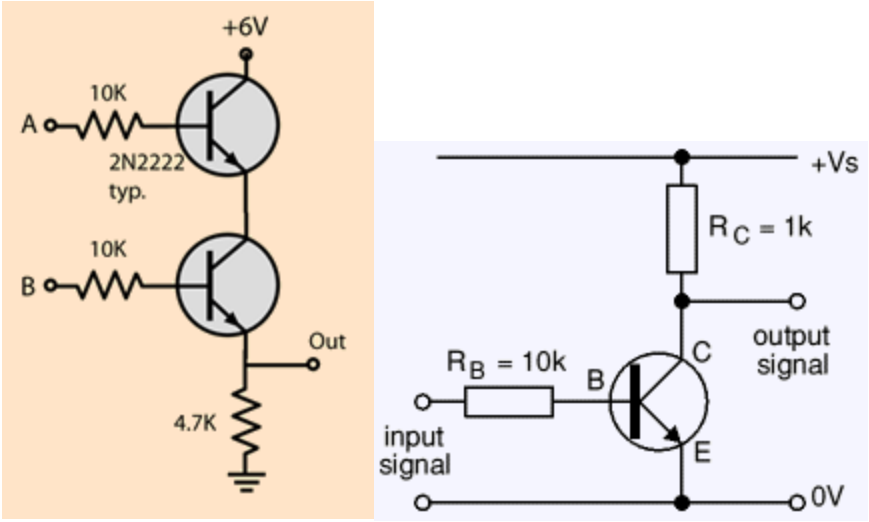

Figure 6.8 - Physical implementation of AND gate and OR gate

With modern technology, printing micro circuits onto silicon wafers, we can fit 10^8 transistor onto a cm^2 area. And since we can have the universal logic gate using transistor-transistor logic, then any other logic gate can be built from transistors.

We need to note, the reason of using transistors is convenience, it is light, cheap, robust etc. But in fact, we can choose any other system which behaves like our logical system, and we don't have to use transistors at all. Actually, the earliest ideas of computer comes from Charles Babbage (1791-1871) and the first mechanical computer was created by German engineer Konrad Zuse in 1941. This worlds first computer, called Z1, has 30,000 mechanical components, 30tons in weight, and 500miles of wiring. [90] The input and output were punch cards. It ran with a 1Hz system clock, and it had 62bits are memory. To put these numbers into prespective, in year 2013, 70years after creation of Z1, the standard system clock is 1GHz. What would take 1hour for our modern CPU to do, Z1 would need 1e9hours to do the same thing, that is 10,000 years. However, even more remarkably, Z1 ran on the exact same Boolean logic that modern computers runs on, nothing has changed on the logical part, only the physical implementation got miles better.

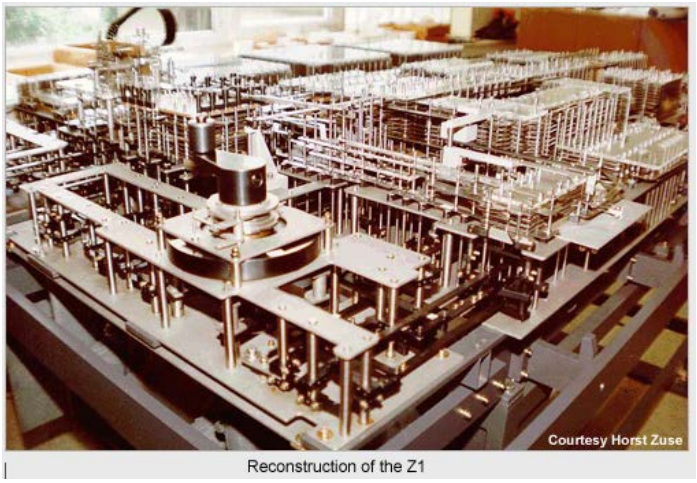

Reconstruction of the Z1

Figure 6.9 - first mechanical computer, named Z1

The idea of a computational device based on quantum mechanics was first explored in the 1970's and early 1980's by physicists and computer scientists such as Charles H. Bennett of the IBM Thomas J. Watson Research Center, Paul A. Benioff of Argonne National Laboratory in Illinois, David Deutsch of the University of Oxford, and the late Richard P. Feynman of the California Institute of Technology (Caltech). [90] In 1994, Peter Shordemonstrated how prime factorization and the calculation of the discrete logarithm could be efficiently performed on a quantum computer. [91] Now known as the Shors algorithm.

The idea of quantum computer, is that, instead of using Boolean logic, we would a complete new kind of logic, arising from the quantum mechanical nature of things. I would call this quantum logic, but the term quantum logic is already reserved fro something else, so I'll refer to this as quantum computer logic. Next, we take a brief look at what is this new kind of logic and its algorithm, without thinking too much where it came from, or why it is useful, or the physical implementation of this logic. After that, we will take some examples, about why it is the way it is, some physical implementation and what is the hype about quantum computers.

C.4 The quantum computer

To remind ourselves, in Boolean logic, our basis was 1's and 0's. In three value logic, our basis was +'s –'s and 0's. So on the same train of thought, in our quantum computer logic, our basis

happen to be |1>'s and |0>'s. The ket notation around 1's and 0's merely indicates this basis have some special properties, that basis in Boolean logic wouldn't have. For example the property of superposition, |1>+|0>, is a valid basis in quantum computer logic, whereas 1+0 in Boolean logic is not defined. Note that the plus sign in 1+0 is not an AND gate. Also, the measurement is different, the outcome of a measurement in a superposition state will be governed by quantum mechanics. Lastly, we call |1>'s and |0>'s qubits, instead of bits.

The logic gate, is just a mapping from initial state of the basis, to the final state. The logic gates in Boolean logic are for example AND, OR, XOR gates. These logic gates will map bits onto bits in Boolean logic. So, similarly, in quantum computer logic, we also have operations which maps qubits onto qubits, we call these quantum logic gates, or quantum gates. Example of quantum logic gates are Hadamard gate, Cnot gate, Toffoli gate etc.

Similarly to Boolean logic, where there exist a set of universal logic gates, namely {NAND} gate in Boolean logic. In quantum computer logic, there also exist a set of universal quantum gates. For example {hadamard gate, Toffoli gate} is such a set of universal quantum gate. And the challenge is again, to find a good physical implementation of such set of quantum gates. Once we can realize a set of universal quantum gate, then we can build any quantum algorithm we can imagine.

C.5 New gates in the quantum world

Let's take a look of some examples, for example the NOT quantum gate

$$NOT(|1\rangle) \rightarrow |-1\rangle$$

This behaves somewhat similar to Boolean logic. But, lets look at another gate, called hadamard gate, which has no analogy in Boolean logic.

$$H(|1\rangle) \rightarrow \frac{1}{\sqrt{2}}\left(|1\rangle + |-1\rangle\right)$$

$$H(|-1\rangle) \rightarrow \frac{1}{\sqrt{2}}\left(|1\rangle - |-1\rangle\right)$$

Equation 6.2

We see that this gate maps qubit, onto a superpositionof states. Meaning that, if the measurement is taken after this gate, the value of the qubit will have exactly 50% chance to be |1>, and 50% chance to be |-1>.

C.6 New algorithms in the quantum world

Next, I want to show a quantum algorithm, called Deutch jooza algorithm[92], which is one of the simplest quantum algorithms that demonstrate why quantum algorithm is faster than classical algorithm.

Suppose we have a function, f, which acts on pair of qubits in following way

$$f(|x, y\rangle) \rightarrow |x, yf(x)\rangle$$

The question we need to answer is,

$$f(|1\rangle) = f(|-1\rangle) \ \text{OR} \ f(|1\rangle) = -f(|-1\rangle) \quad ?$$

The strategy is following, we prepare our initial state in a certain state, which is a superposition state. Then we act f on this superposition state, and then we try to extract information from our final state after f has acted on our system. And the catch is, in this quantum algorithm, our function f, has only been called once. Whereas classically, f needed to be called twice, in order to answer the question we asked above.

We use the basis of |x,y>, which is a pair of qubits. And we start from two well defined state of |x,y>

$$|\psi(0)\rangle = |1,1\rangle$$

Equation 6.3

We then take NOT gate on the 2nd quibit, yielding

$$|\psi(1)\rangle = |1,-1\rangle$$

Equation 6.4

Next we use hadamard gate on both qubits

$$|\psi(2)\rangle = \frac{1}{2}(|1\rangle + |-1\rangle)(|1\rangle - |-1\rangle) = \frac{1}{2}(|1,1\rangle + |-1,1\rangle - |1,-1\rangle - |-1,-1\rangle)$$

Equation 6.5

And here, we have finished our preparation, next we act f on to our system.

$$|\psi(3)\rangle = \frac{1}{2}(|1, f(1)\rangle + |-1, f(-1)\rangle - |1, -f(1)\rangle - |-1, -f(-1)\rangle)$$

Equation 6.6

We separate into two cases, case1, if f(1)=f(-1):

$$\text{If} \quad f(1) = f(-1) = f, \text{ then}$$

$$\Rightarrow |\psi(3)\rangle = \frac{1}{2}(|1, f\rangle + |-1, f\rangle - |1, -f\rangle - |-1, -f\rangle) \backslash\backslash = \frac{1}{2}(|1\rangle + |-1\rangle)(|f\rangle - |-f\rangle)$$

Equation 6.7

Case2, if f(1)=-f(-1):

$$\text{If} \quad f(1) = -f(-1) = f, \text{ then}$$

$$\Rightarrow |\psi(3)\rangle = \frac{1}{2}(|1, f\rangle + |-1, -f\rangle - |1, -f\rangle - |-1, f\rangle) \backslash\backslash = \frac{1}{2}(|1\rangle - |-1\rangle)(|f\rangle - |-f\rangle)$$

Equation 6.8

Then to extract the information we want, we measure the value of the first qubit, and we do this by applying a hadamard gate on it.

$$H\frac{1}{\sqrt{2}}(|1\rangle + |-1\rangle) = |1\rangle$$

$$H\frac{1}{\sqrt{2}}(|1\rangle - |-1\rangle) = |-1\rangle$$

Equation 6.9

Hence, in summary, by going through this algorithm, and by taking the measurement of our first qubit |x> at final stage, we are able to answer our question of f(1) = +f(-1) or f(1) = -f(-1). And we were able to answer this by only calling f once in this algorithm, instead of calling f twice, which is necessary in classical algorithm(Justification is found here.[92]) Usually, the function call f, is time consuming, and the less times we call f, the faster the algorithm is.

$$|x_f\rangle = 1 \Rightarrow f(|1\rangle) = f(|-1\rangle)$$

$$|x_f\rangle = -1 \Rightarrow f(|1\rangle) = -f(|-1\rangle)$$

Equation 6.10

C.7 Physical implementation of the quantum algorithms

So, far, we only hypothesized, whatif we had qubits and quantum gate with such and such property, and we noted that with those new tools, we were able to device new algorithms which are faster than classical algorithms. Now, the question is, where do we get systems which has these quantum properties we want? And this is indeed the question. Many 2-level quantum systems, such as quantum dots, NV-centers, josephson junctions etc, has been proposed to used as the physical implementation of this quantum computer logic. But one of the main limitation of quantum computer is the short coherence time of the qubits. And the way to tackle the decoherence problem, is to make cold atoms and molecules.

For example, in [93], DeMille proposed to use trapped ultracold polar molecules to realize quantum computation. The qubits would consist of the electric dipole moments of diatomic molecules, oriented along or against an external electric field. And quantum gate operations are Transitions between qubit states can be driven by electric resonances. And The usage of ultracold molecules makes it possible to use a weak trapping potential, which would allow long decoherence times for the system, up to 5 seconds. [93]

Appendix D Notes on numerical simulation

In order to explain and analyse the data from experiment, we need a model. An analytical model is always preferred, but in the case such model doesn't exist, or is too imprecise, then we have to result in using a numerical simulation. The purpose of this section is to guide potential new users of the simulation code, which was used to simulate Zeeman deceleration experiment. This should be an additional document, and not a standalone document, that should be used together with the source code and comments inside the source code.
This section is in three sub sections. First we explore the structure and format of the program, alongside with necessary physics. Then we go into each sub function individually, trying to point out pit falls that I have learned while developing the code. This is to aid readers to understand why some of the code were written as they were, and also aid other people who might be developing similar kind of code, to not to fall for the same pit falls as I did. And finally, we will take a look about parallelizing the simulation code to run on a cluster.

We want to note here, that source code of the simulation is not included in this thesis, the source code will be available however upon request, for contact information, see ref [94].

D.1 Overview

Generally speaking, the essence to a molecular dynamics simulation is in three steps. First, in the preparation step, we would set up our molecular/potential model, and we also set the constrains: for example keeping the system under constant temperature; or constraining monolayer of insoluble molecules on the surface of the container etc. Next, in the evolution step, the system is evolved using Newtonian equations. Here many different numerical techniques can be used. In an ideal world, all techniques would evolve the system in an identical way. But in reality, a balance of speed and accuracy must be found, as both cannot be achieve simultaneously. Finally, in the measurement step, we use statistical methods to convert data in molecular dynamics simulation into data we observe in the laboratory.

The simulation code for Zeeman deceleration was written by one person, Sida Zhou[94]. The development of simulation code started early 2010, first working version of the code took three months to complete, and at that point the code was in 2D cylindrical coordinates. Since then the code has been upgraded to 3D Cartesian coordinate, in anticipation of bended magnetic guide simulations. Along the years 2010-2013, the code has been bug fixed, optimized, error checked and parallelized. Currently the code gives simulation result that matches experiments satisfactorily.

The main purpose of the simulation is to 1) simulate the experimental result; 2) analyze the behavior of non synchronous molecules; 3) determine how sensitive the system is, to experimental errors and fluctuations. All goals stated above have been achieved to a satisfactory level, but there is definitely room for improvement.

D.2 Brief history of molecular dynamics simulation

Early models for simulating gases and liquids are developed in late 1930s and 1940s by Morreli, Hildebrand, Hatree and Buneman.

The most success model, now known as the Molecular dynamics, was first introduced by Alder and Wainwright in the late 1950's. They studied simulation of the interactions of hard spheres extensively. Motivation was to solve the many-body problem numerically, since the exact analytical solution does not exist.

The aim of this research, and further researches followed, was to obtain measurable quantities such as pressure, collision rate, potential energy surface, equilibrium, phase-transitions, distribution of kinetic energy, temperature gradient, velocity gradient, distribution of cluster sizes, boundary conditions, system sizes, lattice types. The next major advance was in 1964, when Rahman carried out the first simulation using the LJ-potential for liquid argon. In the simulation, Rahman obtained quantities such as diffusion constant and neutron scattering data, which was in agreement with experiments. The first molecular dynamics simulation of a

realistic system was done in 1974 by Rahman and Stillinger in their simulation of liquid water. They studied the effect of different anisotropic potentials, in terms of diffusion, scattering, thermodynamical and dielectric properties.

D.3 Choice of integrator

It is obvious, when we discretize the continuum, the solution obtained will be an approximation at its best. The results of the simulation will be directly linked to how well these calculated approximations converge to the analytical value. Hence different integration techniques are used in different situations.

There are several choice of integrator for the simulation, for example Euler's method, Verlet leap-frog method, velocity Verlet method, and Runge-Kutta method. In principle, there are four criteria, to determine which integrator is most suited for our need, which are consistency, accuracy, stability and efficiency. Each of the integrators has pros and cons in terms of these four criteria. For example, the 4th order Runge-Kutta method, its advantage over Velocity Verlet is that, the accuracy is fourth order, and dynamical timestep can be more easily implemented. And the disadvantage of Runge-Kutta is that, the algorithm is not time reversible.

However in practice, 4th order Runge-Kutta was selected, because it was an industrial standard in molecular dynamics simulation. 4th order Runge-Kutta uses a trial step at the midpoint of an interval to cancel out lower-order error terms. Generally, Velocity Verlet is preferred when energy conservation is desirable, and RK-methods are used when external forces are involved.

The stability of 4th order Runge-Kutta integrator was compared against 8th order Runge-Kutta, by comparing the trajectory of a single molecule inside the Zeeman decelerator. The result of 4th order and 8th order Runge-Kutta converged, given the timestep and gridsize, and hence 4th order was chosen for efficiency.

D.4 gridsize and timestep

Gridsize in z direction is $2.4e-5 meters$, and gridsize in x and y direction is $8.0e-5 meters$. The gridsize is large enough to avoid handling of too large data sets; and the gridsize is small enough, that the B-field within one 3D grid is smooth enough for us to use trilinear interpolation within the grid. Trilinear interpolation is the next fastest available method, in the case of fitting an analytical function to the field is impossible.

The natural timestep of the simulation is $dt = 1ns$, however in practice the simulation is routinely run at $dt = 1000ns$ and $dt = 100ns$. The timestep is chosen to be large enough to minimize the computation time; and the timestep is chosen to be small enough to ensure the convergence of the result. We have tested and found that $dt = 100ns$ converges to the result of $dt = 1ns$ under typical parameter values. We also want to note, the convergence of the result here means the convergence of result of simulated TOF spectra (less strict), and not the convergence of traces of individual particle (more strict). For $dt = 1000ns$ and $dt = 100ns$, running time of one simulation takes around $30\,\mathrm{min}$ and $2\mathrm{h}$ respectively. And for $dt = 1ns$, running time is $> 5\mathrm{h}$.

D.5 Program execution order, flow chart

The whole simulation code and its output consist of several parts, which I have labeled as: job submission, simulation, output, postprocessing and postprocessed output, see Figure 6.10. There are total of 15 matlab scripts as the source code, total of 2400 lines of code. Each part will be elaborated more later in the text.

Each run of the code consist of trajectory calculation of all quantum levels of interest. Typically, each quantum contains 0.1million molecules, with 100ns time step. For total simulation time 5ms, it means $5ms/100ns = 50000steps$ per quantum level. Running time for these parameters is $1\mathrm{h}20\,\mathrm{min}$ per quantum level.

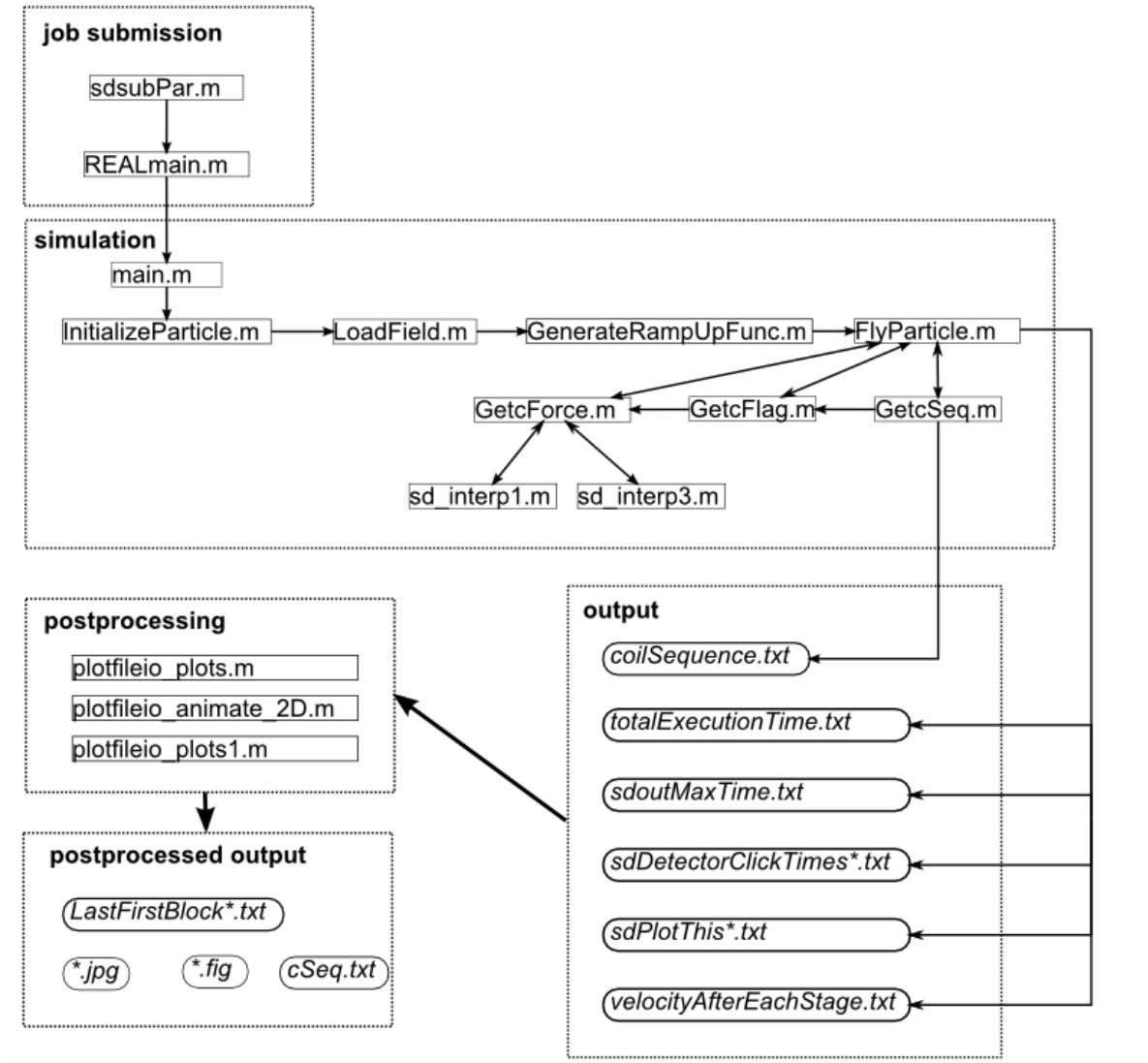

Figure 6.10 – flowchart of the simulation code. The arrows indicate the order of execution. Square frame indicates the file is source code, and round frame indicates that the file is output

D.6 Choice of Matlab over Fortran

Here, as a side note, we want to make a quick note why we have chosen matlab as the language to use. The choice was made at very beginning of the code development. The main alternative was to use fortran. There were several pros and cons for each of the language. The cons of using matlab are that, 1) matlab is proprietary software, which is not free to use; 2) matlab is not a compiled language, hence calculation will be slower than fortran. The pros of using matlab are that, 1) integrated GUI; 2) plotting functionalities; 3) matrix handling; 4)

debugging functionalities. For us, since we held a matlab license, so the cost was not an issue. And for the code running speed, we did several speed tests, and noted that for simple for loops matlab is only 10% - 20% slower compared with fortran, when done correctly. Therefore, in the end the decision was to use matlab instead of fortran.

Doing things correctly, as mentioned above, means vectorizing parameters (vectorizing is a method specific for matlab language), if not done correctly, the overhead can large, and code can slow up to 200%. Matlab, as a software, developed over the years, the requirement of vectorization disappeared, and nowadays matlab JIT engine accelerates the code to a decent level with ease.

D.7 Physical units used in the programs

Working with dimensionless units, means that we can work numerical values that are not too big or too small for the computer to handle. Working with dimensionless unit also means that a single model can describe a whole class of problems.

For example, in our simulation, we use atomic mass units instead of kilograms; and we use a time scale of nanoseconds, instead seconds. This means that the simulation would map onto the laboratory experiment in the following way:

Mass scale: $1\ unit \rightarrow 1.6605e-27kg$

Length scale: $1\ unit \rightarrow 1\ meter$

Time scale: $1\ unit \rightarrow 1e-9seconds$

One of the calculated results was longitudinal force exerted on the molecule at a given time, F_z. For example, if simulation outputs $F_z = 0.8units$, the result is not useful until we convert it back to some meaningful units, for example SI units. And we can do this conversion by using dimension analysis, we can transform this into Newtons: $1N = 1\frac{kg\ m}{s^2}$

$F_z = 0.8 units$ actually reads: $F_z = 0.8 \frac{(mass\ unit)(length\ unit)}{(time\ unit)^2}$

Using $\frac{1\ mass\ unit}{1.6605e-27 kg} = 1$ etc.

Force in Newtons is then

$$F_z = 0.8 \frac{(mass\ unit)(length\ unit)}{(time\ unit)^2} \times \frac{1.6605e-27 kg}{1\ mass\ unit} \times \frac{1\ meter}{1\ length\ unit} \times \left(\frac{1\ time\ unit}{1e-9 seconds} \right)^2$$

$$\Rightarrow F_z = 1.3284e-9 Newtons$$

So, in this example, 0.8 units of energy in simulation correspond to 1.3284e-9 Newtons in the laboratory. Similar logic can be applied to other simulations, in order to scale physical magnitudes into more manageable magnitudes in the simulations.

D.8 A subtle problem at the boundary

When a molecule is collided with the inner wall of the decelerator ($radius = 2mm$), we assume it will be absorbed by the wall, which is at liquid nitrogen temperature. The way to implement this in the simulation is to say: if (radial_position > 2mm) then (wall_collision_happened()). However when implemented naively, this logic will not function properly in our simulation code.

In Figure 6.11, consider a HFS molecule very close to the inner wall of the coil, point A, travelling towards the wall, point B. And will reach point B after the next timestep. Physically, this HFS molecule should hit the wall and disappear. However problem arises: in Figure 6.11, the B-field strength of the undefined region of space is naively set to zero, and the Runge-Kutta (predictor corrector integrator) tries to predict where the molecule should go from point A, it

sees zero B-field at half timestep, and predicts that the HFS molecules should be strongly repelled by the wall. And hence, the molecule in this scenario will wrongly travel to point C.

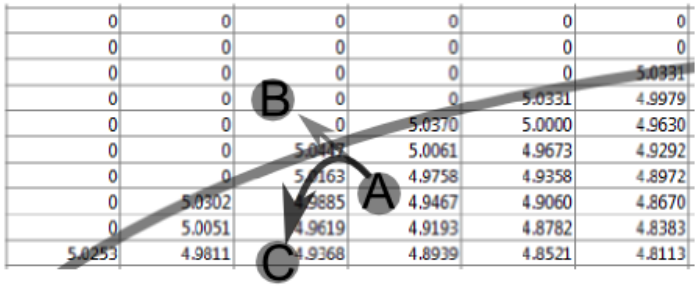

Figure 6.11 – we see tabulated B-filed data , where undefined region is set to zero; and overlay is the boundary is the inner wall of the coil. Molecule start at point A, physically, the molecule should be go point B in the next one timestep, but because of naive implementation, molecule wrongly goes to point C instead.

The problem is an artefact arose from simultaneous usage of Runge-Kutta, inaccurate field definition (zero field), and naive logic check of wall collision. This artefact will heavily focus the HFS molecules, which is unphysical. There are many fix to this problem. One of the elegant ways to fix this is to set undefined area to NaN, see Figure 6.12, and add logic check: if (Force == NaN) then (Force = 0). And the molecule from point A will travel to point B as intended, and consequently, will be eliminated once reached point B, due to collision with wall.

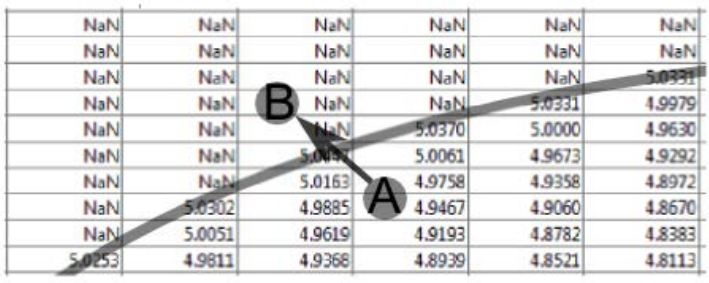

Figure 6.12 – we see tabulated B-filed data, where undefined region is set to NaN; and overlay is the boundary is the inner wall of the coil. Molecule starting from point A will go to point B as intended. And at point B, the molecule will be eliminated due to collision with wall.

D.9 Input files

In this sub section, we want to point out several parameters that are typically varied in the simulation, their typical values and in which file these parameters are located.

sdSubPar.m
Nprocs='10'; Number of processors requested on the cluster
Wtime='5:00:00'; Walltime per processor
Memory='10gb'; Total memory request for all processor

REALmain.m
Npt=100000; Total number of molecules per quantum state
sdParam=1:9; Which quantum state to include in the calculation

InitializedParticle.m
Vxy(1,:), Vxy(2,:), Vxy(3,:) Longitudinal and transverse velocity distribution, in meters

main.m
mass = 32; Mass of the molecule, in atomic units
dt = 1000; Timestep, in ns
nozzleDistance = 0.155229; Distance of nozzle and 0 degree of first coil, in meters
DetectorDistance = 0.012 - 0.001; Distance of 180 degree of last coil and detection, in meters
DetectorRadius = 5e-3 ; Estimated beam waist of detection laser, in meters
raleyLength = 5e-3; Estimated raley length of detection laser, in meters
sdDelay = 0; Timing delay of trigger of coils relative to trigger of nozzle
centralVel = 380; The central velocity of free flight packet
targetVel = 320; The velocity of the synchronous (target) molecule, in m/s
nozzleOpeningTime = 65e-6; Nozzle opening time, in seconds
sdPhase = 43; Switching phase
numberofcoils = 80; Number of Zeeman deceleration stages
NstepRampUp = ceil(70e-6/ 1e-9 / dt); Number of timesteps needed for ramping up the field
NstepRampDown = ceil(1e-9 / 1e-9 /dt); Number of timesteps needed for ramping down the field

LoadField.m
load '~/4mm_600A_4.27T_3D_NaN.mat' The B-field data in 3D grid
FlyParticle.m
load '~/ZeemanShiftO2.mat' Zeeman shift of the molecule
GetcSeq.m

Custom code need to inserted in this file for different mode of operations, for example bunching etc. or for simulation of broken coils etc.

D.10 Output files

There are several files produced per one run of the simulation, here is a brief summary.

Following three output files are system wide:

totalExecutionTime.txttotal running time of the simulation in seconds
coilSequence.txt coil switching timing in simulation units
cSeq.txt coil switching timing in SI units

Following two output files are for monitoring different parameters of the synchronous molecule:
sdoutMaxTime.txt total time simulated; arrival time of sync molecule
velocityAfterEachStage.txt velocity of sync molecule after each stage

Following five output file series are for monitoring different parameters of the non-synchronous molecules, states are labled 1,2,3… which is denoted with * in the fileanames below. State1 is the lowest in energy etc.
sdPlotThis*.txt trajectory of all molecules
sdDetectorClickTimes*.txt time of arrival in the detection region
LastFirstBlock*.txt final phase space; and initial phase space
*.jpg postprocessed figures with lossy data (for browsing)
*.fig postprocessed figures with lossless data